ISSN 0915-6348

NATIONAL INSTITUTE FOR FUSION SCIENCE

Plasma Spectroscopy and Atomic Processes

— Proceedings of the Workshop at Data & Planning Center in NIFS —

(Received – Aug. 28, 1990)

NIFS-PROC-4 Sep. 1990

RESEARCH REPORT
NIFS-PROC Series

NAGOYA, JAPAN

Plasma Spectroscopy

and

Atomic Processes

- Proceedings of the Workshop
at
Data & Planning Center in NIFS -

Keywords

plsama spectroscopy, line intensities, plasma diagnostics, atomic processes, energy levels, cross sections, rate coefficients

Preface

This is the proceedings of the workshop on "Plasma Spectroscopy and Atomic Processes" held on May 14-15, 1990 at the Data and Planning Center in National Institute for Fusion Science (NIFS), under the joint research program. For the workshop we had the honor of having two Russian atomic physicists, Professors U. Safronova from Institute of Spectroscopy in Troitzk and L. Vainshtein from Lebedev Physical Institute in Moscow. Professor Safronova stayed in NIFS for three months under the JSPS fellowship for research in Japan. Professor Vainshtein was invited by our institute to stay for two weeks. They worked mainly on atomic data of highly ionized ions during their stay in our institute.

Our intention of this workshop was to have animated discussion between atomic physicists and plasma physicists. There are many interesting atomic processes in plasmas, and they should be investigated in order to solve the problems related to plasma physics. We hope this workshop will become a good opportunity to organize more new collaboration programs together with scientists both in atomic and fusion plasma physics.

We had wanted to have active exchange between Russian and Japanese scientists. Indeed this workshop was of great help for two Russian scientists to get to know many Japanese scientists and to understand their activities.

Since English is not a native language for both Japanese and Russian, we were concerned about language problems. But we could manage to communicate with one another in English.

We would like to express our sincere thanks to the director Professor A. Iiyoshi for supporting this workshop. We would also like to thank all the participants of the workshop.

Takako KATO
(NIFS)

CONTENTS

16. Plasma Diagnostics of Solar Flares with SOLAR-A Bragg Crystal Spectrometer
    T. Watanabe
17. He-like Spectra from Laboratory Plasmas and Solar Flares
    T. Kato

Professors L. Vainshtein (left) and U. Safronova (right)

PROGRAM

PLASMA SPECTROSCOPY AND ATOMIC PROCESSES

Date: May 15 (Tuesday) 13:30 - May 16 (Wednesday) 17:00
Place: National Institute for Fusion Science
Conference Room on the 8th floor

May 15 (Tuesday)

13:30-15:30 (Chairperson: F. Sasaki)
Opening
A. Iiyoshi (NIFS)

1. Perturbation Theory for Calculation of Atomic Data (50min.)
   U. Safronova (Institute of Spectroscopy, USSR)
2. Relativistic Configuration Interaction Method for Atoms (20)
   T. Kagawa (Nara Women's Univ.)
3. Polarization Plasma Spectroscopy (20)
   T. Fujimoto (Kyoto Univ.)

Coffee break (15:30-16:00)

16:00-18:00 (Chairperson: J. Fujita)

4. Spectroscopy in Heliotron E (20)
   K. Kondo (Kyoto Univ.)
5. Measurement of Electric Field from Plasma Rotation using C VI Lines (20)
   K. Ida (NIFS)
6. X-ray Spectra from High Temperature Plasmas (20)
   S. Morita (NIFS)
7. X-ray Amplification at 54.2A on Balmer α Transition of H-like Sodium (20)
   H. Shiraga, Y. Kato (Osaka Univ.)

18:30-
Party (Conference Room on the 8th floor)

May 16 (Wednesday)

9:30-10:30 (Chairperson: K. Sakimoto)

1. Numerical Calculations of Atoms in Plasmas (20)
   K. Fujima (Yamanashi Univ.)
2. Charge Transfer Calculations between Highly Charged Ions (20)
   F. Koike (Kitasato Univ.)

Coffee break (10:30-10:45)

10:45-12:15 (Chairperson: H. Tawara)

3. Collisional Processes Involving Doubly Excited States of He, H^- (20)
   M. Matsuzawa (Univ. Ele. Com.)
4. Electron Spectra from Doubly Excited Highly Charged Ions (20)
   Y. Kanai (IPCR)
5. Resonance States of Muonic Molecules and Muon-Catalyzed Fusion (20)
   I. Shimamura (IPCR)

Lunch (12:15-13:30)

13:30-15:00 (Chairperson: T. Kawamura)

6. Code ATOM for Calculation of Atomic Characteristics (50)
   L. Vainshtein (Lebedev Physical Institute, USSR)
7. Differential Cross Sections for Electron Impact Excitation of Atomic Ions (20)
   Y. Itikawa (ISAS)

Coffee break (15:00-15:30)

15:30-17:00 (Chairperson: R. Akita)

8. Plasma Diagnostics using Line Intensiy Ratios (20)
   K. Masai (NIFS)
9. Plasma Diagnostics of Solar Flares with SOLAR-A Bragg Crystal Spectrometer (20)
   T. Watanabe (National Astronomical Observatory)
10. He-like Spectra from Laboratory Plasmas and Solar Flares (20)
    T. Kato (NIFS)
11. Discussion and Concluding Remarks

LIST OF PARTICIPANTS

Ulyana I. Safronova	Institute of Spectroscopy, Troizk, USSR
Leonid Vainshtein	Lebedev Physical Institute, Moscow, USSR
Ryou Akita	Osaka Gakuin University
Kazumi Fujima	Faculty of Engineering, Yamanashi University
Takashi Fujimoto	Dep. of Engineering Science, Kyoto University
Junji Fujita	National Institute for Fusion Science
Yukikazu Itikawa	The Institute of Space and Astronautical Science
Katsumi Ida	National Institute for Fusion Science
Kiyoshi Kadota	Plasma Science Center, Nagoya University
Takashi Kagawa	Dep. of Physics, Nara Women's University
Yasuyuki Kanai	The Institute of Physical and Chemical Research
Takako Kato	National Institute for Fusion Science
Takaichi Kawamura	National Institute for Fusion Science
Naoshi Kobayashi	Faculty of Engineering, Osaka University
Fumihiro Koike	School of Medicine, Kitasato University
Katsumi Kondo	Plasma Physics Laboratory, Kyoto University
Kuniaki Masai	National Institute for Fusion Science
Mitio Matsuzawa	Dep. of Applied Physics and Chemistry, the University of Electro-Communications
Shigeru Morita	National Institute for Fusion Science
Kazuhiro Sakimoto	The Institute of Space and Astronautical Science
Fukashi Sasaki	Faculty of Science, Hokkaido University
Isamu Shimamura	The Institute of Physical and Chemical Research
Hiroyuki Shiraga	Institute of Laser Engineering, Osaka University
Hiroyuki Tawara	National Institute for Fusion Science
Kazuki Tsuchida	Energy Reserch Laboratory, Hitachi Ltd.
Tetsuya Watanabe	National Astronomical Observatory

CORRELATION EFFECTS FOR TWO-ELECTRON SYSTEMS

P.B.Ivanov* and U.I.Safronova**

*Kurchatov Atomic Energy Institute, Troitsk Branch,142092, USSR
**National Institute for Fusion Science, Nagoya 464-01, Japan *

1.Introduction

Correlation phenomena are of fundamental importance for autoionising states in two-electron ions, where the collective movement of atomic electrons dominates over self-consistency effects. The explicit evaluation of correlation diagrams in the theory of adiabatic S-matrix [1] describes doubly excited states as atomic states proper, though in some cases it is necessary to take into account their resonance nature. One of the most popular ways of theoretical extracting autoionization resonances from continuum is configuration-interaction (CI) theory [2], in wide variety of its branches. As an approximate solution of CI equation diagonalisation method has appeared in early 70's [3], and has been successively used to reveal resonance features in atomic reactions. It is natural to undergo the task of relating the results of diagonalisation approach (DA) to those of 1/Z perturbation theory (PT), as. in part, is fulfilled in present article.

2. General Formulae

Autoionising states in DA appear as resonancee in a continuum wave function

$$|aE\rangle = |aE\rangle + \sum_{\mu} |(\mu)E\rangle \frac{1}{E - E_{\mu} \pm i\Gamma_{\mu}/2} \langle(\mu)|H-E|aE\rangle , \qquad (1)$$

where "modified" autoionisation state vectors are

$$|(\lambda)E\rangle = |(\lambda)\rangle + \sum_{a} \int \frac{dE'}{E - E' \pm i0} |aE'\rangle\langle aE'|H-E|(\lambda)\rangle , \qquad (2)$$

and $|(\lambda)\rangle = \sum_{\mu} |\mu\rangle c_{\mu}^{\lambda}$ are obtained from the egenvalue problem

$$\sum_{\mu\upsilon} \{ E_{\mu}^{CI} \delta_{\mu\upsilon} + \beta_{\mu\upsilon}(E) \} c_{\upsilon}^{\lambda} = E^{\lambda} c_{\mu}^{\lambda} \qquad (3)$$

which is ordinarily solved perurbatively, expanding $E^{\lambda}=E^{\lambda}-\frac{i}{2}\Gamma^{\lambda}$ and c_{μ}^{λ} in powers of $\beta_{\mu\upsilon}$ given by

$$\beta_{\mu\upsilon}(E) = \sum_{a} \int dE' \frac{1}{E - E' \pm i0} \langle \mu| H-E |aE'\rangle\langle aE'| H-E |\upsilon\rangle \qquad (4)$$

Basis states in closed ($|\mu\rangle$) and open ($|aE\rangle$) channels are "prediagonalized", so that

$$\langle \mu \mid H-E \mid \upsilon \rangle = (E_\mu - E)\,\delta_{\mu\upsilon} \tag{5}$$

$$\langle aE' \; H-E \; bE'' \rangle = (E'-E)\,\delta_{\mu\upsilon}\,\delta(E'-E'') \tag{6}$$

THe procedure of prediagonalization in the open-channel subspace comes from the general scattering theory [4], and is destined to to provide physically correct asymptotic behavior of continuum wave functions. The primary basis for open-channel states consists usually of distorted-wave continuum orbitals coupled to unscreened core orbitals. Coulomb interaction between such states is then given by the matrix element.

$$V^{pp}_{aE,a'E'} = V^{pp}_{n_1 l_1 \varepsilon l_2, n'_1 l'_1 \varepsilon' l'_2} =$$

$$= \langle n_1 l_1(Z)\; \varepsilon l_2(Z-1) \left|\frac{1}{r_{12}}\right| n'_1 l'_1(Z)\; \varepsilon' l'_2(Z-1) \rangle -$$

$$- \delta(n_1 l_1 l_2, n'_1 l'_1 l'_2) \int_0^\infty dr\, r^2\, R_{\varepsilon l_2}(Z-1)\, \frac{1}{r}\, R_{\varepsilon' l'_2}(Z-1) \tag{6}$$

where the subtrahend cancels the divergent part in $\langle aE|\, 1/r_{12}\,|a'E'\rangle$. In the language of perturbation theory (PT) it means the summation of divergent terms in all orders of 1/Z energy expansion higher than the second [5].

Prediagonalized basis in the closed-channel subspace is obtained, as a rule, through the truncated CI procedure [6]:

$$|\mu\rangle = \sum_Q |Q\rangle\, c^\mu_Q \quad , \tag{8}$$

$$\sum_{Q'} \langle Q \mid H \mid Q'\rangle\, c^\mu_{Q'} = E^{CI}_\mu\, c^\mu_Q \tag{9}$$

- and primary basis vector $|Q\rangle = |Nln l';LSJM\pi\rangle$ are usual Slater states, constructed of unscreened Coulomb orbitals.

In the first order in $\beta_{\mu\upsilon}$ we write

$$E_\mu(E) = E^{CI}_\mu + \Delta_\mu(E) \tag{10}$$

$$\Delta_\mu(E) = \sum_a \int dE' \frac{1}{E-E'} \left| \langle \mu \mid H-E \mid aE' \rangle \right|^2 , \qquad (11)$$

$$\Gamma_\mu(E) = 2\pi \sum_a \left| \langle \mu \mid H-E \mid aE \rangle \right|^2 \qquad (12)$$

Energy dependence of resonance positions and widths is characteristic feature of DA. To introduce autoionizing state energies and widths as atomic constants, the resonance approximation is usually made:

$$E_\mu = E_\mu(E_\mu^{CI}) = E_\mu^{CI} + \Delta_\mu(E_\mu^{CI}) , \qquad (13)$$

$$\Gamma_\mu = \Gamma_\mu(E_\mu^{CI}) = 2\pi \sum_a \left| \langle \mu \mid H-E_\mu^{CI} \mid aE_\mu^{CI} \rangle \right|^2 \qquad (14)$$

As the summation in Eq.11 runs all over the complement of the {Q}-subspace, and E_μ^{CI} comprises total contribution of the first order in $V_{QQ'}$, energy (13) coincides with that of PT up to the second order. If non-degenerate configurations are included in primary basis, a part of higher-order corrections is summed through all the orders of PT.

3. Comparison of the CI and PT energies

In practice of DA, the correction (11) is included in autoionising-state energies only in a part, and often Δ_μ is is entirely omitted. Such approximation is justified only if CI energies, calculated on a sufficiently wide basis, account for a major part of the second-order terms. Hereafter we investigate the situation on the example $2s^2\ ^1S_o$ and $2p^2\ ^1S_o$ states .

For energy matrix we have in frame of two orders PT (we take into account terms $T^{(0)}$, $T^{(1)}$ and $T^{(2)}$ and for states $2s^2\ ^1S$ and $2p^2\ ^1S$ we shall use designations: "1" and "2")

$$T_{11} = -0.25\ Z^2 + 0.150390625\ Z - 0.037125$$

$$T_{22} = -0.25\ Z^2 + 0.216796875\ Z - 0.110552$$

$$T_{12} = -0.050743676\ Z - 0.030278 \qquad (15)$$

Usually, we obtain coefficients from solving Eq.(9) and take into account first order approximation and as a result we can find for coefficients C_Q^μ and for energy E_μ

$$E_1^{(1)}=0.122952 \qquad C_1^1 = a = 0.879640,\ C_1^2 = b = 0.475640$$

$$E_2^{(1)}=0.244235 \qquad C_2^1 = -b, \qquad C_2^2 = a \qquad (16)$$

With these coefficients we can recalculate the second order PT. Our results :

$$E_1^{(2)} = -0.028355, \qquad E_2^{(2)} = -0.119304\ , \qquad (17)$$

and for energy we obtain

$$E_1 = -0.25\ Z^2 + 0.122952\ Z - 0.028355$$

$$E_2 = -0.25\ Z^2 + 0.244235\ Z - 0.119304 \qquad (18)$$

The primary basis for the truncated HI had mixed configurations $2l n l'$ with $2 \leqslant n \leqslant 10$. A number of Z-values were taken in the range from Z=2 to Z=26. The calculation results are given in the Table 1. This Table is divided for three parts. The first part is the calculation results in units E/Z^2 (at.un.). The second part is the coefficients for Z-expansion like Eq.18. The third part is

$$X_2 = -\left(E - E^{(0)}Z^2 - E^{(1)}Z \right) \qquad (19)$$

These data we used for calculation $\mathcal{E}^{(2)}$ and $\mathcal{E}^{(3)}$ coefficients

$$-X_2 = \mathcal{E}^{(2)} + \mathcal{E}^{(3)}/Z \qquad (20)$$

in order to compare with exact calculations (in actually we can compare only $E^{(2)}$ and $\mathcal{E}^{(2)}$.

Results of these calculations are given in the Table 2. It is need to say, that the values of $\mathcal{E}^{(2)}$ and $\mathcal{E}^{(3)}$ depend on Z, but usually only in limit 10% for $\mathcal{E}^{(2)}$ and 30% for $\mathcal{E}^{(3)}$ except data for small Z (Z=3-5). These results we shall discuss on the example of $2s^2\ ^1S$ and $2p^2\ ^1S$ states. Instead (18) we have

$$E_1 = -0.25\ Z^2 + 0.122952\ Z - \left\{ \begin{matrix} 0.01975 \\ 0.01987 \end{matrix} \right. - \frac{1}{Z} \left\{ \begin{matrix} 0.00406 \\ 0.00295 \end{matrix} \right.$$

$$E_2 = -0.25\ Z^2 + 0.244235\ Z - \left\{ \begin{matrix} 0.05235 \\ 0.05183 \end{matrix} \right. - \frac{1}{Z} \left\{ \begin{matrix} 0.05608 \\ 0.06113 \end{matrix} \right. \qquad (21)$$

Two values for $\mathcal{E}^{(2)}$ and $\mathcal{E}^{(3)}$ mean the limit of changing these data with Z (Z=26 and Z=6). If we compare $\mathcal{E}^{(2)}$ and $\mathcal{E}^{(3)}$ we can

see that the absolute values of $\mathcal{E}^{(2)}$ and $\mathcal{E}^{(3)}$ are comparable.

The analogous data we obtained for 2lnl' states. We used data from the Tables 1,2 and C_Q^{μ} coefficients obtained after diagonalization of energy matrix in the same way as for $2s^2$, $2p^2$ states. The results of calculations are given in the Table 3.

From comparison $E^{(2)}$ (Eq.18) and $\mathcal{E}^{(2)}$ (Eq.21 and Tab.3) we can find difference in these data and we can conclude that CI method is given only part of second order PT. This part is equal a discrete-discrete part of second order PT [1] with limitation for one index nl=2s or 2p. We shall illustrate this on the same example of $2s^2$ $2p^2$ states. Matrix element of second order is represented in form:

$$T_{ij}^{(2)} = T(D,D) + T(D,C) + T(C,C) \qquad (22)$$

where these three components are designated discrete-discrete, discrete-continuous and continuous-continuous parts of sum for second order PT . For T(DD) part it possible to divide sum for three part else, pulling out sum with n=1 and n=2:.

$$T(D,D) = T(n,n) + T(2,n) + T(1,n) \qquad (23)$$

where n = 3 - ∞ . We shall show, that CI method takes into account only T(2,n) component. For $2s^2\ {}^1S$ we can write :

$$T_{11}^{(2)} = 0.022528 + 0.009615 + 0.004912 \qquad (24)$$

$$T(D,D) = 0.005693 + 0.0181586 - 0.001330 \qquad (25)$$

This example shows that T(2,n) part is equal only half of $T_{11}^{(2)}$. The analogous data we obtained for $2p^2\ {}^1S$ state. Recalculaton of these data with coefficients C_Q^{μ} from Eq.16 is given this part of second order correction:

$$E_1^{(2)}(D) = - 0.0202705, \qquad E_2^{(2)}(D) = - 0.0531519 \qquad (26)$$

Comparison of these data with data for $\mathcal{E}^{(2)}$ (see Eq.21) shows very good agreement.

We can conclude, that CI method takes into account only part of second order PT and we know now what is this part. In this case we can improve data obtained CI method if we shall add another part of second order PT (T(C,C), T(D,C), T(n,n), T(1,n)). From another side we shall improve data obtained PT method if we add third order correction from CI method ($\mathcal{E}^{(3)}$), because numerical calculation of third order PT ($E^{(3)}$) is very complicated.

Table 4 gives analogous data for 2s3p, 2p3s, 2p3d ($^{1,3}P$) states. Our CI calculations were done for ions with Z=2,6,18,26. with these data we calculated $\mathcal{E}^{(2)}$ and $\mathcal{E}^{(3)}$. There are in the Table 4, but accuracy of these data worse than accuracy of data

in the Table 3, because in this case we used only 4 values of Z. For all states the ratio $\xi_2^{(2)} / E_2^{(2)}$ is equal 0.5-0.6. This is the same difference as for $2s^2$ and $2p^2$ states that we explained before.

4.First Order PT for Decay Amplitude

Now we note that continuum wavefunctions practically exploited are only approximately prediagonalized, if ever. Naturally, screened hydrogenic primary basis makes the asymptotic of open-channel wavefunctions correct, and, for lower autoionizing states, it is sufficient to get satisfactory width estimates from Eq.12. We see, that DA zero-order autoionization amplitude

$$\gamma_{\mu,aE} = \langle \mu \mid H-E \mid aE \rangle = \sum_Q c_Q^\mu \langle Q \mid H-E \mid aE \rangle \qquad (27)$$

at $E = E_\mu^{CI}$, comprises total PT second-order contribution, plus higher-order terms arising from the summation of screening diagrams for continuum orbitals, as well as from the closed-channel prediagonalization procedure. Since the prediagonalization of open channels is independent on the choice of closed-chanell basis, it is convenient to consider primary autoionisation amplitude $\gamma_{Q,aE} = \langle Q \mid H-E \mid aE \rangle$, to oberve the effect of Coulomb interaction in continuum.

We can accomplish continuum prediagonalization in the first order in V^{pp}, Eq.7:

$$|aE\rangle \cong \sum_b \left\{ |bE\rangle_o + \sum_c \int \frac{dE'}{E - E'} |cE'_o\rangle V^{pp}_{cE',bE} \right\} \left\{ 1 - i\pi V^{pp}_{bE,aE} \right\}^{-1} \qquad (28)$$

Normalization factor in the form $(1 - i\pi V^{pp})^{-1}$ is required for the correct outgoing-wave asymptotic behaviour of $|aE\rangle$, but at higher Z we can retain only first order terms in Eq.28 moming to

$$|aE\rangle = |aE\rangle_o + \sum_b \int \frac{dE'}{E - E' - i0} |bE'\rangle_o V^{pp}_{bE',aE} \qquad (29)$$

where summation runs all over open-channel primary basis, including discrete values of energy. Substituting Eq.28 or (29). into Eq.27 we define first-order autoionisation amplitude in DA. Provided the complete summation is performed in Eq.28,29, the first-order correction to DA amplitudes comprises total of the value obtained in the third order of PT, screening diagrams being summed up. In practice, nevertheless, such complete summation never take place,

only physically open at a definite energy channels are summed over.

For $(2lnl')\ ^{2S+1}L_J$ levels, Coulomb decay is possible to have not more than one channel, so the nirmalization matrix in (28) reduces to just a complex factor, and only one-dimension summation is retained in DA autoionization amplitudes. Exploiting the analitical properties of primary amplitudes, this summation can be carried out all the infinity of discrete levels under threshold, and all energies over threshold. We can separete the whole correction into contributions of the discrete summation and the integral over continuous energy levels, but the first we discuss contributions of screening effect and first order correction. We represent the DA autoionization amplitudes (A(Q)) in a form:

$$A(Q) = A^{(0)}(1 + A^{S}/ Z + A^{(1)}/ Z) \qquad (30)$$

where $A^{(0)}$ is the value of amplitude in hydrogenic approximation, $A^{(0)}(1 + A^{S}/ Z)$ is the value of amplitude obtained with V^{pp} defined Eq.6., and $A^{(1)}$ is the first order correction. The Table 5 gives result for these values . We considered $2sns\ ^1S$ states for Z= 2 -26.

We can see from the Table 5 that $A^{(S)}$ and $A^{(1)}$ are rather stable and independent of Z. The other things is very interesting, A^{S} and $A^{(1)}$ have different sign (A^{S} is positive and $A^{(1)}$ is negative) and a result they are almost delete each other. Especially this is true for $2s^2\ ^1S$ state. For all states the values of A^{S} and $A^{(1)}$ are almost 1 and we can conclude that for ions with high Z this is not very big corrections and in this case it is possible to use only $A^{(0)}$. This is rather good conclusion because many data for H-like satellite line were prepared by one of the other of this article (see, an example, Ref.7) in hydrogenic approximation.

* Permanent addres: Institute of Spectroscopy, Academy of Sciences of the USSR, Troitsk, Moscow region, 142092, USSR

References

1) E.V.Aglitskii and U.I.Safrponova, Spestroscopy of Autoionising States of Atomic Systems (in Russian),Moscow (1985)
2) U.Fano, Phys.Rev.,124, 1866 (1961)
3) V.V.Balashov et.al., Optics and Spectroscopy, 38, 859 (1970)
4) G.Howat, T.Aberg and O.Goscinski, J.Phys., B11, 1575 (1078)
5) A.Yu.Matulis and U,I.Safronova, Optics and Spectroscopy, 28, 1076 (1970)
6) L.Lipsky, A.Russek, Phys.Rev., 142, 59 (1966)
7) L.A.Vainshtein and U.I.Safronova, Atomic Data and Nuclear Data Tables, 21, 49 (1978)

Table 1. The values of energy E for 2lnl ^{1}S states, obtained from CI calculation $X=E/Z^2$, $X_2 = -(E-E^{(0)}Z^2-E^{(1)}Z)$

Z	$X(2s^2)$	$X(2p^2)$	X(2s3s)	X(2p3p)	X(2s4s)	X(2p4p)
2	0.193763	0.201904	0.146596	0.136200	0.135768	0.131613
3	0.211323	0.220111	0.156630	0.146316	0.141666	0.137341
4	0.220549	0.227448	0.162133	0.152864	0.144983	0.141012
5	0.226228	0.231424	0.165609	0.157387	0.147090	0.143521
6	0.230073	0.233898	0.167993	0.160688	0.148545	0.145349
7	0.232849	0.235581	0.169727	0.163194	0.149606	0.146739
8	0.234947	0.236796	0.171042	0.165154	0.150413	0.147828
9	0.236588	0.237714	0.172074	0.166725	0.151046	0.148700
10	0.237906	0.238432	0.172905	0.168011	0.151558	0.149414
12	0.239893	0.239480	0.174159	0.169986	0.152326	0.152326
16	0.242394	0.240743	0.175739	0.172527	0.153297	0.151908
20	0.243902	0.241477	0.176694	0.174087	0.153883	0.152763
26	0.245301	0.242139	0.177579	0.175549	0.154426	0.153560
$E^{(0)}$	-0.25	-0.25	-0.180555	-0.180555	-0.15625	-0.15625
$E^{(1)}$	0.122952	0.244235	0.77843	0.132483	0.047628	0.070360
$E^{(2)}$	-0.02835	-0.11930	-0.0287	-0.1050	-0.0198	-0.0521
Z	$X_2(2s^2)$	$X_2(2p^2)$	X_2(2s3s)	X_2(2p3p)	X_2(2s4s)	X_2(2p4p)
2	0.020956	0.084663	0.019848	0.087544	0.013328	0.042178
3	0.020763	0.072373	0.018197	0.089289	0.011804	0.040889
4	0.020592	0.067147	0.016607	0.086876	0.010232	0.037640
5	0.020460	0.064057	0.015547	0.083198	0.009149	0.033571
6	0.020340	0.062019	0.014815	0.079666	0.008397	0.029733
7	0.020265	0.060579	0.014286	0.076647	0.007858	0.026486
8	0.020224	0.059511	0.013888	0.074148	0.007455	0.023841
9	0.020196	0.058687	0.013579	0.072089	0.007145	0.021704
10	0.020120	0.058033	0.013332	0.070382	0.006800	0.019969
12	0.020077	0.057061	0.012964	0.067746	0.006538	0.017369
16	0.020000	0.055864	0.012508	0.064369	0.006098	0.014198
20	0.019500	0.055156	0.012239	0.062322	0.005840	0.012379
26	0.019900	0.054508	0.011993	0.060433	0.005608	0.010772

Table 2.The values of $\mathcal{E}^{(2)}$, $\mathcal{E}^{(3)}$ for Z-expansion CI energy

$$E(CI) = E^{(0)}Z^2 + E^{(1)}Z + \mathcal{E}^{(2)} + \mathcal{E}^{(3)}/Z$$

Z	$\mathcal{E}^{(2)}(2s^2)$	$\mathcal{E}^{(2)}(2p^2)$	$\mathcal{E}^{(2)}(2s3s)$	$\mathcal{E}^{(2)}(2p3p)$	$\mathcal{E}^{(2)}(2s4s)$	$\mathcal{E}^{(2)}(2p4p)$	$\mathcal{E}^{(2)}(2s5s)$
3	-0.02039	-0.04779	-0.01490				-0.00681
4	-0.02008	-0.05147	-0.01184				-0.00359
5	-0.01993	-0.05169	-0.01131	-0.06849	-0.00481		-0.00243
6	-0.01987	-0.05183	-0.01116	-0.06201	-0.00464	-0.01055	-0.00200
7	-0.01983	-0.05194	-0.01111	-0.05853	-0.00462	-0.00700	-0.00191
8	-0.01981	-0.05203	-0.01110	-0.05665	-0.00464	-0.00532	-0.00190
9	-0.01980	-0.05210	-0.01111	-0.05562	-0.00466	-0.00461	-0.00192
10	-0.01979	-0.05215	-0.01111	-0.05502	-0.00469	-0.00436	-0.00202
12	-0.01978	-0.05220	-0.01112	-0.05457	-0.00473	-0.00436	-0.00195
16	-0.01976	-0.05227	-0.01114	-0.05423	-0.00478	-0.00469	-0.00206
20	-0.01785	-0.05232	-0.01116	-0.05414	-0.00481	-0.00510	-0.00211
26	-0.01975	-0.05235	-0.01117	-0.05414	-0.00483	-0.00541	-0.00214
$E^{(2)}$	-0.02835	-0.11930	-0.028	-0.1050	-0.0198	-0.0521	-0.0142

Z	$\mathcal{E}^{(3)}(2s^2)$	$\mathcal{E}^{(3)}(2p^2)$	$\mathcal{E}^{(3)}(2s3s)$	$\mathcal{E}^{(3)}(2p3p)$	$\mathcal{E}^{(3)}(2s4s)$	$\mathcal{E}^{(3)}(2p4p)$	$\mathcal{E}^{(3)}(2s5s$
3	-0.00156	-0.07374	-0.00990				-0.00671
4	-0.00205	-0.06271	-0.01908				-0.01638
5	-0.00264	-0.06181	-0.02120	-0.07346	-0.02167		-0.02105
6	-0.00295	-0.06113	-0.02196	-0.10595	-0.02254	-0.11512	-0.02307
7	-0.00315	-0.06046	-0.02222	-0.12682	-0.02268	-0.13638	-0.02375
8	-0.00329	-0.05986	-0.02228	-0.13994	-0.02254	-0.14841	-0.02384
9	-0.00341	-0.05885	-0.02226	-0.14787	-0.02232	-0.15386	-0.02365
10	-0.00350	-0.05885	-0.02220	-0.15359	-0.02206	-0.15612	-0.02274
12	-0.00360	-0.05829	-0.02209	-0.15816	-0.02171	-0.15605	-0.02340
16	-0.00375	-0.05747	-0.02188	-0.16213	-0.02115	-0.15217	-0.02217
20	-0.00391	-0.05667	-0.02159	-0.16370	-0.02061	-0.14557	-0.02131
26	-0.00406	-0.05608	-0.02129	-0.16372	-0.02009	-0.13927	-0.02063

Table 3. Z-coefficients for energy $2lnl'(^1S)$ states

$$E_Q = E^{(0)}Z^2 + E^{(1)}Z + \mathcal{E}^{(2)} + \mathcal{E}^{(3)}/Z$$

	2s3s	2p3p	2s4s	2p4p	2s5s
$E^{(0)}$	-13/72	-13/72	-5/32	-5/32	-29/200
$E^{(1)}$	0.077843	0.132483	0.0476280	0.073601	0.0322245
$\mathcal{E}_1^{(2)}$	-0.0149	-0.068	-0.00481	-0.070	-0.0020
$\mathcal{E}_2^{(2)}$	-0.0112	-0.054	-0.00483	-0.054	-0.0021
$\mathcal{E}_1^{(3)}$	-0.01	-0.073	-0.022	-0.12	-0.023
$\mathcal{E}_2^{(3)}$	-0.02	-0.163	-0.020	-0.14	-0.021
$E^{(2)}$	-0.0287	-0.1050	-0.0198	-0.0520	-0.0142

Table 4. The values of X_2 from CI calculations and the values of $E^{(0)}$, $E^{(1)}$, $E^{(2)}$, $\mathcal{E}^{(2)}$ $\mathcal{E}^{(3)}$ for Z-expansion energy $E(CI) = E^{(0)}Z^2 + E^{(1)}Z + \mathcal{E}^{(2)} + \mathcal{E}^{(3)}/Z$, $E(PT) = E^{(0)}Z^2 + E^{(1)}Z + E^{(2)}$

Z	$X_2(2s2p\,^1P)$	$X_2(2s2p\,^3P)$	$X_2(2s3p\,^1P_+)$	$X(2s3p\,^1P_-)$	$X(2p3d\,^1P)$
2	0.06917660	0.0233513	0.05458273	0.01253970	0.07629096
6	0.06702173	0.0213438	0.04785370	0.01125566	0.06241010
18	0.06370603	0.0204701		0.01077850	0.05241480
26	0.06311130	0.0203307	0.03438270	0.01072776	0.05098314
$E^{(0)}$	-0.25	-0.25	-0.1805555	-0.18055555	-0.18055555
$E^{(1)}$	0.19140625	0.1328125	0.109305	0.0692263	0.126064
$E^{(2)}$	-0.096872	-0.027688	-0.073229	-0.0145429	-0.087012

Z	$\mathcal{E}^{(2)}(2s2p\,^1P)$	$\mathcal{E}^{(2)}(2s2p\,^3P)$	$\mathcal{E}^{(2)}(2s3p\,^1P_+)$	$\mathcal{E}^{(2)}(2s3p\,^1P_-)$	$\mathcal{E}^{(2)}(2p3d\,^1P)$
2	-0.0659442	-0.0203401	-0.0444892	-0.0106136	-0.0554697
6	-0.0620482	-0.0200332		-0.0105399	-0.0474172
18	-0.0617732	-0.0200173		-0.0106136	-0.0477619

Z	$\mathcal{E}^{(3)}(2s2p\,^1P)$	$\mathcal{E}^{(3)}(2s2p\,^3P)$	$\mathcal{E}^{(3)}(2s3p\,^1P_+)$	$\mathcal{E}^{(3)}(2s3p\,^1P_-)$	$\mathcal{E}^{(3)}(2p3d\,^1P)$
2	-0.006465	-0.0060225	-0.0201871	-0.0038521	-0.0416426
6	-0.029841	-0.0078636		-0.0042944	-0.0899577
18	-0.034792	-0.0081502		-0.0029683	-0.0837520

Z	$X_2(2s3p\,^3P_+)$	$X_2(2s3p\,^3P_-)$	$X_2(2p3d\,^3P)$	$X_2(2p3d\,^3D)$
2	0.02186742	0.0219858	0.0495106	0.04911186
6	0.01950372	0.0146844	0.0363941	0.0385796
18	0.01850072	0.0117854	0.0318776	0.0349565
26	0.01832160	0.0113618	0.0312144	0.0343784
$E^{(0)}$	-0.18055555	-0.1805555	-0.1805555	-0.1805555
$E^{(1)}$	0.0831808	0.0809653	0.1123085	0.1045114
$E^{(2)}$	-0.021651	-0.022650	-0.038882	-0.057637

Z	$\mathcal{E}^{(2)}(2s3p\,^3P_+)$	$\mathcal{E}^{(2)}(2s3p\,^3P_-)$	$\mathcal{E}^{(2)}(2p3d\,^3P)$	$\mathcal{E}^{(2)}(2p3d\,^3D)$
2	-0.0184719	-0.0110337	-0.0298358	-0.0333135
6	-0.0179492	-0.0103330	-0.0296193	-0.0331449
18	-0.0179186	-0.0104132	-0.0297223	-0.0330777

Z	$\mathcal{E}^{(3)}(2s3p\,^3P_+)$	$\mathcal{E}^{(3)}(2s3p\,^3P_-)$	$\mathcal{E}^{(3)}(2p3d\,^3P)$	$\mathcal{E}^{(3)}(2p3d\,^3D)$
2	-0.0067909	-0.0219042	-0.0393495	-0.0365963
6	-0.0099274	-0.0261086	-0.0406488	-0.0326079
18	-0.0104785	-0.0246642	-0.0387954	-0.0338190

Table 5. Autoionization Amplitudes of 2sns ^1S states (at.un.)

$A(Q) = A^{(0)}(1 + A^S/Z + A^{(1)}/Z)$, A^S -a, $A^{(1)}$-b.

Z		2s2s	2s3s	2s4s	2s5s	2s6s	2s7s
	$A^{(0)}$	0.0281196	0.0200220	0.0127109	0.0090056	0.0068105	0.0053933
2	a	0.42900	0.41238	0.39967	0.39275	0.39040	0.38553
	b	-0.91615	-0.87115	-0.85385	-0.84562	-0,84170	-0.83814
3	a	0.58142	0.59691	0.59101	0.58657	0.58622	0.58081
	b	-0.79938	-0.75910	-0.74107	-0.73596	-0.73238	-0.72917
4	a	0.64473	0.69386	0.69556	0.69398	0.69580	0.69008
	b	-0.72766	-0.69241	-0.67846	-0.67176	-0.66856	-0.66566
5	a	0.67885	0.76148	0.77087	0.77221	0.77619	0.77021
	b	-0.68659	-0.65470	-0.64190	-0.63574	-0.63227	-0.63018
6	a	0.71479	0.86378	0.88842	0.89559	0.90389	0.89741
	b	-0.66659	-0.63195	-0.61993	-0.61414	-0.61138	-0.60883
7	a	0.72014	0.88561	0.91405	0.92266	0.93199	0.92543
	b	-0.64527	-0.61754	-0.60616	-0.60065	-0.59802	-0.59557
8	a	0.72550	0.90745	0.93968	0.94973	0.96010	0.95346
	b	-0.63459	-0.60830	-0.59741	-0.59213	-0.58961	-0.58725
9	a	0.73374	0.94853	0.98832	1.00126	1.01386	1.00689
	b	-0.62752	-0.60246	-0.59197	-0.58689	-0.58447	-0.58217
10	a	0.74032	0.98787	1.03521	1.05104	1.06576	1.05855
	b	-0.62297	-0.59898	-0.58886	-0.58394	-0.57787	-0.57937
12	a	0.75000	1.06320	1.12553	1.14716	1.16614	1.15844
	b	-0.61857	-0.59672	-0.58723	-0.58259	-0.58041	-0.57827
16	a	0.76332	1.20660	1.29900	1.33201	1.35949	1.35081
	b	-0.62160	-0.60262	-0.59414	-0.58997	-0.58805	-0.58604
20	a	0.77204	1.34538	1.46770	1.51215	1.54811	1.53811
	b	-0.63139	-0.61502	-0.60743	-0.60365	-0.60194	-0.60005
26	a	0.78153	1.54970	1.71686	1.77850	1.82710	1.81554
	b	-0.65140	-0.63848	-0.63190	-0.62864	-0.62721	-0.62545

Relativistic Configuration Interaction Method

Takashi Kagawa
Department of Physics, Nara Women's University
Nara 630, Japan

Abstract: Based on the projection operator method, the relativistic configuration interaction (RCI) method for many-body systems is presented. In this method, a variational one-body potential v(r) is introduced into a Hamiltonian and both a projection operator and a RCI wavefunction are constructed from the eigenfunctions for the one-body Hamiltonian involving v(r). This method is useful when one obtains variationally an optimum one-body projection operator used for constructing a relativistic many-body Hamiltonian without a disease of "variational collapse". Numerical applications of the method to helium-like atomic systems are carried out.

1. Introduction

In the nonrelativistic quantum theory, variation method has widely been used for calculating the ground-state energy in many-body systems such as atoms and molecules. In this case the variational principle is used as a minimum principle as well as a stationary one. However, in the relativistic quantum mechanics, the situation is very different from the nonrelativistic one. Brown and Ravenhall[1] have pointed out that the relativistic wave equation for many-body systems does not yield a normalizable wavefunction for a bound state because not only the positive-energy bound and continuum solutions but also negative-energy continuum ones are obtained with the wave equation. This means that there are an infinite number of configurations containing pairs of the positive- and negative-continuum states which yield the same energy as

that for a bound state if the two-body interaction is neglected in the Hamiltonian. However, when this interaction is taken into account, these configurations are mixed with the normalizable bound state wavefunction in the configuration interaction scheme, so that a total wavefunction becomes a unnormalizable function. Moreover, variational solutions for the relativistic wave equation cannot be obtained as an upper bound for the exact energy value of the ground state in a system since the spectrum of a relativistic Hamiltonian is not bounded from below due to the negative-energy continuum states.

Problems on the elimination of the contamination of negative-energy states in the relativistic calculations for the ground state in many-body systems have so far been investigated by various authors. One of ways to avoid the variational collapse is that one uses a modified Hamiltonian whose energy spectrum is bounded from below. Along this line, two approaches have been proposed: One is the projection operator method proposed by some authors such as Brown and Ravenhall[1], Mitteleman[2] and Sucher[3]. The other is the squared Hamiltonian method by Wallmeier et. al.[4].

In this report, the relativistic configuration interaction (RCI) method is presented, where the projection operator method is modified by introducing a variational one-body potential into a Hamiltonian in order to eliminate tedious treatment in the evaluation of expectation values for the Hamiltonian with the projection operator. The same type of the Hamiltonian which can be used for the variational calculation has already been proposed by Mitteleman[2]. Here, we modify the RCI method as follows: The RCI calculation is carried out under an condition that the one-body variational potential introduced is used to produce a complete set of basis functions which both the projection operator and the configuration state functions (CSF's) are constructed from. This condition leads to the most simplified treatment for the projection operator, namely, one can omit a projection operator in the relativistic

Hamiltonian when calculating the Hamiltonian matrix elements with respect to these CSF's. In addition, the modification involves another interesting feature that one can variationally obtain an optimum projection operator which a relativistic many-body Hamiltonian without a disease of "variational collapse" can be constructed with.

Numerical application of the method to helium-like atomic systems are carried out.

2. Relativistic Configuration Interaction Method

For atomic systems, a relativistic Hamiltonian in atomic units is written as a sum of the Dirac Hamiltonian $H_D(i)$ and the two-electron operator $g(i,j)$ due to the Coulomb and the Breit interactions between electrons as follows,

$$H = \sum_i H_D(i) + \sum_i \sum_j g(i,j), \tag{1}$$

where

$$H_D(i) = c\vec{\alpha}_i \cdot \vec{p}_i + c^2\beta_i - Z/r_i \ , \tag{2}$$

and c is the velocity of light and Z is the atomic number. $\vec{\alpha}$ and β are the Dirac operators in the matrix form. The two-electron operators $g(i,j)$ is written as

$$g(i,j) = \frac{1}{r_{ij}} + H_B(i,j), \tag{3}$$

where $H_B(i,j)$ is an operator for the Breit interaction given by

$$H_B(i,j) = -\frac{\vec{\alpha}_i \cdot \vec{\alpha}_j}{r_{ij}} - \frac{1}{2}(\vec{\alpha}_i \cdot \vec{\nabla}_i)(\vec{\alpha}_j \cdot \vec{\nabla}_j)\, r_{ij}. \tag{4}$$

We neglect the Breit interaction in an approximate Hamiltonian for the systems under consideration since the Breit interaction energy is α^2 order smaller in magnitude than the Coulomb interaction one between electrons, where α is the fine structure constant.

Following Sucher[3], we start with the wave equation for an atomic system with N electrons given by

$$H_+ \Psi = E \Psi, \tag{5}$$

where

$$H_+ = \sum_i \{H_D(i) + v(i)\} + \Lambda_+ \{\sum_i \sum_j \frac{1}{r_{ij}} - \sum_i v(i)\} \Lambda_+, \tag{6}$$

and $v(i)$ is a variational potential and Λ_+ is a projection operator onto the positive-energy states. Λ_+ is expressed as a product of single-particle projection operators $\Lambda_+(i)$ in the following,

$$\Lambda_+ = \Lambda_+(1)\Lambda_+(2)\cdots\cdots\Lambda_+(N), \tag{7}$$

where

$$\Lambda_+(i) = \sum_m |\psi_m^{(+)}(i) \quad \psi_m^{(+)}(i)|. \tag{8}$$

Here, $\psi_m^{(+)}(i)$ denotes an eigenfunction belonging to the mth positive-energy eigenstate for a single-particle Hamiltonian $H_0(i)$ written as

$$H_0(i) = H_D(i) + v(i). \tag{9}$$

The eigenvalue equation for $H_0(i)$ is given by

$$H_0(i) \ \psi_m^{(+)}(i) = \varepsilon_m^{(+)} \ \psi_m^{(+)}(i), \tag{10}$$

where $\varepsilon_m^{(+)}$ is a positive-energy eigenvalue.

A four-component eigenfunction $\psi^{(+)}(\vec{r})$ is expressed as

$$\psi^{(+)}_{n\kappa m}(\vec{r}) = \frac{1}{r}\begin{pmatrix} P_{n\kappa}(r)\ \chi_{\kappa m}(\theta,\phi) \\ iQ_{n\kappa}(r)\ \chi_{-\kappa m}(\theta,\phi) \end{pmatrix} \tag{11}$$

where $P_{n\kappa}(r)$ and $Q_{n\kappa}(r)$ are the large and small components of a radial wavefunction, respectively. $\chi_{\kappa m}(\theta,\phi)$ is a two-component spinor and κ is the relativistic angular momentum quantum number.

We write a total configuration interaction (CI) wavefunction $\Psi(\Gamma)$ belonging to a Γ symmetry species as a linear combination of configuration state functions (CSF's) $\Phi(\Gamma)$, given by

$$\Psi(\Gamma) = \sum_n c_n \Phi_n(\Gamma), \tag{12}$$

where c_n is an expansion coefficient and each CSF is constructed as a product of appropriate basis functions. As has been mentioned before, our RCI method requires that a CSF $\Phi(\Gamma)$ in eq. (12) is constructed with the same basis functions as $\{\psi^{(+)}_m(i)\}$ contained in Λ_+ in eq. (8). This requirement for constructing CSF's makes it possible that the evaluation of matrix elements for H_+ in eq. (6) can be carried out with neglecting the positive-energy projection operator Λ_+ in H_+.

For the wave equation in eq. (5), the variational principle can be used as a minimum principle, so that the minimum variational energy for the lowest state with a Γ symmetry in the system can be obtained by varying not only the expansion coefficients $\{c_n\}$ but also the variational potential $v(r)$, which leads to the change of both the projection operator and CSF's constructed with the same basis functions $\{\psi^{(+)}_m(i)\}$.

3. Calculated Results for Helium-Like Systems.

Here we apply the method to helium-like systems as the simplest many-electron system to see the effectiveness of the method. For simplicity, a Coulombic potential having a

variational parameter δ is taken as a variational potential v(i) in the relativistic Hamiltonian for the systems, written as

$$v(i) = \frac{Z-\delta}{r_i} . \tag{13}$$

The first H_0 and second H'_+ terms in the Hamiltonian H_+ in eq. (6), are given in the following forms, respectively,

$$H_0 = \sum_{i=1}^{2} H_0(i) = \sum_{i=1}^{2} \{H_D(i) + \frac{Z-\delta}{r_i}\}, \tag{14}$$

and

$$H'_+ = \Lambda_+ \{ \frac{1}{r_{12}} - \frac{Z-\delta}{r_1} - \frac{Z-\delta}{r_2} \} \Lambda_+ . \tag{15}$$

In this case, the Dirac orbitals for hydrogen-like systems containing a variational parameter δ instead of the atomic number Z form a basis set in the RCI method. These orbitals are used to construct both a RCI wavefunction and a projection operator $\Lambda_+(i)$ in eq.(8) for the systems.

By varying a variational parameter δ in v(i) in eq. (13), numerical calculations for the ground and some lower excited states in helium-like systems with Z=2, 10, 50 and 100 are caried out. Using the same variational potential as v(i) in eq. (13), we also make nonrelativistic CI calculations for the ground state in these systems to see the difference between the relativistic and nonrelativistic results, where the Dirac Hamiltonian $H_D(i)$ in H_0 in eq. (9) is replaced by the Schrödinger Hamiltonian for the hydrogen-like systems in the nonrelativistic calculations.

The seven hydrogenic Dirac orbitals (1s, 2s, $2p_{1/2}$, $2p_{3/2}$, 3s, $3p_{1/2}$, and $3p_{3/2}$) are used in the RCI

calculations for all states in the systems, whereas the corresponding non-relativistic hydrogenic orbitals, that is, 1s, 2s, 2p, 3s, and 3p ones are used in the NRCI calculations.

In Table 1, the RCI and NRCI results for the ground state in the helium-like systems with Z=2, 10, 50 and 100 are listed together with the values obtained with the Dirac-Hartree-Fock (DHF)[5,6], nonrelativistic Hartree-Fock (NRHF)[7] and exact nonrelativistic calculations[8], and experimental values[9]. Both the DHF values in the table are obtained with the point charge approximation for the nucleus. The RCI energies for the ground state obtained with the limited hydrogenic basis set are not good compared with the DHF ones for all the systems considered here. The same behavior for the energy value between the NRCI and NRHF calculations can be observed in the table. This means that the hydrogenic basis set does not yield good convergence both in the RCI and NRCI calculations for the ground state in a system, though the calculation can be carried out analytically.

The energy difference between the RCI and the NRCI methods increases as the atomic number Z becomes large since in heavier atomic systems the electron correlation effects become much smaller than the relativistic effects most of which are accounted for with the Dirac Hamiltonian. This can be confirmed by comparing the calculated results with experiment between the systems with Z=10 and 2: The discrepancy between the RCI or the DHF total energies and experiment for the ground state in helium-like neon (Z=10) becomes much smaller than that between the norelativistic energies and experiment, while it is not the case for Z=2, namely, the RCI and DHF results for the ground state in helium are not good compared with the exact nonrelativistic value[10] which is close to experiment.

In Table 2, values of the CSF expansion coefficients in the RCI and the NRCI calculations for the ground state in each system are listed. One sees from the table that the

value of the expansion coefficient for the $1s^2$ main configuration increases rapidly toward the maximum value of unity when atomic number Z becomes large. This means that the wavefunction for the ground state in very heavy two-electron atomic systems can well be approximated by a single jj-coupling congiguration wavefunction.

The calculated RCI energies for some lower excited states such as 2^3S_1 and $2^3P_{0,1,2}$ in the systems are listed in Table 3 together with the NRHF[11] and the exact nonrelativistic[10] ones and the experimental values[9]. The RCI energy values for all the excited states in neutral helium considered here are higher than not only the exact nonrelativistic energies but also the NRHF ones. Moreover, the order of the magnitude of the RCI energies for the fine structure in the 2^3P state in helium does not agree with experiment, that is, the RCI energy values for the three 2^3P states having J=0, 1 and 2 in helium are in the reverse order of the energies observed for them. However, the RCI energies for the $2^3P_{0,1,2}$ states as well as the 2^3S_1 one in helium-like neon (Z=10) are much close to experiment compared with the results for helium. This shows the rapid increase of the relativistic effects in the lower excited states as well as the ground state in atomic systems when the atomic number Z increases.

The CSF expansion coefficients for each state in the systems are listed in Table 4. From the table, one observes the same behavior of the coefficients for the main CSF in each excited state as that for the ground state when the atomic number Z increases: The coefficient for the main configuration in each state increases as the atomic number Z becomes large so that the total wavefunction for heavier atomic systems is also described appropriately by the single jj-coupling wavefunction. This means that the independent particle model such as the DHF one becomes an good approximation for high Z atomic systems because of the strong nuclear potential. If we start with the DHF potential for v(r) in the RCI calculation, improvement beyond the DHF

method could be obtained. However, in this case we have to deal with the numerical wavefunctions in the calculation.

4. Discussion

Here, any higher order effects such as the Breit interaction and the Lamb shift correction including the vacuum polarization on the total energy are not taken into account. Although the magnitude of these higher-order corrections to the total energy for lighter atomic systems is fairly small, they play an important role in dertermining the fine structure levels in the state such as the 2^3P one. However, the method of calculating the Lamb shift energy for many-electron systems is not established, yet. This has often been estimated for many-electron atomic systems by using a modified formula of the Lamb shift correction for one-electron atoms.

In order to obtain an accurate total energy for atomic systems with these higher-order corrections as a first-order perturbation, a much more accurate unperturbed wavefunction for a state in the systems than that obtained with the present RCI calculation will be needed. The MCDF method has widely been used to obtain the multiplet structure of the energy levels in various atomic systems. However, sometimes one encounters an difficulty in getting the Dirac orbitals in the MCDF scheme when the number of configuration increases. This means that one cannot always obtain an appropriate solution in the MCDF method. As the RCI method dose not deal with an additional inhomogeneous wave equation for the Dirac orbitas, this problem does not happen in this case. The deficiency of using the CI method is that the convergence is very slow. Moreover, in the RCI calculation, the contribution from the positive-energy continuum states to the total energy cannot be taken into account because of the difficulty in evaluating matrix elements with continuum wavefunctions. From these reasons, one could not expect that the RCI method based on the projection operator yields the electron correlation energy satisfactorily, even if a

different one-electron variational potential is chosen. On the other hand, it is expected that the total wavefunction for a system will be obtained so as to describe the relativistic effects in each electron appropriately since the inner- and outer-electrons have a different intermediate coupling between the LS- and jj-couplings depending on the magnitude of the relativistic effects.

5. Concluding Remarks

Based on the projection operator method, the relativistic configuration interaction (RCI) method for many-body systems is presented. To facilitate the numerical calculation for the relativistic wave equation containing projection operators, a variational one-body potential $v(r)$ is introduced into a Hamiltonian, where both a projection operator and a RCI wavefunction are constructed from the eigenfunctions for the one-body Hamiltonian involving $v(r)$. This leads to the most simplified treatment for the projection operator, namely, one can take no account of the projection operator in the relativistic Hamiltonian. Assuming the variational Coulombic potential and using a small size of a basis set, numerical applications of the method to helium-like atomic systems are carried out. Although the RCI method does not yield the correlation energy, it could be used to calculate the various physical quantities in heavier atomic systems with Z more than 50 since the relativistic effects can be taken into account sufficiently with the method.

References

(1) G.E. Brown and D.G. Ravenhall: Proc. R. Soc. London Ser. A208, 552 (1951).

(2) M. Mitteleman: Phys. Rev. A5, 2395 (1972), Phys. Rev. A24, 1167 (1981).

(3) J. Sucher: Phys. Rev. A22, 348 (1980).

(4) H. Wallmeier and W. Kutzelnigg: Chem. Phys. Lett. 78, 341 (1981) and H. Wallmeier: Phys. Rev. A29, 2993 (1984).

(5) S. Kiyokawa: Private communication.

(6) S.P. Goldman: Phys. Rev. A37, 16 (1988).

(7) C.C.J. Roothaan, L.M. Sachs, and A.W. Weiss: Rev. Mod. Phys. 32, 186 (1960).

(8) C. L. Pekeris: Phys. Rev. 112, 1649 (1958).

(9) C.E. Moor: NSRDS-NBS 34, Nat. Stand. Ref. Data Ser., Nat. Bur. Stand.(U.S.) (Sept. 1970); S. Bashkin and J.O. Stoner, Jr.: Atomic Energy Levels and Grotorian Diagrams, Vol. I, Hydrogen I - Phosphorus XV, North-Holland, Amsterdam, 1975. We use the same Rydberg constants R_M as a conversion factor as those in reference 23, that is, R_M = 109722.267 cm^{-1} for Z=2 and R_M = 109734.297 cm^{-1} for Z=10.

(10) Y. Accad, C.L. Pekeris, and B. Shiff: Phys. Rev. A4, 516 (1971).

(11) C. Froese-Fisher: J. Chem. Phys. 47, 4010 (1967).

Table 1. The calculated energies for the ground state (1^1S_0) in helium-like systems in atomic units.

Method	Z=2	Z=10	Z=50	Z=100
RCI(Coul.)	-2.858563	-93.97651	-2556.444	-11796.84
NRCI(Coul.)	-2.859822	-93.85582	-2468.855	-9937.605
DHF[a)]	-2.861813	-93.98279	-2556.452	-11796.86
DHF[b)]	-2.8618134	-93.982799		
NRHF[c)]	-2.86168	-93.86111		
Exact(NR)[d)]	-2.9037244	-93.906805		
Exp.[e)]	-2.9037844	-94.008358		

a) Reference 5.
b) Reference 6.
c) Reference 7.
d) Reference 8.
e) Reference 9.

Table 2. The RCI and NRCI energies, exponents and the CSF expansion coefficients for the ground state in helium-like systems.

CSF[a)]	Z=2	Z=10	Z=50	Z=100
RCI				
Energy	-2.858563	-93.97651	-2556.444	-11796.84
Exponent	1.783	9.737	49.75	99.83
$1s^2$	0.989142	0.999874	0.999995	0.999996
1s2s	-0.134618	-0.014016	-0.002892	-0.002490
$2s^2$	-0.022693	-0.003143	-0.000658	-0.000490
$2p-^2$	0.010623	0.001694	0.000323	0.000146
$2p+^2$	0.014909	0.002386	0.000430	0.000153
1s3s	-0.048384	-0.005304	-0.001088	-0.000921
2s3s	-0.009987	-0.001986	-0.000429	-0.000313
$3s^2$	-0.004683	-0.000693	-0.000144	-0.000103
2p-3p-	0.007026	0.001128	0.000213	0.000093
$3p-^2$	0.002308	0.000383	0.000072	0.000031
2p+3p+	0.009938	0.001594	0.000293	0.000111
$3p+^2$	0.003265	0.000542	0.000101	0.000041
NRCI				
Energy	-2.859822	-93.85582	-2468.855	-9937.605
Exponent	1.786	9.737	49.74	99.73
$1s^2$	0.988251	0.999867	0.999995	0.999999
1s2s	-0.138525	-0.014065	-0.002674	-0.001247
$2s^2$	-0.022964	-0.003142	-0.000593	-0.000295
$2p^2$	0.024989	0.004073	0.000794	0.000395
1s3s	-0.049690	-0.005315	-0.001021	-0.000472
2s3s	-0.014505	-0.002064	-0.000392	-0.000195
$3s^2$	-0.004651	-0.000689	-0.000131	-0.000065
2p3p	0.016953	0.002722	0.000527	0.000263
$3p^2$	0.005546	0.000917	0.000178	0.000088

a) p- and p+ mean $p_{1/2}$ and $p_{3/2}$, respectively.

Table 3. The RCI and other nonrelativistic energies for lower excited states in helium-like systems in a.u..

Term	Method	Z=2	Z=10	Z=50	Z=100
2^3S_1	RCI(Coul.)	-2.170032	-60.73404	-1611.201	-7463.047
2^3S	NRHF[a]	-2.17426			
	Exact(NR)[b]	-2.1752294	-60.317488		
	Exp.[c]	-2.1753528			
2^3P_0	RCI(Coul.)	-2.128472	-60.32759	-1608.706	-7453.788
2^3P_1	RCI(Coul.)	-2.128472	-60.32321	-1608.329	-7452.952
2^3P_2	RCI(Coul.)	-2.128471	-60.31487	-1598.051	-7208.648
2^3P	NRHF[a]	-2.13144			
	Exact(NR)[b]	-2.1331641	-60.055676		
2^3P_0	Exp.[c]	-2.1332836			
2^3P_1	Exp.[c]	-2.1332881			
2^3P_2	Exp.[c]	-2.1332884			
$2^3P_{0,1,2}$	Exp.[c]		-60.379		

a) Reference 11.
b) Reference 10.
c) Reference 9.

Table 4. The RCI energies, exponents and the CSF expansion coefficients for some lower excited states in helium-like systems.

Term and CSF[a)]	Z=2	Z=10	Z=50	Z=100
2^3S_1				
Energy	-2.170031	-60.73404	-1611.201	-7463.047
Exponent	1.995	9.910	49.91	99.93
1s2s	0.866162	0.998540	0.999951	0.999985
2p-2p+	0.000002	0.000003	0.000010	0.000020
1s3s	-0.499749	-0.053953	-0.009846	-0.005382
2s3s	-0.001652	-0.002607	-0.000534	-0.000320
2p-3p-	-0.000681	-0.000129	-0.000026	-0.000013
2p+3p-	-0.001925	-0.000365	-0.000067	-0.000026
2p-3p+	0.001925	0.000366	0.000073	0.000036
2p+3p+	0.002152	0.000408	0.000076	0.000028
3p-3p+	0.000001	0.000001	0.000001	0.000002
2^3P_0				
Energy	-2.128472	-60.32759	-1608.706	-7453.788
Exponent	2.001	9.877	49.85	99.85
1s2p-	0.754264	0.997169	0.999911	0.999967
2s2p-	-0.012139	0.002643	0.000852	0.000579
3s2p-	-0.002987	-0.004586	-0.001150	-0.000857
1s3p-	-0.656437	-0.074970	-0.013261	-0.008063
2s3p-	-0.004318	-0.002184	-0.000416	-0.000323
3s3p-	-0.001329	-0.000836	-0.000158	-0.000122

a) p- and p+ mean $p_{1/2}$ and $p_{3/2}$, respectively.

Table 4. Continued.

Term and CSF	Z=2	Z=10	Z=50	Z=100
2^3P_1				
Energy	-2.128472	-60.32321	-1608.329	-7452.952
Exponent	2.003	9.883	49.85	99.85
1s2p-	0.615619	0.827834	0.998619	0.999954
2s2p-	-0.010251	0.001945	0.001121	0.000735
1s2p+	-0.435026	-0.555833	-0.050496	-0.004253
2s2p+	0.007263	-0.001224	0.000332	0.000203
3s2p-	0.002737	-0.001187	-0.000552	-0.000365
3s2p+	0.001605	0.002497	0.000189	0.000075
1s3p-	-0.536541	-0.063139	-0.014379	-0.008550
2s3p-	-0.003240	-0.001786	-0.000323	-0.000272
3s3p-	-0.000959	-0.000689	-0.000122	-0.000102
1s3p+	0.379085	0.041651	-0.000921	-0.000596
2s3p+	0.002297	0.001224	0.000156	0.000087
3s3p+	0.000680	0.000471	0.000060	0.000033
2^3P_2				
Energy	-2.128471	-60.31487	-1598.052	-7208.648
Exponent	2.004	9.886	49.88	99.94
CSF				
1s2p+	0.753620	0.997107	0.999909	0.999967
2s2p+	-0.012758	0.002117	0.000598	0.000137
3s2p+	-0.003439	-0.001337	-0.000345	-0.000112
1s3p+	-0.657165	-0.075933	-0.013491	-0.008071
2s3p+	-0.003807	-0.002152	-0.000373	-0.000184
3s3p+	-0.001102	-0.000832	-0.000138	-0.000065

Polarization Plasma Spectroscopy

Takashi Fujimoto
Department of Engineering Science, Kyoto University, Kyoto

In experimental plasma spectroscopy, little attention has been paid so far to an important attribute of plasma emission radiation, the polarization. When the excitation mechanism of a particular excited level of atoms or ions is spatially anisotropic, these excited ions have a spatial anisotropy, the alignment. Then the emission radiation has a spatially anisotropic intensity distribution and is polarized. Anisotropic excitation is realized by collisional excitation by electrons whose velocity distribution has spatial anisotropy. An example is a shifted maxwellian distribution. When excited ions are produced by the charge exchange process with a directional neutral hydrogen beam, for example, alignment is also produced.

The most usual situation of our experimental arrangement is such that we observe a plasma, which may be anisotropic, from a particular direction with detectors having different sensitivities for different polarization directions of radiation. When we ignore the existence of the alignment in the excited ions or the spatial anisotropy of the radiation, the observed light intensity is different from what is expected from the upper-level population, and we would be lead to an incorrect conclusion. On the contrary, there is a possibility that we may utilize the polarization characteristics of the emission radiation and derive information on the anisotropy of the plasma. We call the latter approach the polarization plasma spectroscopy.

The first example of the phenomena relevant to polarization plasma spectroscopy is the intensity ratio of the Lyman doublet of hydrogenlike ions. For ions for which the relativistic effect can be neglected, the intensity ratio for $1\ ^2S_{1/2} - 2\ ^2P_{1/2}$ to $1\ ^2S_{1/2} - 2\ ^2P_{3/2}$ should be 1/2. There are several observations in which the ratio is substantially larger than 1/2. An example is the hydrogenlike titanium lines observed from JT-60 tokamak. The ratio is about 1.3/2. Another is hydrogenlike iron from a solar flare observed by Hinotori satellite.

A possible interpretation to these intensity anomalies is the

excitation transfer from the metastable $2\ ^2S$ level by proton collisions to the $2\ ^2P_{1/2}$ level. The proton density, however, is too low by two orders of magnitude to explain the intensity anomaly, even for the tokamak plasma. Therefore, other explanations should be sought, and the alignment is one possibility; These plasmas have highly anisotropic distributions of electrons, and alignment is produced in the 2p level resulting in the intensity anomalies.

Until recently, there has been no calculation on the excitation anisotropy of the 2p level by electron collisions. Dr. R. Srivastava has performed a Coulomb-Born calculation for hydrogen-like titanium and iron,[1] and a substantial alignment is found. The question, however, whether the effect of the excitation anisotropy actually explain the observation is still open and should be a subject of future studies.

The produced alignment may be destroyed by isotropic collisions in plasma. We call this phenomenon the disalignment. Disalignment by electron collisions has been studied extensively by, e.g., the Hanle effect experiment. There has been no experimental investigation of disalignment by electron or ion collisions until recently. Alignment is understood as a population imbalance among the magnetic sublevels of an excited level. Disalignment is the equilibration of these populations. The same alignment may be interpreted as the existence of the Zeeman coherence, or of the off-diagonal elements of the density matrix. Disalignment is then understood as relaxation of the phase correlation of the atomic wavefunctions of the sublevels. This latter interpretation suggests that the disalignment is closely related with the phenomenon of Stark broadening of spectral lines. This is because the latter phenomenon is interpreted as relaxation of the optical coherence, or of the phase correlation of the wavefunctions of the upper and lower levels. It is thus expected that the rate coefficient for disalignment by electron collisions is rather close to the corresponding quantity for Stark broadening.

The group of the present author attempted to measure the disalignment rate by using an afterglow plasma and the laser-induced-fluorescence spectroscopy method. Metastable neon atoms in a neon-helium mixture plasma were laser-excited with the polarized light, and the polarized components of the subsequent fluorescence were

observed. From the temporal decay of the polarization degree of the fluorescence light the disalignment rate was determined. Various effects like disalignment by atomic collisions were corrected for. The electron temperature and density were determined spectroscopically. It was found that the resulting rate coefficient is in agreement with the corresponding quantity for Stark broadening within 40 %.[2]

References

1. R. Srivastava (private communication).
2. A. Hirabayashi, Y. Nambu, M. Hasuo and T. Fujimoto, Phys. Rev. A **37**, 83 (1988).

Spectroscopy in Heliotron E

K.Kondo, K.Miyake*, T.Oda**

Plasma Physics Laboratory, Kyoto University, Uji, Japan
*Faculty of Engineering, Kyoto University, Kyoto, Japan
**Faculty of Engineering, Hiroshima University, Higashi-Hiroshima, Japan

Abstract

The status of spectroscopic diagnostics in Heliotron E is described. The spectra from 50 Å to 7000 Å are measured by VUV and visible spectrometers with multichannel detectors. In VUV region, impurity spectra are identified, and useful line pairs are indicated to estimate the density ratio of iron to oxygen applicable to an uncalibrated spectrometer. In visible region, spectral profiles, the Doppler broadening, the Doppler shift and the Zeeman splitting, are analyzed to obtain the ion temperature, the energy components of the injected neutral beams, and the locations of the impurity. The intensity ratio of the charge exchange recombination emission to the Doppler-shifted H_α emission of the injected neutral beam is useful to estimate the impurity to electron density ratio.

§1. Introduction

Plasma spectroscopy is one of the significant diagnostics for understanding plasmas. In Heliotron E, various spectroscopic measurements have been applied to the currentless plasma, produced by high power gyrotrons and further heated by NBI and ICRF. Heliotron E is a nonaxisymmetric torus with helical coil. The major radius is 2.2 m and the averaged minor radius is 0.2 m, respectively. The size of the magnetic surface, the rotational transform and the shear parameter are varied by applying the additional toroidal field and the auxiliary vertical field on the helical field [1]. The range of the plasma parameters is $0.94 \leqslant B(T) \leqslant 1.9$, $0.1 \leqslant n_e(10^{13}\ cm^{-3}) \leqslant 20$, $T_e(keV) \leqslant 1$, $T_i(keV) \leqslant 0.8$, $P_{NBI}(MW) \leqslant 2.5$, $P_{ECH}(MW) \leqslant 0.6$, $2.14 \leqslant R(m) \leqslant 2.24$, $0.18 \leqslant \bar{a}(m) \leqslant 0.23$. The recent experimental results are shown in elsewhere [2]. The important plasma parameters, such as ion temperature, poloidal rotation velocity and electron density near the ablating pellet, are already estimated [3].

In this report, the impurity spectra obtained by a multichannel VUV spectrometer are analyzed. The useful line pairs for estimating the impurity density ratio by an uncalibrated spectrometer is shown. In the visible region, spectral profiles due to the Doppler broadening, shift and the Zeeman splitting are investigated to provide the plasma parameters: ion temperature, energy components of the neutral beam, and the locations of atoms and low ionized ions. Finally the method to estimate the impurity and electron density ratio by using the intensity ratio of the charge exchange recombination and the Doppler shifted H_α emissions of the injected neutral beams is shown.

§2. VUV SPECTROSCOPY

2-1. Instrument

A flat-field VUV survey spectrometer is used to analyze impurity spectra between 50 Å to 400 Å. Figure 1 shows the schematic drawing of the instrument. The main components are the entrance slit (10 μm width), the grating with unequal groove spacing (Hitachi,001-0437) and 1024-channel detector (Hamamatsu Photonics,F1208-21PX,S2304-1024FH). The dispersion is 0.11 Å /ch at 50 Å and 0.23 Å/ch at 400 Å. The wavelength resolution is about 1 Å. The minimum integration time is 10 ms. The AD converter is 10 bits in full scale. The data are stored and analyzed by a personal computer (NEC PC9801-VX4) [4].

The absolute wavelength is calibrated by helium gas puffing and Ne-seeded pellet injection. Figure 2 shows the three successive spectra when Ne-seeded pellet was injected into a neutral beam heated plasma. The integrated time was 10 ms and the pellet was injected during the frame 6. The observed neon lines are Ne VIII (88.1, 98.2, 103.1 Å) and Ne VII (106.1 Å). The obtained dispersion has a good agreement to the calculated one. Upper traces are time behaviors of the electron density and Ne VIII resonance line (770 Å) observed by a single channel VUV monochromator (McPherson 247V).

Absolute sensitivity is inevitable to discuss the impurity density quantitatively. But this instrument has not been calibrated yet. No suitable line pairs for branching ratio was available unless additional injection of the interest elements. Only at the limited wavelengths, the relative sensitivity is measured using the doublets from Na-like iron and nickel (Fe XVI 335.4 Å, 360.8 Å, Ni XVIII 291.9 Å, 320.6 Å). The relative sensitivity at these wavelengths is nearly same.

2-2. Spectra

Figure 3 shows the time behavior of impurity spectrum between 50 Å and 400 Å, which was observed in the plasma heated by neutral beams with 2.2 MW. The integrated time was 10 ms. The average electron density increased to 6 x 10^{13} cm^{-3} and the central electron temperature was 450 eV. The wall of the vacuum chamber is stainless steel and titanium was flashed for gettering. The prominent line emissions are described in figure 4. The highest ionization stages of these impurity lines are Fe XVIII, Ni XVIII, Cr XVI, Ti XVIII, Cl XV, O VIII, and C VI.

Figure 5 shows the spectra observed before and after the carbonization. Applying the carbonization on the wall of the vacuum chamber, metallic impurity lines except titanium disappeared.

Figure 6 shows the titanium spectrum, when titanium dropped into the plasma accidently. Nineteen shots of titanium drop were found in 562 shots. The observed titanium lines were Ti XI (386.14 Å), Ti X (360.13, 289.58 Å), Ti IX (296.28, 278.71, 267.94 Å), Ti VIII (263.56, 258.61 Å), Ti VII (264.82, 254.69 Å), Ti VI (255.38, 251.07 Å).

Figure 7 shows the time behavior of the spectra, when pellet is injected into a beam heated plasma. The low ionized impurity emissions had been less affected and intensities of multiply ionized impurity emission increase, which indicates that the change of the electron density near the edge is small and at the central region large, and also impurities accumulate to the center of the plasma column.

2-3. Line Ratios of Fe IX (171 Å) and O VI (173 Å)

The main impurities are oxygen and iron in the beam heated plasma. It is important to estimate the density ratio of iron to oxygen, and

fraction contributing to Z_{eff}. Since this instrument has not been calibrated in whole spectral region, the line pairs of Fe IX (171 Å) and O VI (173 Å) were used to measure the density ratio of iron to oxygen. The wavelength difference is only 2 Å. The relative sensitivity seemed to be same at these wavelengths. The ionization potentials are 240 eV and 134 eV, respectively, and the difference is not so large. The intensity of these two lines are described as $I \propto n_e\ n_{imp}\ Q(Te)$, where n_e, n_{imp}, and $Q(T_e)$ are electron and impurity densities, and excitation rates. If these impurities locate where their ionization potentials are equal to the electron temperature, the electron density and temperature dependent-Q are easily estimated. The density ratio of Fe IX and O VI is about 1/50 ~ 1/100. The iron fraction contributing to Z_{eff} is about 2 ~ 5 % of oxygen.

§3. VISIBLE SPECTROSCOPY

3-1. Instrument

It is necessary to analyze spectral profiles due to the Doppler broadening, shift and the Zeeman splitting for measuring plasma parameters. A 1.26 m visible spectrometer (SPEX 1269) with a 512-channel detector (Tracor Northern, TN6133) is employed. The dispersion of this system is 0.1 Å/ch, and the minimum integration time is 5 ms. The plasma emission is guided to the entrance slit of the spectrometer through a lens and fiber optics. The spatial scanning is made by using the mirror in the vacuum chamber. The sightline intersects the neutral beam, which is injected perpendicularly into the plasma. An angle between the sightline and the beam varied from 63 to 76 degrees. Figure 8 shows the geometry of the neutral beam line and

sightlines in the vacuum chamber. The magnetic flux surfaces are also shown.

3-2. The Doppler Broadening

The Doppler broadening of the charge exchange recombination lines, C VI(3435 Å), and O VIII(2981 Å), is measured by using heating neutral beams. Lines, C V(2271 Å), O V(2781 Å), and C III(2977 Å) are also used to measure edge ion temperature.

3-3. The Doppler Shift

Two kinds of the Doppler-shift are measured. The first is the plasma poloidal rotation to estimate electric field [3]. The second is H_α emissions from the high energy neutral beams to measure the energy components [5] and beam attenuation profiles [6]. The beam injection energy is varied from 20 to 30 kV. Figure 9 shows the spectral profiles of the H_α emissions observed by two different sightlines, (-03) and (0), which intersect the neutral beam line. There are three peaks near the unshifted H_α emission. They are the Doppler shifted H_α emissions of the beam neutrals excited mainly by electron collision. The wavelength shifts correspond to the beam energy E(23.5 kV), E/2 and E/3, which are originated from the acceleration of H^+, H_2^+, and H_3^+ ions. The fraction of the energy components are estimated easily.

If the electron density profile is known, the attenuation profile of the injected neutral beam is also estimated [6]. Figure 10 shows the beam density profile, where the electron density was assumed to be a parabolic profile.

3-4. The Zeeman Splitting

It is important to know the locations of the impurity and neutral emissions. Usually the passive spectrocopy tells no space-resolved emission intensity along the sightline. If the Zeeman splitting is observed and the spatial variation of the magnetic field strength is given, the location of the emission will be identified [7]. Figure 11 shows time behaviors of the specral profiles of Cr I(4274 Å), H_α(6563 Å) and C II(6578, 6583 Å), where the Zeeman splitting is clearly observed. Figure 12 shows the levels and their corresponding emission lines of Cr I (4274 Å) in the magnetic field of 2 T. There are three groups of emission lines, two of which are σ-components and the other is π-components. Intensity of the σ-components is proportional to $(1+\cos^2\theta)$, and π-components to $\sin^2\theta$, where θ is an angle between the sightline and the magnetic field line. If θ is small enough, only σ-components are observed, and the magnetic field strength at the emission is calculated from the splitting width. Figure 13 shows the magnetic field strength and the angle θ along the sightline. Figure 14 shows the Zeeman splitting of Cr I (4274 Å) at the various sightlines. The magnetic field strength of about 2.3 T was derived from the splitting width. A and B are two locations, where B = 2.3 T, in the each sightline as shown in figure 15. At B, the electron density is larger than 10^{12} cm^{-3}, and the ionization length of chromium is less than 1 cm. The most probable location of neutral chromium is considered at A near the wall.

Figure 16 shows the time behavior of H_α Zeeman profile in ECH plasma. Figure 17 shows the Zeeman splitting width and corresponding magnetic field strength. At the first and decaying phase, H_α emissions locate at the magnetic field of 2 T, and during ECH pulse at B = 2.4 T. There are

two possibilities for B = 2 T, A and C as shown in figure 18. The measurement by a thermal Li beam probe showed that the plasma radius is smaller at the first and the decaying phase than during the ECH pulse [8]. The emission region moved from C to B, and to C.

3-5. Line Ratio of the Charge Exchange Recombination Emission and the Doppler-shifted H_α Emission

The density ratio of the fully ionized oxygen and carbon to electron density can be estimated by the intensity ratio of the charge exchange recombination emission to the Dopper-shifted H_α emission of the beam neutrals. The intensity of the charge exchange recombination is described as

$$I_{imp}^{cx} = G\,R(\lambda_1) \sum_{k=1}^{3} n_b(E/k)\, n_{imp} \langle \sigma_{cx}(E/k)\, V_b(E/k) \rangle$$

and the Doppler-shfted H_α emission is

$$I_{H_\alpha}^{Dop} = G\,R(\lambda_2) \sum_{k=1}^{3} n_b(E/k)\, n_e \langle \sigma_{ex}\, v_e \rangle$$

where G is geometrical factor and $R(\lambda)$ are sensitivity at the wavelengths, and σ_{cx} and σ_{ex} are cross sections for charge exchange recombination and electron excitation and n_b is beam density.
The intensity ratio of these emissions can be related density ratio of the impurity (fully ionized oxygen or carbon) to electron density.

$$\frac{I_{imp}^{cx}}{I_{H_\alpha}^{Dop}} = \frac{R(\lambda_1)}{R(\lambda_2)} \frac{n_{imp}}{n_e} \frac{\sum_{k=1}^{3} \{ f(E/k) \langle \sigma_{cx}(E/k)\, V_b(E/k) \rangle \}}{\langle \sigma_{ex}\, V_e \rangle \sum_{k=1}^{3} f(E/k)}$$

where f(E/k) is fraction of the beam energy components normalized to the primary beam energy, E.

This method is powerful because the beam density profile is not necessaly and only the relative intensity ratio provides the impurity and the electron density ratio.

Acknowledgements

The authors would like to acknowledge the effort of the Heliotron E Group.

References

[1] T.Obiki et al., Fusion Technology 17 (1990) 101

[2] K.Kondo et al., 17th EPS Conf. on Controlled Fusion and Plasma Heating, Amsterdam,(1990), Vol.II p459

[3] K.Kondo et al., Rev.Sci.Instrum. 59 (1988) 1533

[4] K.Kondo et al., Jpn.J.Appl.Phys. 27 (1988) 1287

[5] K.Kondo et al., PPLK-R-29,Plasma Physics Lab.Kyoto Univ.(1988)

[6] K.Kondo et al., 7th Int.Stellarator Workshop, Oak Ridge, USA.(1989)

[7] P.G.Carolan et al., JET-P(85)05

[8] A.Komori, private communication

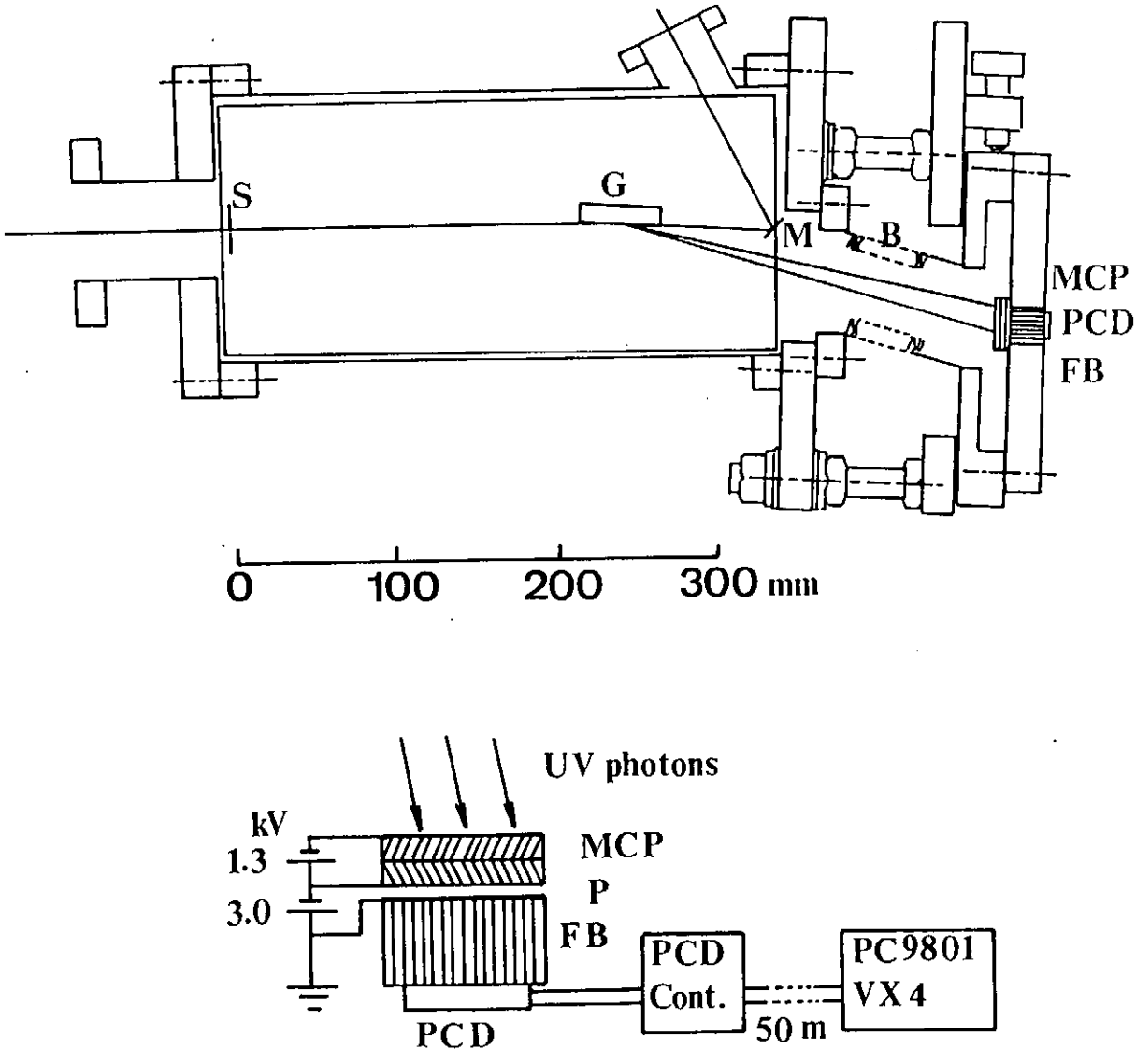

Figure 1. Schematic of the multichannel VUV spectrometer and detector. S: entrance slit, G: unequal spacing grating, M: mirror for zeroth light rejection, B: bellews, MCP:micro-channel plate, FB: fiber bundle, PCD: plasma coupled device.

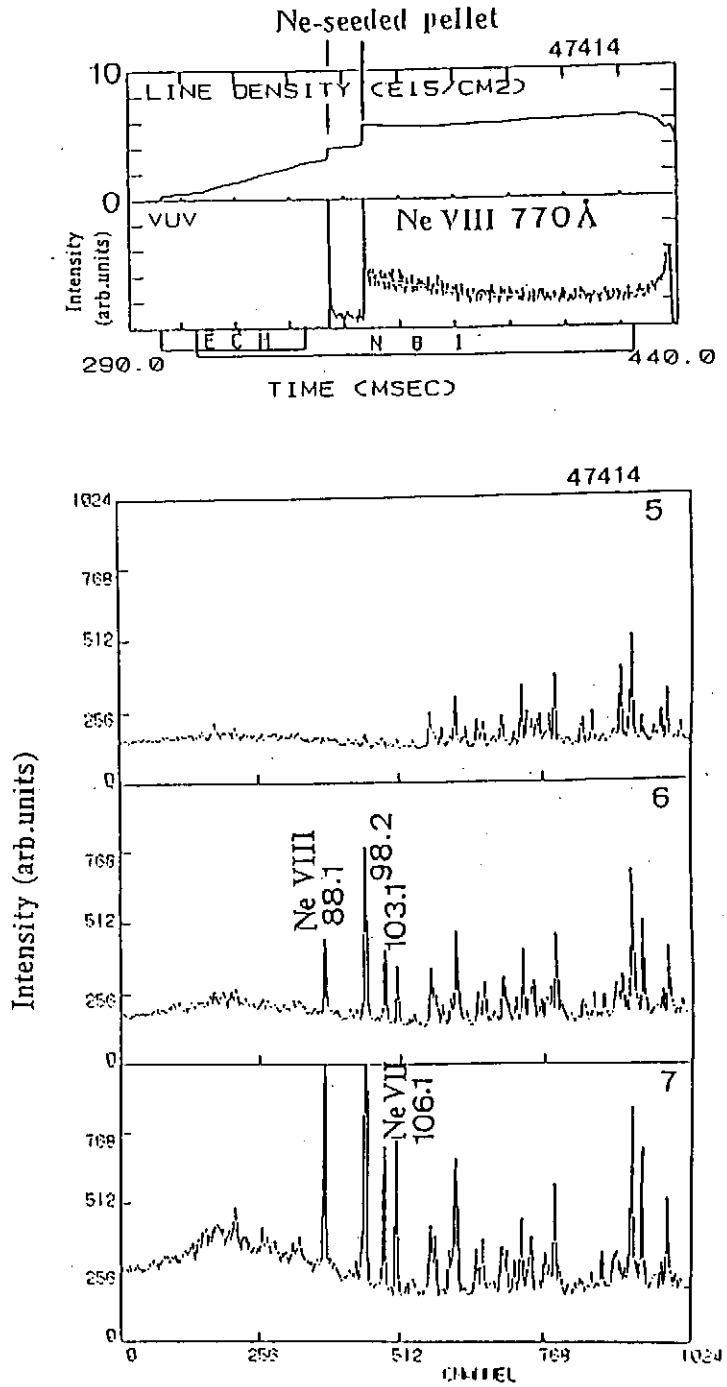

Figure 2. Spectra of Ne VIII(88.1, 98.2, 103.1 Å) and Ne VII(106.1 Å) when Ne-seeded pellet was injeced into a beam heated plasma. Upper traces are the time behaviors of the electron density and Ne VIII (770 Å) resonance line.

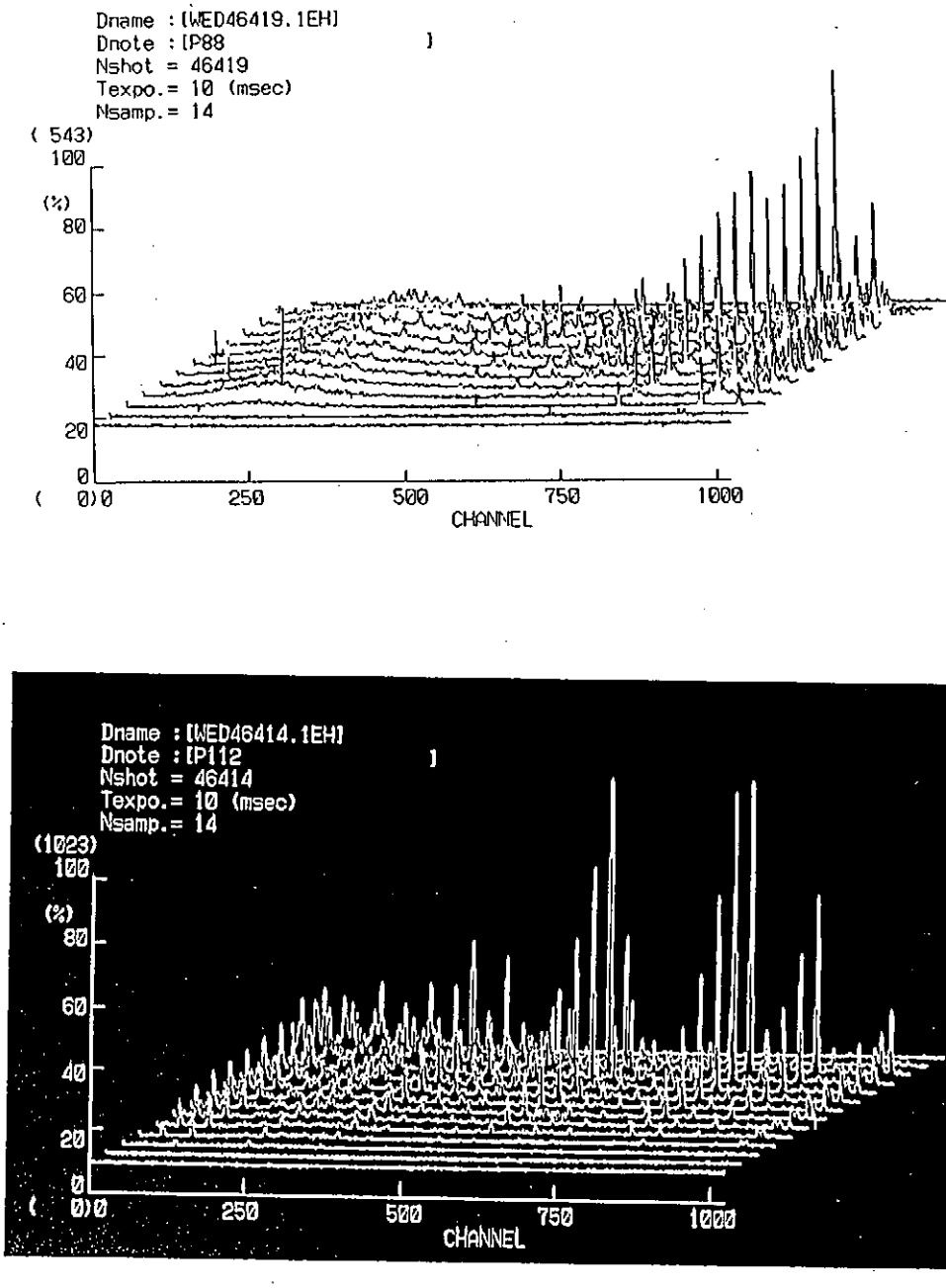

Figure 3. Time resolved VUV spectrum in the beam heated plasma in the wavelength from 45 Å to 400 Å. The time resolution is 10 ms.

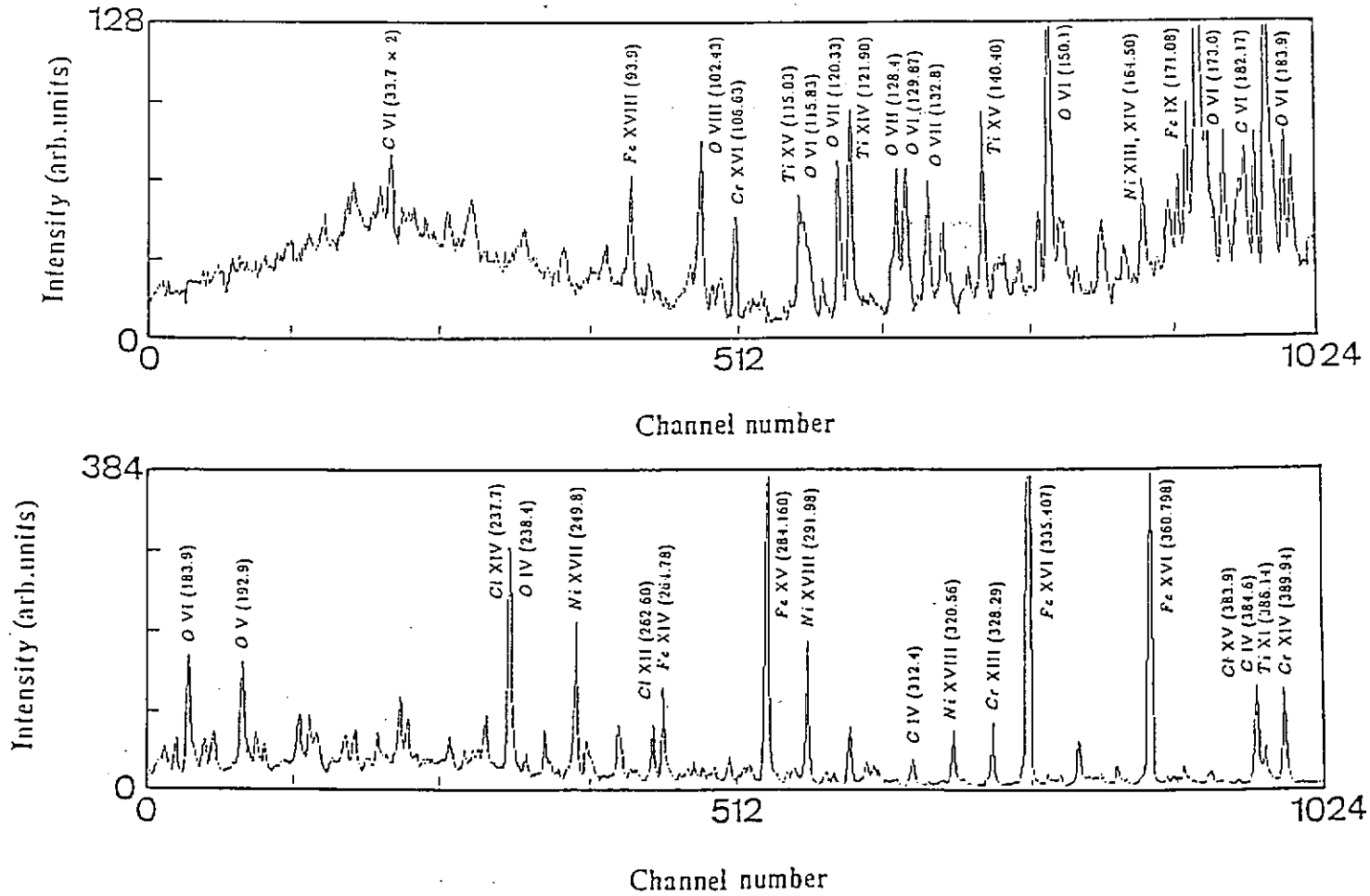

Figure 4. Spectrum of Heliotron E plasma impurities in the beam heated plasma.

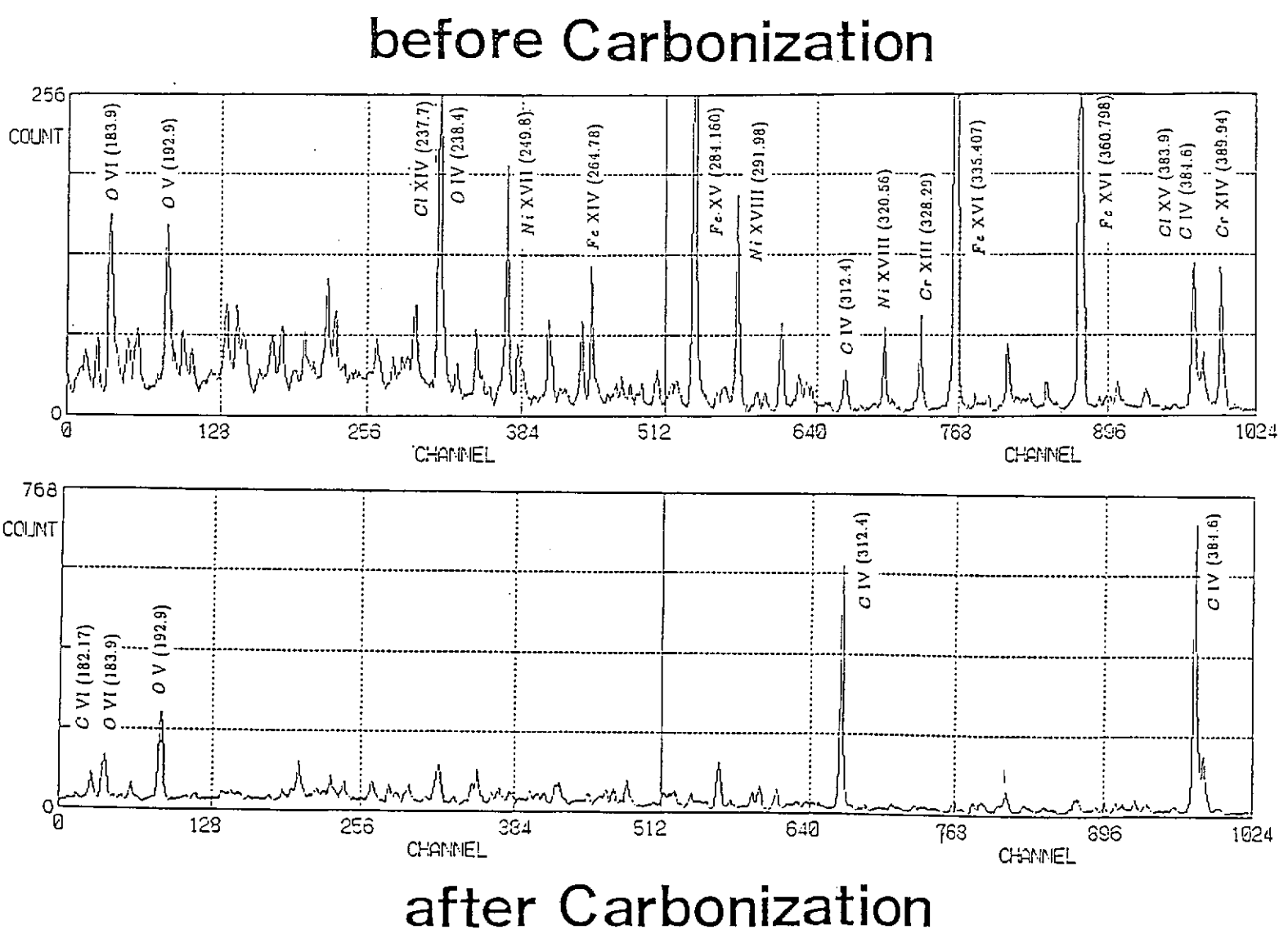

Figure 5. Spectra before and after carbonization.

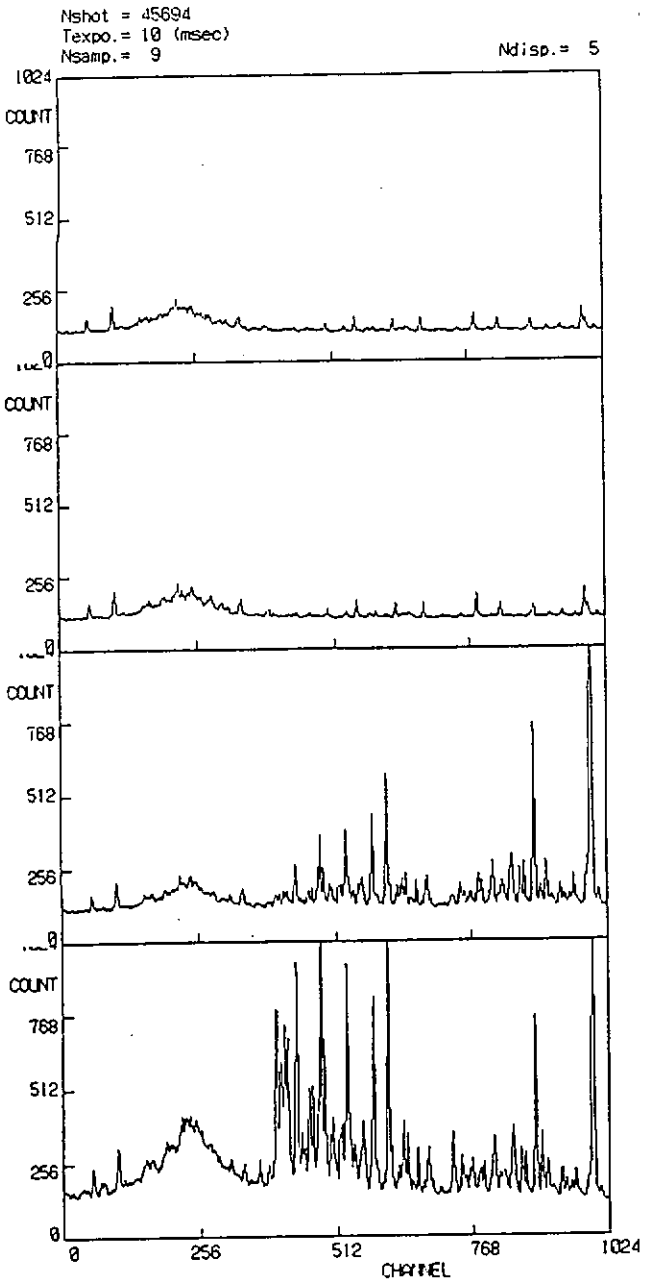

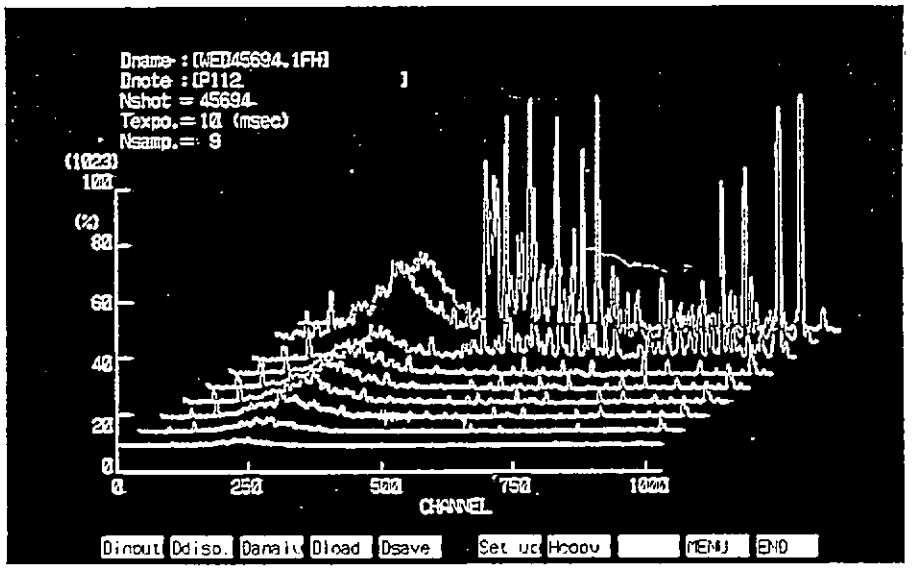

Figure 6. Titanium spectrum when titanium dropped into a plasma.

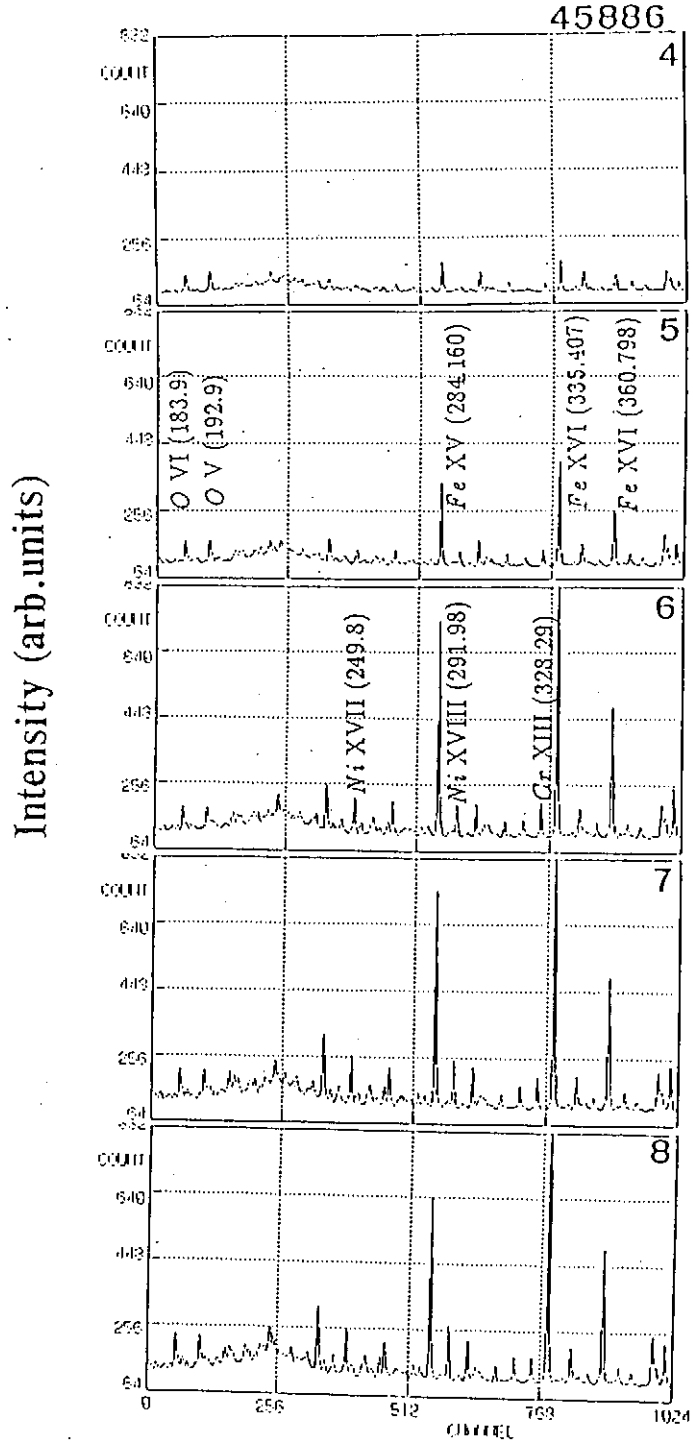

Figure 7. Time resolved spectrum of pellet injected plasma. Two plellets were injected during frames 5 and 6.

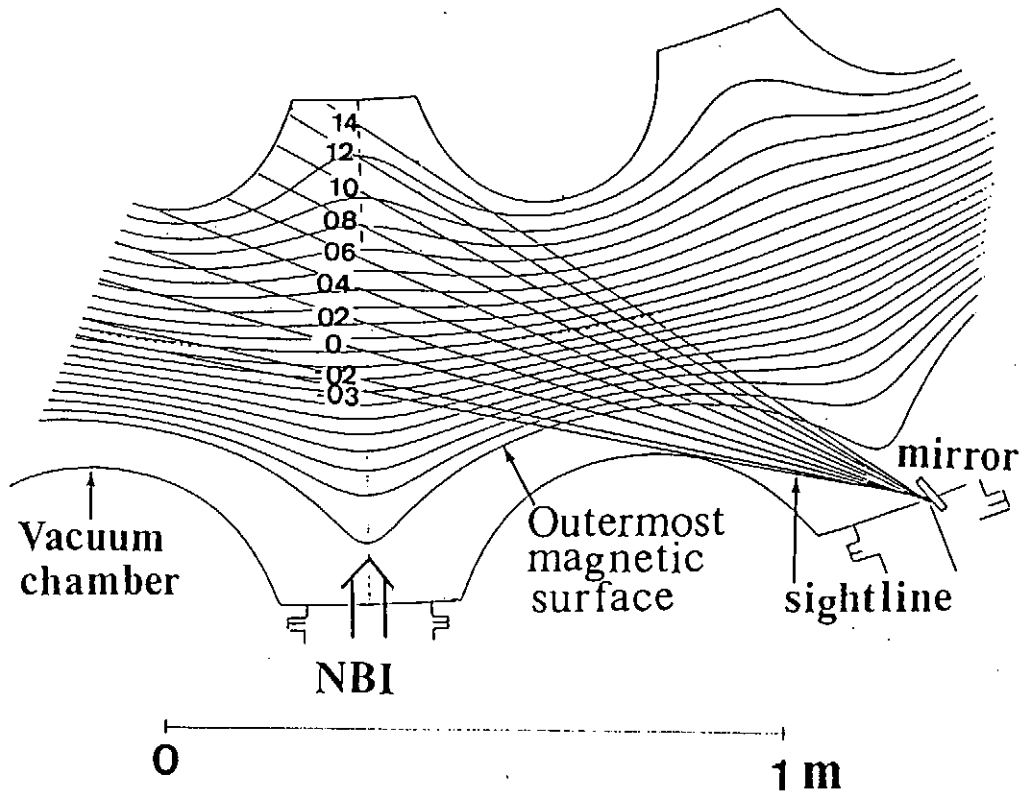

Figure 8. Top view of the sightlines of visible spectroscopy.

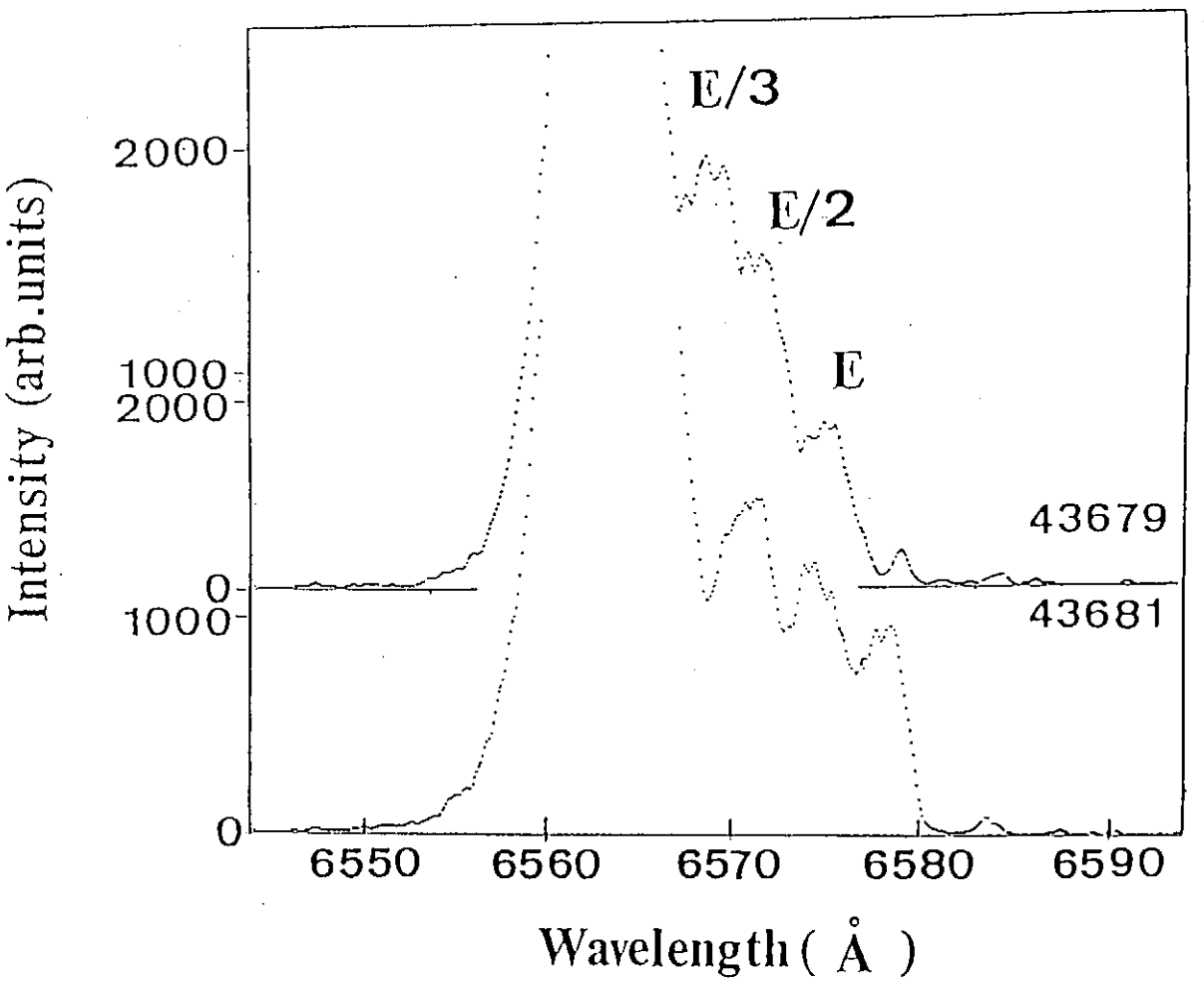

Figure 9. The spectral profiles of the Doppler shifted H_α emissions. Sightlines are (-03) and (0). E,E/2 and E/3 indicate the beam energy components from H^+, H_2^+ and H_3^+ ions.

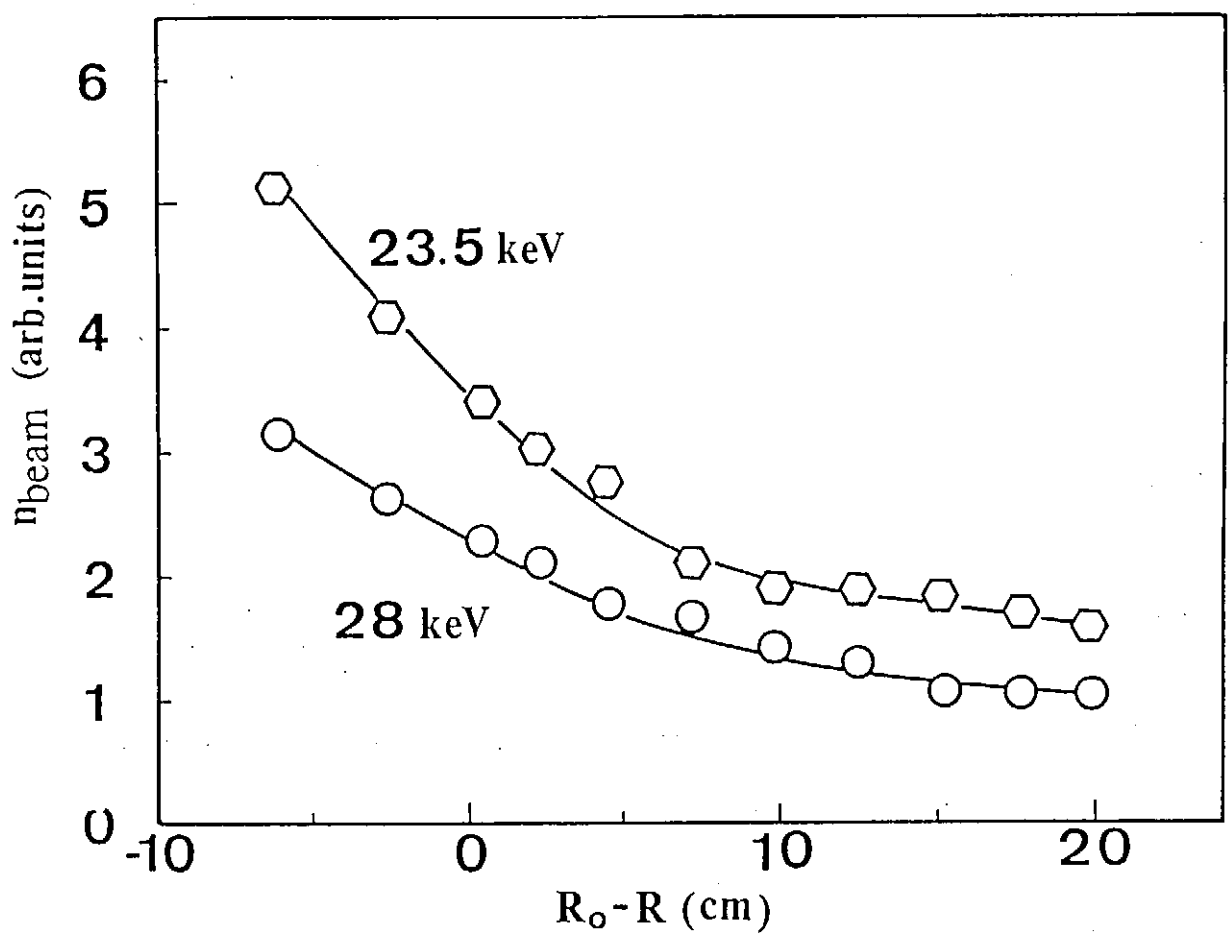

Figure 10. The neutral beam density profile measured by the Doppler-shifted H_α emissions.

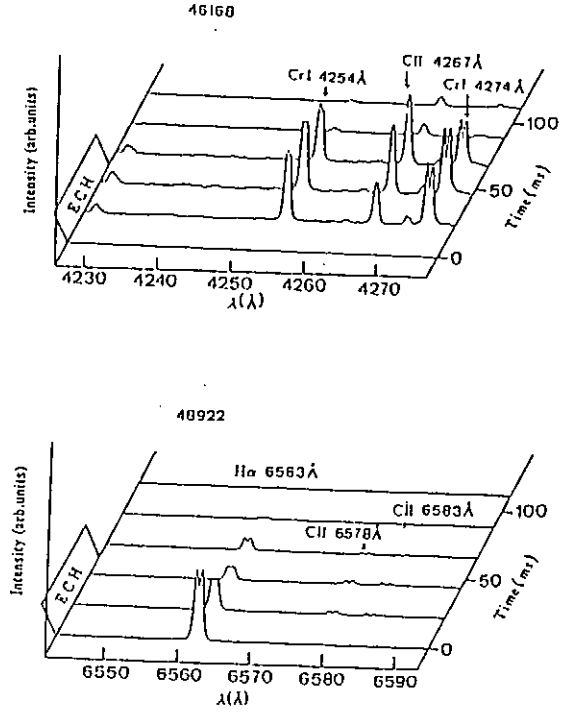

Figure 11. Time behavior of the Zeeman splitting of Cr I(4274 Å), H_α , and C II(6578, 6583 Å).

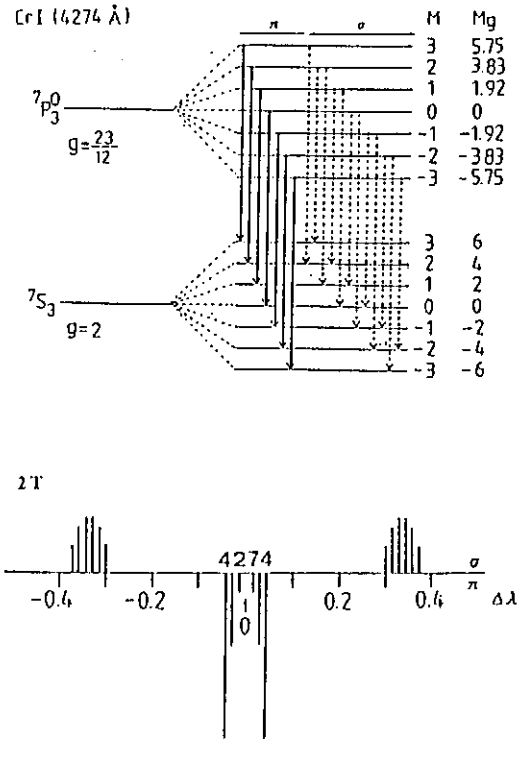

Figure 12. Level diagram and wavelengths of Cr I at B = 2 T.

$\alpha^*(B_t/B_h) = 0$

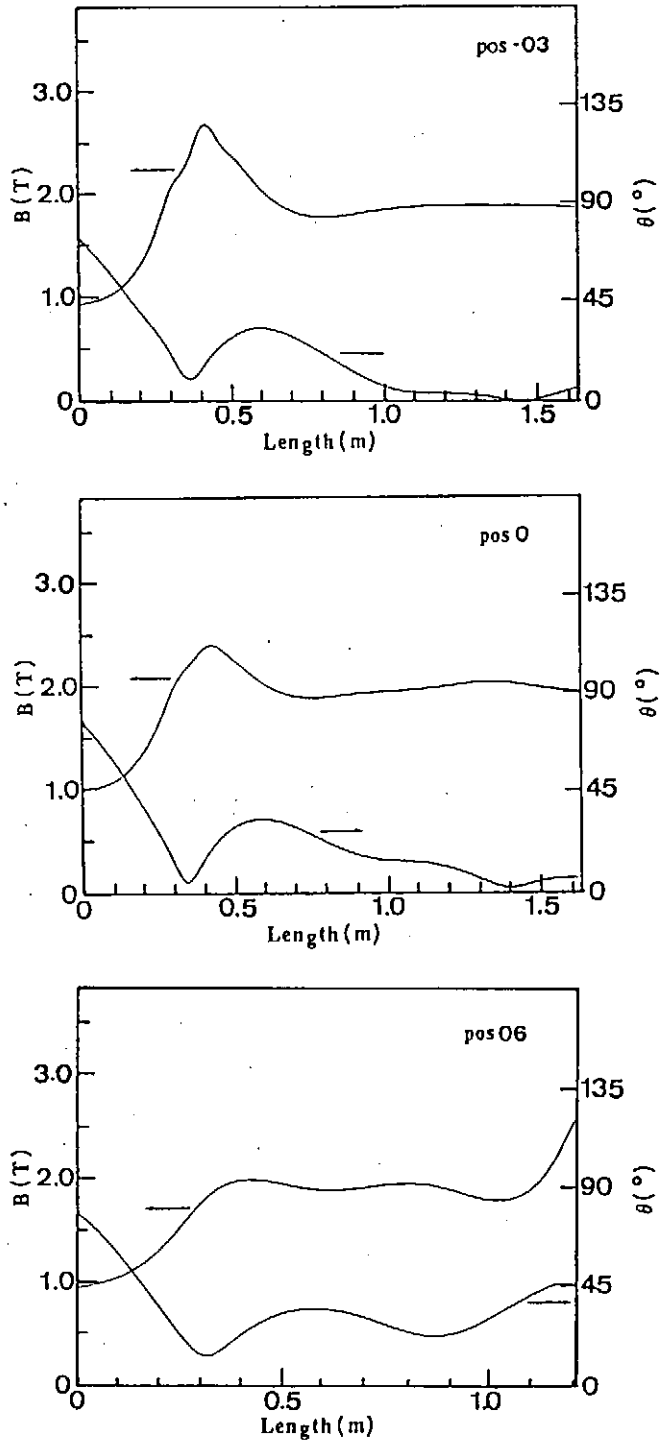

Figure 13. Magnetic field strength and an angle between the sightline and the magnetic field line. The length is measured from the mirror in the vacuum chamber.

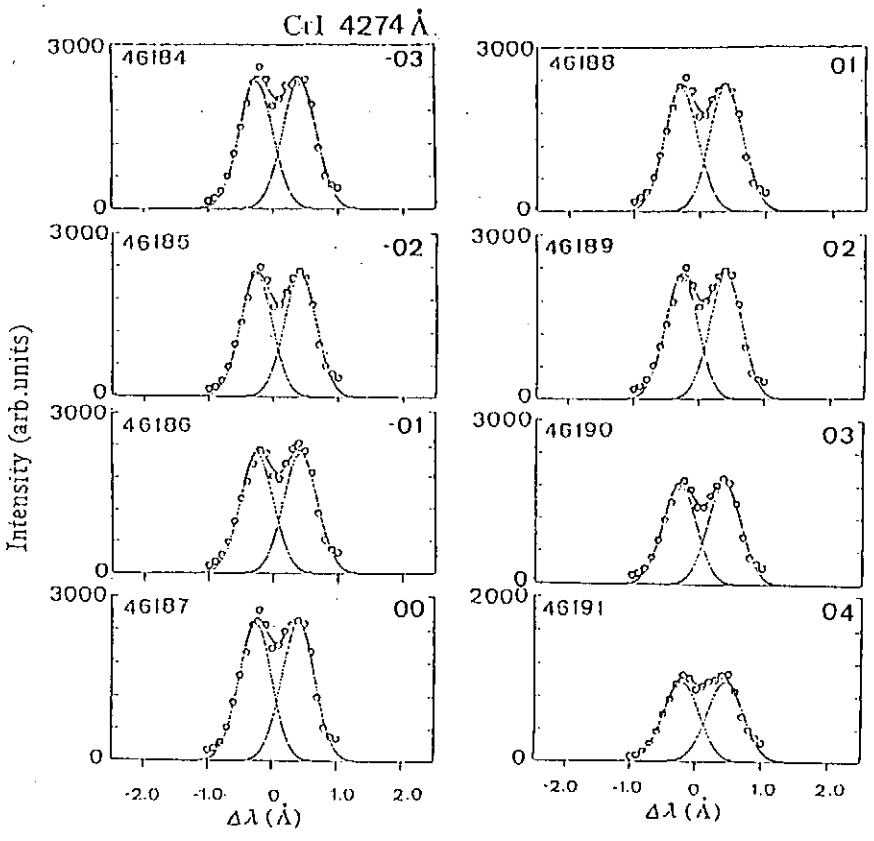

Figure 14. Cr I Zeeman splitting at various sightlines.

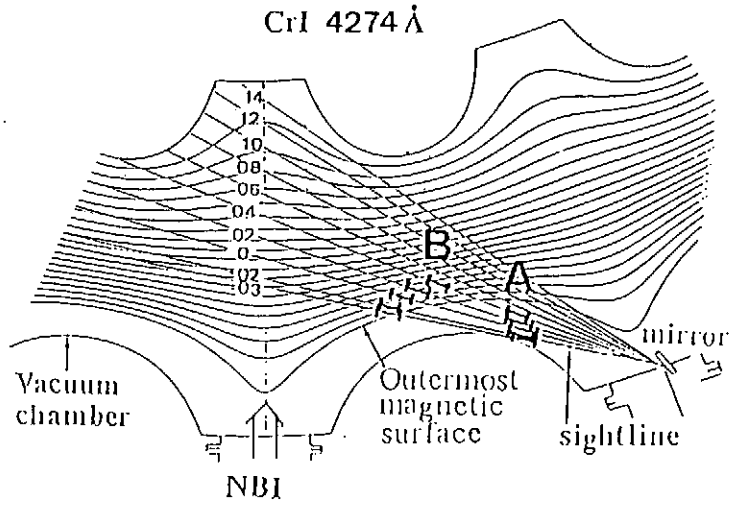

Figure 15. Locations A and B, where the magnetic field strength correspond to the observed Zeeman splitting. Neutral chromium locates at A.

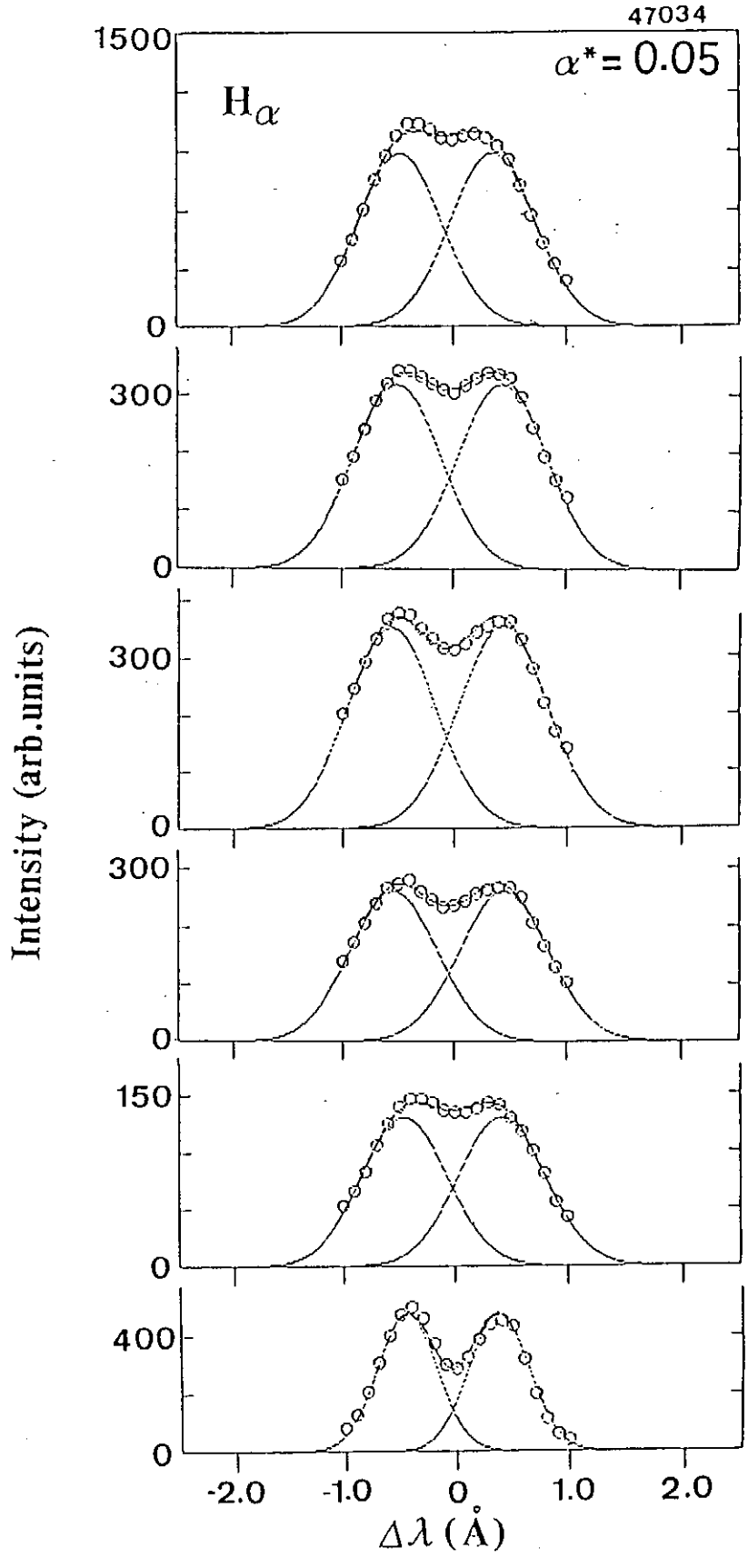

Figure 16. Time behavior of the H_α Zeeman splitting.

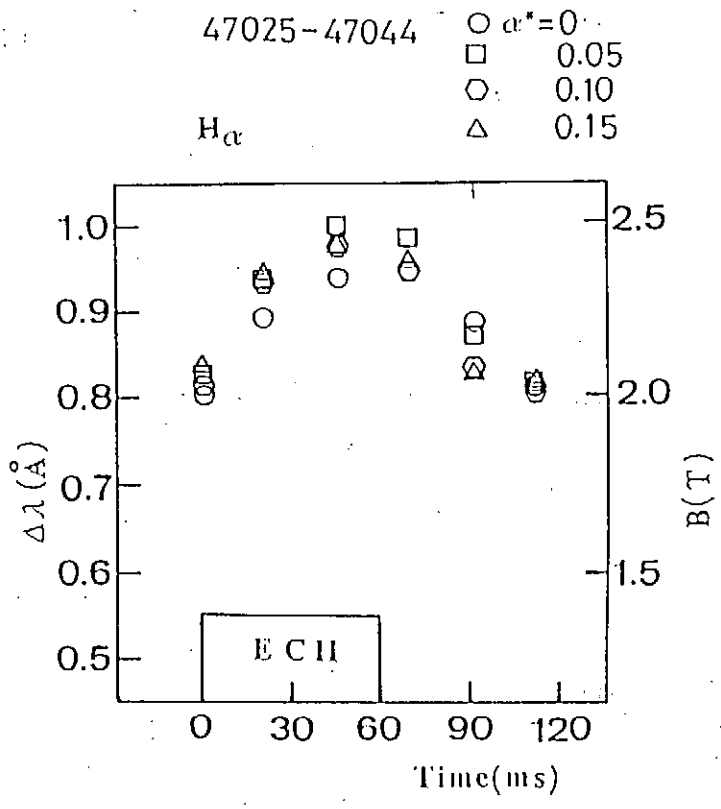

Figure 17. Width and magnetic field strength of the H_α Zeeman splitting.

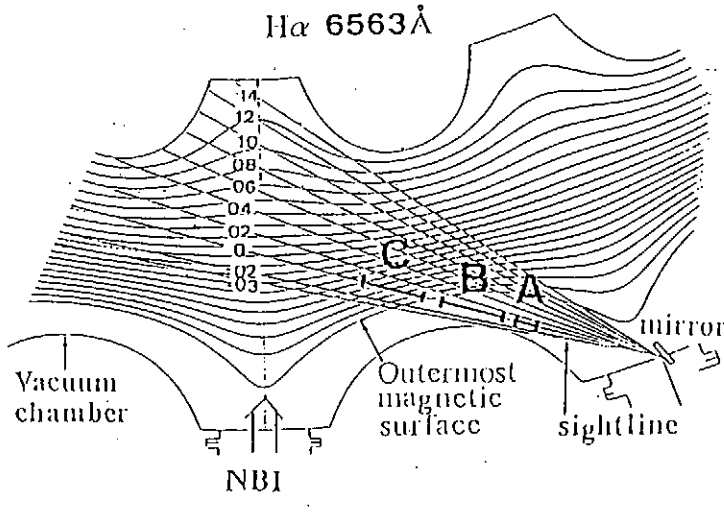

Figure 18. Locations of H_α emission. At the first and decaying phase, H_α emission locates at C, and during ECH pulse at B.

Measurement of electric filed from plasma rotation using CVI lines

Part I

Edge Electric Field Profiles of H-mode Plasmas in JFT-2M Tokamak

K.Ida and S.Hidekuma
National Institute for Fusion Science
Nagoya, 464-01, Japan

Y.Miura, T.Fujita, M.Mori, K.Hoshino, N.Suzuki,
T.Yamauchi and JFT-2M Group
Japan Atomic Energy Research Institute
Naka-machi, Naka-gun, Ibaraki, 319-11, Japan

A structure of an edge radial electric field E_r inferred from poloidal rotation velocity is compared with that of particle/thermal transport barrier for H-mode plasmas in JFT-2M. Both of E_r and its gradient $\partial E_r/\partial r$ in the thermal transport barrier are found to become more negative at the L/H transition. On the other hand, $\partial E_r/\partial r$ is more positive in the region of the particle transport barrier. The shear of radial electric field and poloidal rotation velocity in H-mode is localized within an ion poloidal gyro radius near the separatrix, in the region of ion collisionality $\nu_{*i} \approx 20\text{-}40$.

PACS number 52.55.Fa, 52.55.Pi, 52.70.Kz

Since the H-mode plasma was discovered in ASDEX,[1] it has been observed in many tokamaks.[2-5] Several theoretical models on the transition of L-mode to H-mode plasmas have been presented[6-11]. Recently a radial electric field (E_r) near the plasma periphery has been found both experimentally and theoretically to play an important role in the L/H transition.[12-19] A more negative radial electric field was observed a few ms before the L/H transition in D-IIID[12] and a decrease in particle transport was observed with negative E_r, by driving a radial current, in CCT[13]. Theoretical models associated with the radial electric field have been proposed to explain the L/H transition[14-17]. However, the predicted change of the gradient of the radial electric field ($\partial E_r/\partial r$) is different between models. In Shaing's model[16], the poloidal flow velocity changes at the L/H transition and the corresponding radial electric filed E_r becomes more negative and $\partial E_r/\partial r$ becomes more positive and hence suppresses the fluctuations. On the other hand, Itoh's model[17] predicts positive values of $\partial E_r/\partial r$ in L-mode and negative values of $\partial E_r/\partial r$ in H-mode and that this negative $\partial E_r/\partial r$ reduces the banana width of ions and the electron anomalous flux by the improved micro-stability. Thus it is crucial to measure the gradient or profile of the radial electric field for L- and H-mode plasmas in tokamaks. In this paper we present the radial electric field and temperature gradient profile a few cm inside the separatrix where the transport barrier is produced in H-mode plasmas in JFT-2M[5].

The radial electric field profiles are inferred from poloidal/toroidal rotation and ion pressure profiles using the ion momentum balance equation;

$$E_r = \frac{\partial p_i}{e n_i \partial r} - (B_\theta V_\varphi - B_\varphi V_\theta),$$

where p_i, n_i are the ion pressure and density, B_φ and B_θ are the toroidal and poloidal magnetic fields, and v_φ and v_θ are the toroidal and poloidal rotation velocities. The toroidal rotation velocity, ion temperature and fully stripped carbon density profiles are measured using multi-channel charge exchange spectroscopy technique[18,19] at CVI 5292Å with toroidal arrays (two sets of 34 channels) with a spatial resolution of 1 cm. The poloidal rotation and edge ion temperature profiles are measured using the intrinsic radiation of CVI at 5292Å with poloidal arrays (two set of 23 channels), which do not view across the beam line and view only the plasma periphery with a spatial resolution of 4 mm. In order to avoid the integration problem of line-of-sight, an wavelength-resolved Abel inversion[18] is used to obtain local ion temperature and poloidal rotation velocity from poloidal arrays.
These two set of toroidal/poloidal arrays view the plasma in opposite directions to define the zero reference for Doppler shift measurements.

The electron temperature profile and its gradient profile are meaured with an ECE radiometer to investigate the location of the thermal transport barrier. The electron temperature is obtained from the intensity of ECE with some correction associated with optical thickness and reflection coefficient at the wall. The spatial resolution of the measurements set by the frequency bandwidth of the detector is 3 mm. Bulk electron density (n_e) and temperature (T_e) are measured with Thomson scattering and the edge n_e and T_e profiles are measured with a electric probe from 5 mm inside to 30 mm outside of the separatrix. The uncertainty of the position of the separatrix calculated with an equilibrium code is estimated to be 5 mm.

Figure 1 shows the time evolution of the poloidal rotation velocity for a plasma with a current of 250 kA, a toroidal field of 1.24 T, q_ψ of 2.8 in a single null divertor configuration. The neutral beam is injected at 700 ms in the co-

direction with a power of 0.7 MW. A jump of poloidal rotation velocity at the L/H transition is observed at 0.4 cm inside the separatrix, while the significant increase of ion temperature is observed at ds=-1.3 cm, more inside the plasma. The poloidal rotation increases in the electron diamagnetic direction in the H-mode regardless of the direction of plasma current and neutral beam injection. The change of poloidal rotation is prior to the change of ion temperature and is fairly localized near the separatrix, while the sharp gradient of ion temperature is also observed more inside. In H-mode with ELM, no poloidal rotation velocity shear is observed, however, some steep gradient of ion temperature is observed. The strong shear of poloidal rotation velocity is observed in the region of $|a-r| < \rho_p \approx 1.3$ cm. The profiles of ion/electron temperature, density and poloidal/toroidal rotation velocity are measured in detail before (t = 710 ms) and after (t= 740 ms) the L/H transition to derive radial electric field profiles as shown in Figs.2 and Fig.3(a).

As shown in Fig.3(b), the electric field profiles for L-mode and H-mode plasmas are calculated from rotation velocities of carbon and ion pressure gradients assuming that momentum exchange between impurities and ions is large enough to make impurities rotate in the same speed of bulk ions. This is a good assumption, since no difference of rotation velocity between He^{2+} and O^{8+} has been observed[20]. Here, ion density profiles is estimated with electron density profiles and carbon density profiles[19] which is a dominant impurity in JFT-2M. The electric field profiles calculated with C^{5+} momentum balance equation, where the momentum exchange between bulk ions and C^{5+} is neglected, are shown with dashed lines in Fig.3(b) as a references. The electric field becomes more negative in H-mode, due to increase of poloidal rotation in the electron diamagnetic direction and the increase of the ion pressure gradient. The gradient of the electric field inside the separatrix, ds = -0.7 cm, becomes more negative, -50 ± 10 V/cm^2, in the H-mode. The

ion/electron thermal transport barrier is found at 1-2 cm inside the separatrix. On the other hand, the particle transport barrier demonstrated with gradient of electron density and the brightness of CVI emission is much narrower and within 0.5 cm of the separatrix as shown in Figs.4. The absolute values of the gradient of electron density measured with electric probes have uncertainty by factor of two, however, the relative values is accurate enough to measure the location of particle barrier. The brightness of CVI emission is roughly proportional to the product of electron density and C^{5+} density, since the excitation rate in visible region has week temperature dependence. We note that the particle transport barrier and the thermal transport barrier are produced in the different region of the plasma. These measurements (Figs.3 and 4) seem to indicate that the improvement of thermal transport correlates to the negative $\partial E_r/\partial r$ and the improvement of particle transport correlates to the positive $\partial E_r/\partial r$. However these measurements do not exclude the possibility that the more negative electric field itself, not the gradient, is important in the L/H transition.

It is important to compare the measured plasma parameters such as poloidal rotation, electric field, and pressure gradient with K.C.Shaing's and Itoh's models. The poloidal rotation parameter $U_{p,m}$ [$=v_\theta B/v_\varphi B_\theta+\lambda_p/2$, $\lambda_p=\rho_p(\partial p_i/\partial r)/p_i$] changes from 2.1 ± 0.4 to 3.4 ± 0.2 at L/H transition 0.9 cm inside the separatrix. This change of poloidal rotation at L/H transition agrees with the prediction of K.C.Shaing's model[16] within a factor of two or three. The ion collisionality ν_{*i} at 0.7 cm inside the separatrix decreases from 44 ± 7 (L-mode) to 22 ± 10 (H-mode). The measured rotation parameter and critical ν_{*i} values do not agree with the critical value of ν_{*i} (≈ 1.5) and $U_{p,m}$ before L/H transition (≈ 0.7) in their model. The large value of critical ν_{*i} measured in JFT-2M may be explained with Sahing's model by including the additional effect of fast ion loss[21]. It also is interesting to evaluate the strength of the

gradient of radial electric field $\partial E_r/\partial r$, since it can affect the ion orbit and change the banana width of ions by the factor of $(|1-u_g|+C\varepsilon)^{-1/2}$, where ε and C are an inverse aspect ratio and a numerical coefficient.[15,22] The shear parameter of electric field u_g, defined by $\rho_p(\partial E_r/\partial r)/v_{thB\theta}$, is 0.4 ± 0.3 for L-mode and -1.0 ± 0.2 for H-mode at 0.7 cm inside the separatrix. The gradient of electric field measured in H-mode is large enough to change the banana width. This shear parameter u_g is 1.0 in L-mode and -2.3 in H-mode in Itoh's model[17]. The pressure gradient parameter λ $[=-(T_e/T_i)\rho_p\{(\partial n_e/\partial r)/n_e+\alpha(\partial T_e/\partial r)/T_e)\}]$ defined in his model changes from 0.5 to 1.3, at L/H transition and is consistent with the critical value of their model ($\lambda_c \approx 1$). We observe qualitative agreement of characteristic parameters in the L/H transition with Itoh's model and K.C.Shaing's model. However both models are point model and do not fully explain the structure of edge electric field, negative $\partial E_r/\partial r$ in thermal transport barrier and positive $\partial E_r/\partial r$ more outside. In conclusion, both of E_r and $\partial E_r/\partial r$ become more negative in the thermal barrier in L/H transition. Positive $\partial E_r/\partial r$ and particle transport barrier are observed more outside of this thermal barrier both for L- and H-mode plasma.

We would like to thank S.-I.Itoh, K.Itoh and K.Toi (NIFS) and K.C.Shaing (ORNL) for their useful discussions. Comments by T.Leonard(GA) is acknowledged. We also thank the support of data acquisition by T.Matsuda (JAERI) and M.Kojima (NIFS). Continuous encouragement by H.Maeda (JAERI), Y.Hamada(NIFS), K.Matsuoka (NIFS) are acknowledged.

References

[1]F.Wagner et al., Phys. Rev. Lett. **49**, 1408 (1982).
[2]S.M.Kaye et al., J. Nucl. Mater **121**, 115 (1984).
[3]M.Nagami et al., Nucl. Fusion **24**, 183 (1984).
[4]A.Tanga, et al., Nucl. Fusion **27**, 1877 (1987).
[5]S.Sengoku et al., Phys. Rev. Lett. **59**, 450 (1987).
[6]T.Ohkawa et al., Phys. Rev. Lett. **51**, 2101 (1983).

[7]F.L.Hinton Nucl. Fusion **25**, 1457 (1985).
[8]H.P.Furth, Plasma Phys. Controlled Fusion **28**, 1305 (1986).
[9]N.Ohyabu et al., Nucl. Fusion **26**, 593 (1986).
[10]C.M.Bishop, Nucl. Fusion **26**, 1063 (1986).
[11]T.S.Hahm and P.H.Diamond, Phys. Fluids **30**, 133 (1987).
[12]K.H.Burrell et al., Plasma Physics and Contr. Nucl. Fusion **31** 1649 (1989).
[13]R.J.Taylor, et al., Phys. Rev. Lett. **63**, 2365 (1989).
[14]S.-I.Itoh and K.Itoh , Phys. Rev. Lett. **60**, 2276 (1988).
[15]S.-I.Itoh and K.Itoh Nucl. Fusion **29**, 1031 (1989).
[16]K.C.Shaing and E.C.Crume,Jr, Phys. Rev. Lett. **63**, 2369 (1989).
[17]S.-I.Itoh and K.Itoh, Research Report of National Institute for Fusion Science NIFS-4 (1990).
[18]K.Ida and S.Hidekuma, Rev. Sci. Instrum. **60**, 867 (1989).
[19]K.Ida T.Amano, K.Kawahata, O.Kaneko, H.Tawara, Nucl. Fusion **30**, 665 (1990).
[20]K.H.Burrell, R.J.Groebner, H.St.John, R.P.Seraydarian, Nucl. Fusion **28** 3 (1988).
[21]private communication with K.C.Sahing.
[22]F.L.Hinton "ion-electron energy transfer near the separatrix in diverted tokamaks", paper presented at Sherwood Theory Meeting, Oak Ridge, TN, (1987).

Figure captions

Fig.1 Time evolution of (a) poloidal rotation velocity and (b) ion temperature at 0.4 cm (open circles) and 1.3 cm (closed circles) inside the separatrix. The L/H transition occurs at t = 725 ms.

Fig.2 Radial profiles of (a) electron temperature measured with ECE radiometer (circles) and electric probes (squares), (b) ion temperature measured with toroidal (circles) and poloidal (squares) arrays and (c) electron density measured with Thomson scattering (circles) and electric probes (squares), for L-mode (t=710 ms, open symbols) and H-mode (t=740 ms, closed symbols) plasma, where r/a is a normalized minor radius.

Fig.3 Radial profile of (a) Poloidal (circles) and toroidal (squares) rotation velocity and (b) radial electric field, as a function of the distance from the separatrix, for L-mode (t=710 ms, open symbols) and H-mode (t=740 ms, closed symbols). A ds is negative for inside and positive outside of the separatrix. Dashed lines in figure (b) are radial electric field calculated from momentum balance of C^{5+} impurity.

Fig.4 Gradients of (a) electron temperature measured with ECE radiometer (circles) and electric probes (squares) and ion temperature (cross for t=740 ms, triangles for t=760 ms) and (b) electron density measured with Thomson scattering (circles) and electric probes (squares) and the brightness of CVI emission (triangles), as a function of the distance from the separatrix for L-mode (t=710 ms, open symbols) and H-mode (t=740 ms, closed symbols) plasma.

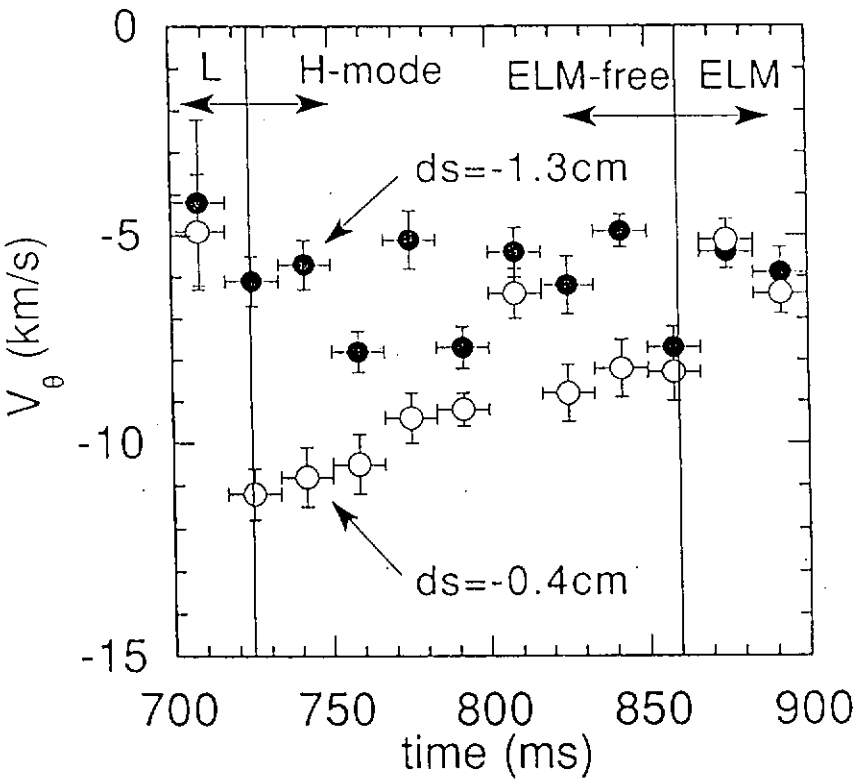

Figure 1 (a) K.Ida et al.

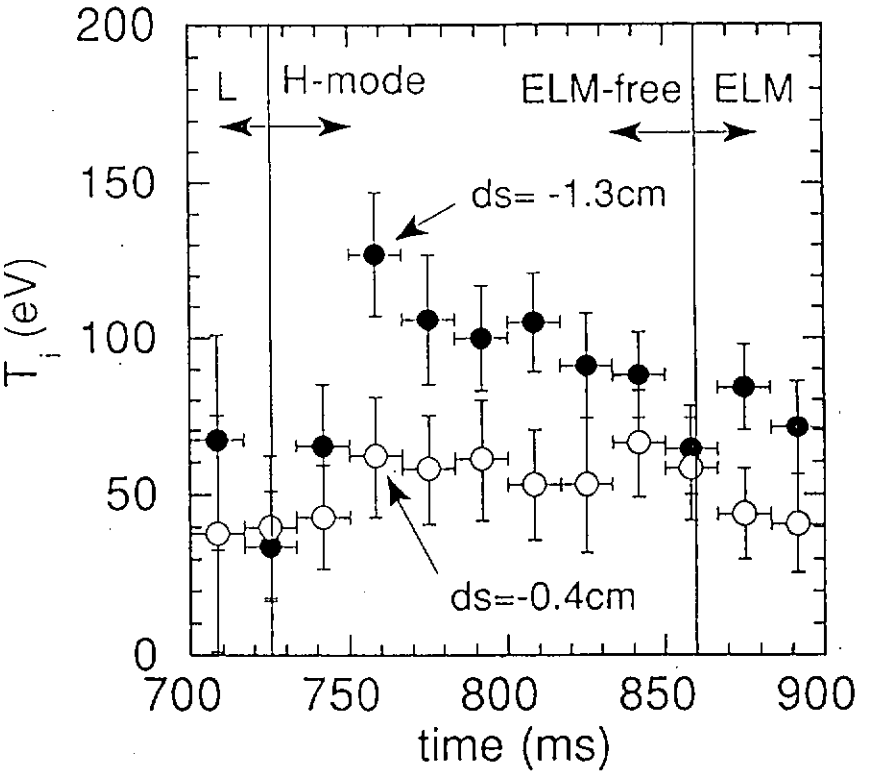

Figure 1 (b) K.Ida et al.

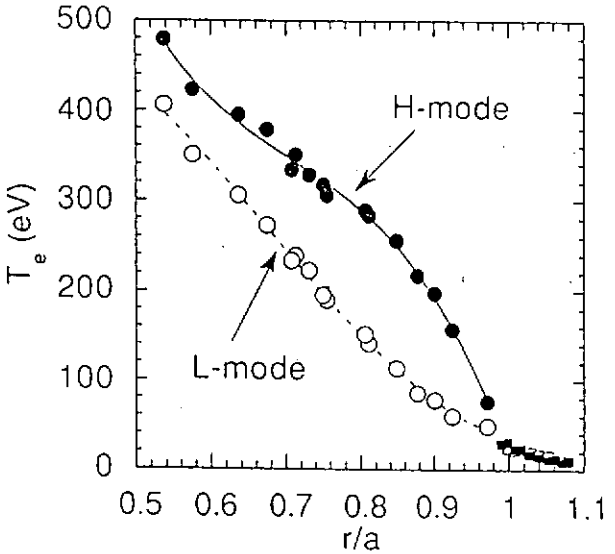

Figure 2 (a) K.Ida et al.

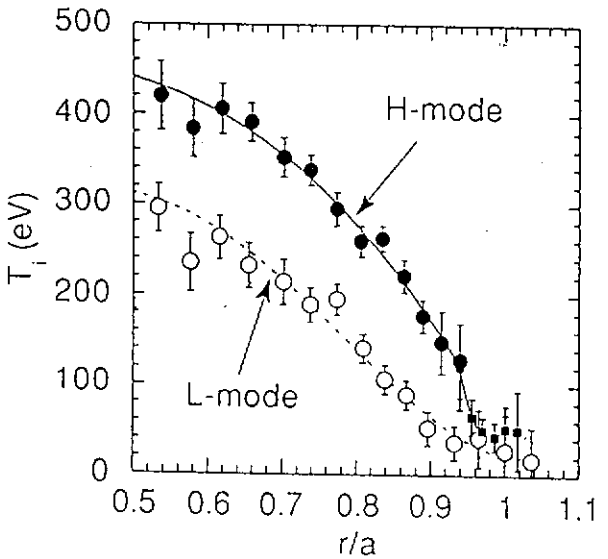

Figure 2 (b) K.Ida et al.

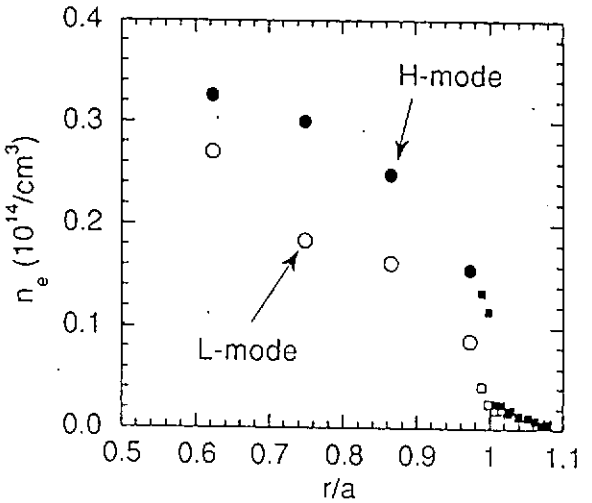

Figure 2 (c) K.Ida et al.

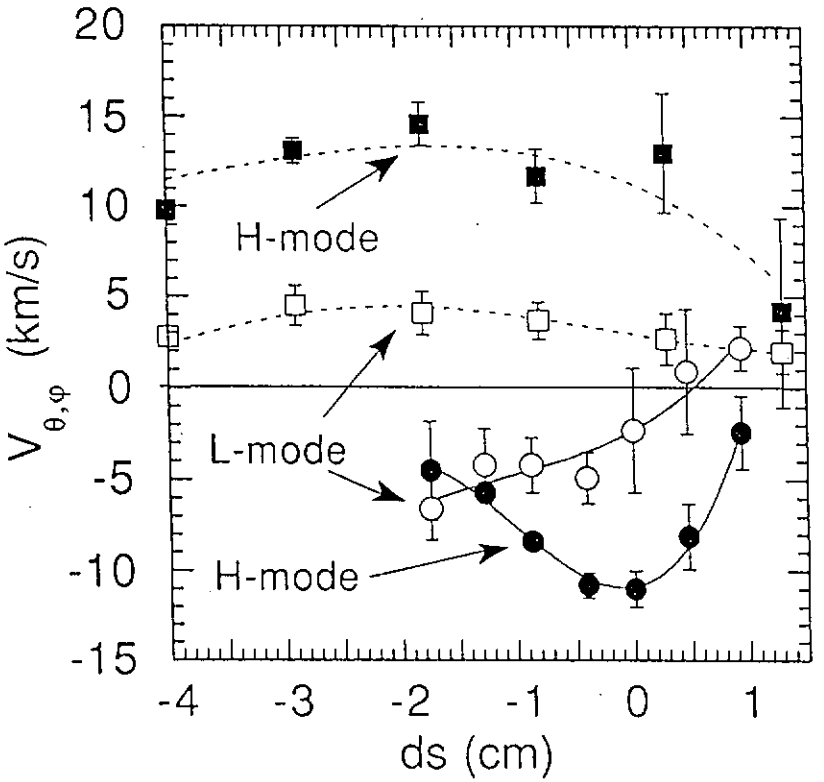

Figure 3 (a) K.Ida et al.

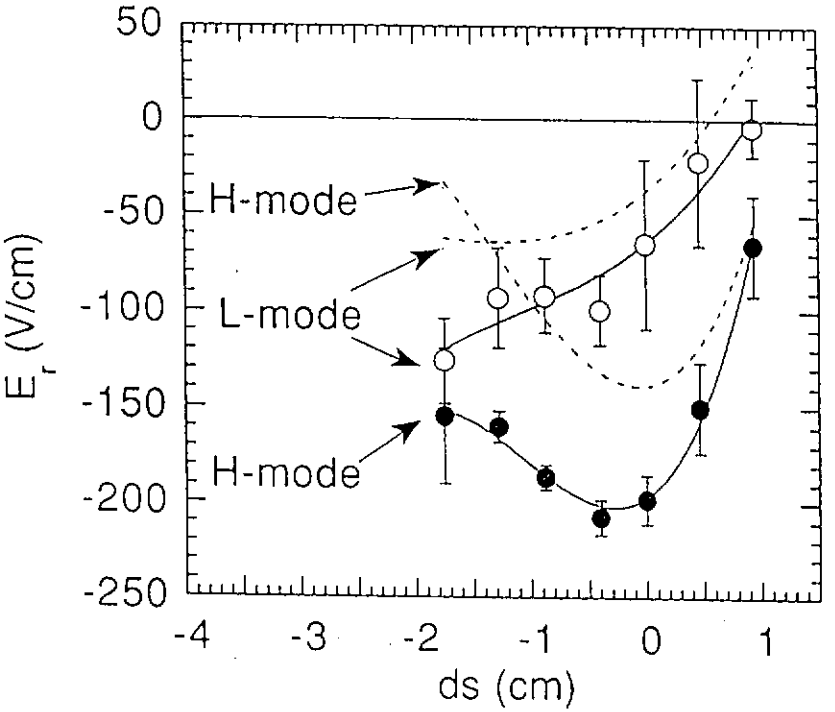

Figure 3 (b) K.Ida et al.

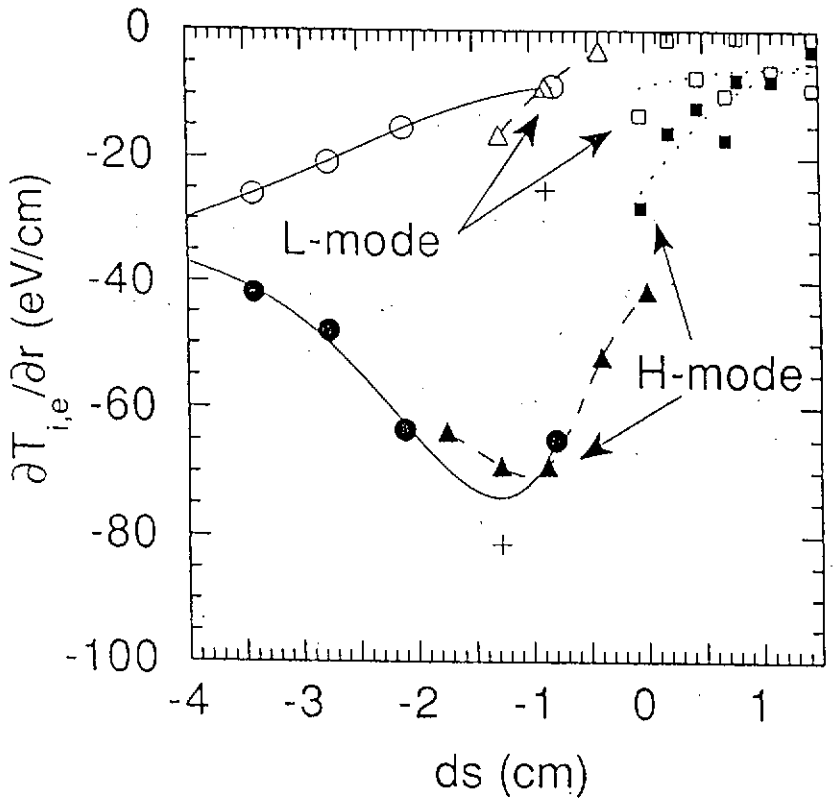

Figure 4 (a) K.Ida et al.

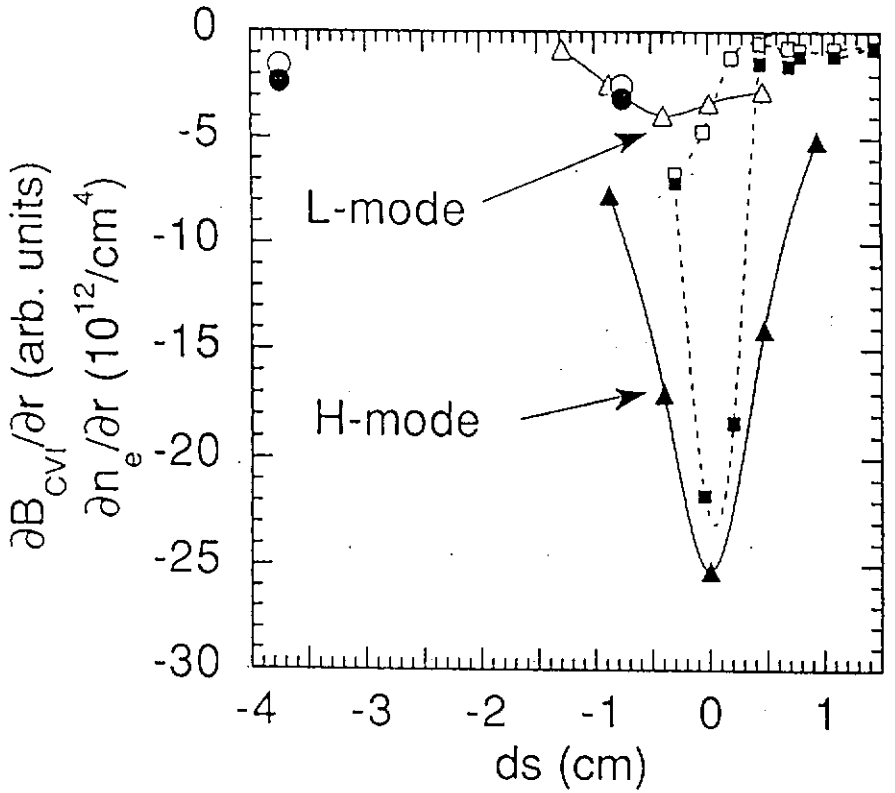

Figure 4 (b) K.Ida et al.

Part II

Electric field profile of NBI heated plasma in CHS

K.Ida, S.Hidekuma, H.Iguchi, H.Yamada, H.Sanuki
and CHS Group
National Institute for Fusion Science,
Nagoya,464-01, JAPAN

Abstract

Ion temperature and poloidal rotation velocity profiles are measured with 68 channel space resolved spectrometer using beam emission spectroscopy technique in CHS. The electric field profiles derived from poloidal rotation velocity has a large shear near the plasma edge and the absolute value of this edge electric field increases from -70 V/cm to -110 V/cm as the ion collisionality ν_{*i} is increased from 2 to 20. The values of radial electric field measured in CHS is larger than the neoclassical estimates especially near the plasma periphery at $r/a > 0.7$.

Ion temperature and electric field profiles are the crucial plasma parameter in helical device, since the electric field is expected to reduce helical ripple loss and improve energy confinement by Neoclassical theory[1-3]. The electric field can be measured with heavy ion beam probe[4] or inferred from poloidal and toroidal rotation velocity using momentum balance equation. The poloidal rotation has been measured with CV line radiation in Heliotron-E device[5]. The measurements are limited only at the plasma edge, since the electron temperature in the core plasma is high enough to ionize C^{4+} to higher ionized stages. No measurement for poloidal rotation velocity near the plasma center has been done in helical devices. In most of tokamak plasmas beam emission spectroscopy techniques have been used to measure ion temperature and toroidal rotation velocity even in the region where carbon or oxygen impurities are fully stripped, however they have not been well established in a helical device due to its complexity of magnetic configuration. In these techniques, the ion temperature, rotation velocity and fully stripped impurity density are measured respectively from the Doppler width, shift and amplitude of the radiation for the high n level transition (visible region) of hydrogen-like impurities excited by the charge transfer between fully stripped impurities and the heating neutral beam[7,8].

Compact Helical System (CHS)[6], which is an l = 2 heliotron/torsatron type device with the major radius of 100 cm and the averaged minor radius of 20 cm. A 28 GHz gyrotoron with the injection power of 100 kW produces ECH plasma with low density below 1×10^{13} cm^{-3} , while tangential NBI can sustain the plasma with high density up to 1×10^{14} cm^{-3}. A 68 channel space resolved 1 m visible spectrometer system using CCD detector coupled with image intensifier has been developed to measure spectrum in poloidal cross section. Two set of 34 channel optical fiber arrays, one viewing a fast neutral beam and the other viewing off the neutral beamline to subtract background radiation, have been installed in CHS. These optical

fibers with 100 μ mm diameter are led into the entrance slit of 1 m Czerny-Turner spectrometer with 2400 grooves/mm grating. At the exit plane the light from each fiber gives the spectrum from one spatial position. The light from all of the fibers is focused onto an image intensifier tube coupled with CCD TV camera. The resolution of the wavelength is 0.1 Å/ch (100 spectral channels) , while its time resolution is only 16.7 ms.

The background radiation is mostly due to the reaction between fully ionized impurity and background thermal neutral in the plasma periphery. This background emitted from the cool plasma edge is proportional to the neutral density at the plasma edge and depends on the clearance between plasma edge and inner wall (the position of magnetic axis) and the amount of gas puff. The background is too high to derive ion temperature profile for the plasma with the magnetic axis of < 92 cm even without gas puff. The most measurements have been done using CVI 5292Å (n = 8-7) for low or medium density plasma with a weak or medium gas puff.

For ECH plasma the beam emission spectroscopy techniques can not be used due to the lack of neutral beam. The intrinsic line radiations emitted from the plasma edge are measured to derive poloidal rotation velocity . Even though the measurements of poloidal rotation cover whole plasma (84 cm < R < 107 cm) the measured velocities represent the component of poloidal rotation velocity to the line of sight and the emission is localized at r=0.7a. Plasma rotates in ion diamag direction with the velocity of 3 km/s for the low density (n_e = 4 x 10^{12} cm^{-3}) plasma produced by ECH. The radial electric field averaged along the magnetic surface is 16V/cm (positive). The central electron temperature is 900 eV. This indicates that the plasma potential is positive in the collisionless regime of ν_{*e} = 0.2.

On the other hand, the beam emission spectroscopy techniques can be used for the NBI plasma. The emission is more localized at the cross section of neutral beam line (midplane)

and line of sight. The measured velocity is more likely poloidal rotation velocity at each point, although the space resolution becomes poor near the plasma center due to the integration effect along the neutral beam. The plasma heated by NBI rotates in the electron diamag direction and has strong shear near the plasma periphery. The poloidal rotation velocity at the plasma edge depends on the collisionality of the plasma.

Radial electric field profiles are obtained from the profiles of ion pressure gradient and toroidal/poloidal rotation with the use of momentum balance equation. The toroidal rotation velocity at $r > 0.7a$ ($\varepsilon_h > \varepsilon_t$) is damped to be almost zero by the viscosity due to helical ripple and has very narrow profile at the center. In order to investigate the dependence of collisionality two discharges, one is low electron density and the other is high density, are compared. The electron temperature and density profiles are measured with Thomson scattering, while ion temperature profiles are measured with CXS as shown in Figs.1. The ion collisionality of ν_{*i} is 2 for low density discharge and 20 for high density discharge. The poloidal rotation profile for these discharges has a strong shear near the plasma edge as shown in Fig. 2(a). The poloidal rotation velocity profiles of these discharges show the significant differences near the plasma periphery. The radial electric field in CHS has a strong electric field shear at the plasma periphery as shown in Fig.2(b). This edge electric field increases as the electron density is increased. This negative electric field is -70 V/cm for low density and -110 V/cm for high density plasma.

It is interesting to compare the radial electric field profiles measured in CHS to neoclassical estimates, since the electric field in heliotoron/torsatoron devices is expected to improve confinement by reducing helical ripple loss. Figure 3 shows the comparison of electric field profiles measured in CHS to the calculated electric field profiles with neoclassical theory presented by Kovrizhnykh[1] and Hastings[2]. These calculated

electric field profiles are smaller than those measured from poloidal rotations. The electric field calculated with Kovrizhnykh formula gives smaller values than that with Hastings formula, since symmetric ambipolar fluxes play a role to reduce electric field produced by asymmetric ambipolar flux in Kovrizhnykh formula. However, these theory do not explain the electric field shear near the plasma edge. This large electric field measured near the plasma edge can be explained with orbit loss.

Negative electric filed has been observed in tokamak plasmas[9] and this negative electric field has been found to be more negative at the edge in H-mode[10,11]. Radial electric field should be related with the improvement of confinement. In order to demonstrate the location of good confinement, the gradient of electron pressure is calculated by fitting electron pressure profile measured with Thomson scattering. The good confinement region for high density case is at $r/a = 0.7$, where the both of negative E_r and $\partial E_r/\partial r$ are observed. On the other hand, no significant good confinement region is observed in low density case and electric field profiles has no shear near the plasma edge. We note that profiles both of electric field and of pressure gradients in high density case are similar to those measured in H-mode in tokamak[11]. However no bifurcation phenomena has been observed in CHS plasma between low density case and high density cases.

We would like to thank K.C.Shaing (ORNL) and Y.Ogawa for their useful discussions. Calculation with neoclassical has been done by K.Yamazaki. We would also thank S.Okamura, O.Kaneko, Takeiri for thier support of machine and NBI operation. We also thank the support of data acquisition by C.Takahashi and M.Kojima. Continuous encouragement by K.Matsuoka is acknowledged.

Reference

1L.M.Kovrizhnykh Nucl. Fusion 24 435 (1984).
2D.E.Hastings, W.A.Houlberg, K.C.Shaing, Nucl. Fusion 25 445 (1985).
3E.C.Crume, Jr.,K.C.Shaing, S.P.Hirshman, W.I.van Rij, Phys. Fluids 31 11 (1988).
4G.A. Hallock, J.Matthew, W.C. Jennings, R.C. Hickok, A.J. Wootton and R.C. Isle, Phy. Rev. Lett. 56 1248 (1986).
5K. Kondo, H. Zushi, S. Nishimura, et. al., Rev. Sci. Instrum. 59 (1988) 1533.
6K.Matsuoka et. al., in Plasma Physics and Controlled Nuclear Fusion Research (in Proc. 12th IAEA Conf. Nice, 1988) IAEA-CN-50/I-I-3.
7K.Ida and S. Hidekuma, Rev. Sci. Instrum. 60 876 (1989).
8K.Ida, T.Amano, K.Kawahata, O.Kaneko, H.Tawara, Nucl. Fusion 30 665 (1990).
9K.Ida et al. National Institute for Fusion Science Research Report NIFS-23 (1990).
10K.H.Burrell et al., Plasma Physics and Contr. Nucl. Fusion 31 1649 (1989).
11K.Ida et al. National Institute for Fusion Science Research Report NIFS-26 (1990).

Figure captions

Fig.1 (a) electron density and (b) electron and (c) ion temperature profile for low density and high density cases.

Fig.2 Profiles of (a) poloidal rotation velocity and (b) radial electric field for low and high density plasma produced by NBI.

Fig.3 Radial electric field profiles measured in CHS and neoclassical estimates. Solid lines are calculated radial electric field for high density plasma, while the dashed lines for low density plasma.

Fig.4 Radial profile of electron pressure gradient measured with Thomson scattering.

Figure captions

Fig.1 (a) electron density and (b) electron and (c) ion temperature profile for low density and high density cases.

Fig.2 Profiles of (a) poloidal rotation velocity and (b) radial electric field for low and high density plasma produced by NBI.

Fig.3 Radial electric field profiles measured in CHS and neoclassical estimates. Solid lines are calculated radial electric field for high density plasma, while the dashed lines for low density plasma.

Fig.4 Radial profile of electron pressure gradient measured with Thomson scattering.

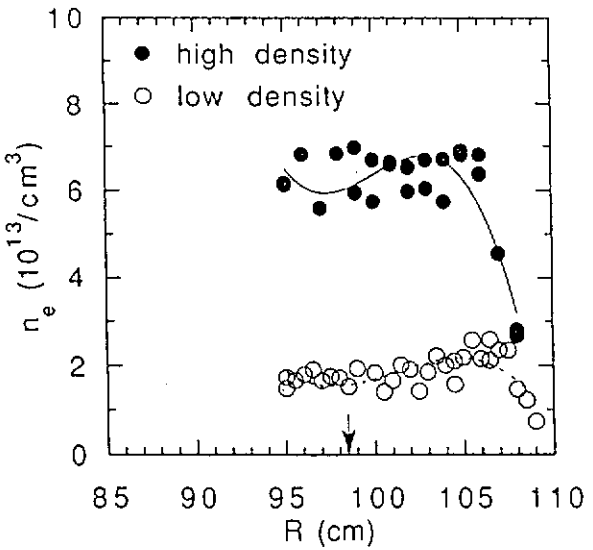

Figure 1 (a)

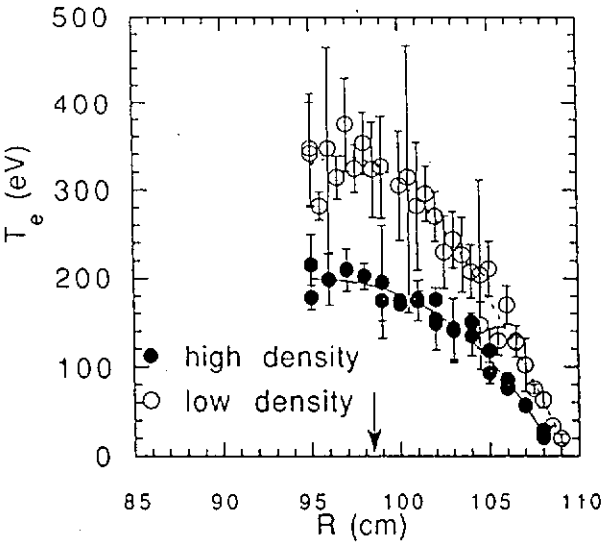

Figure 1 (b)

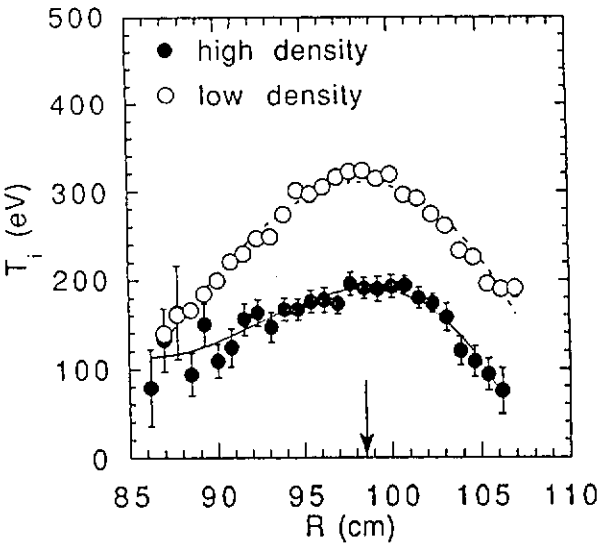

Figure 1 (c)

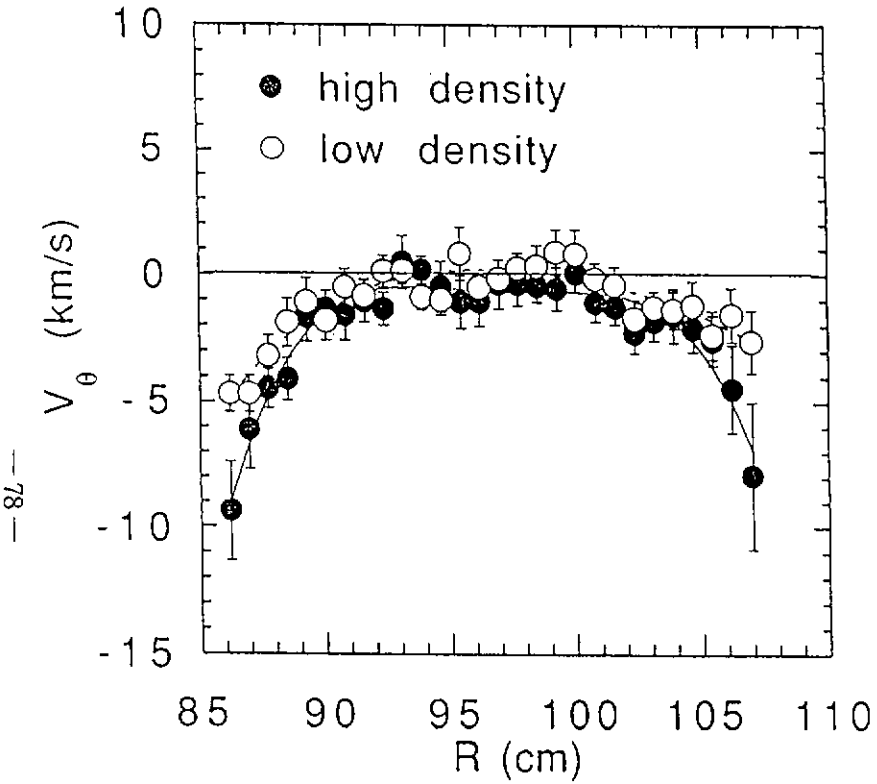

Figure 2(a) K.Ida et al.

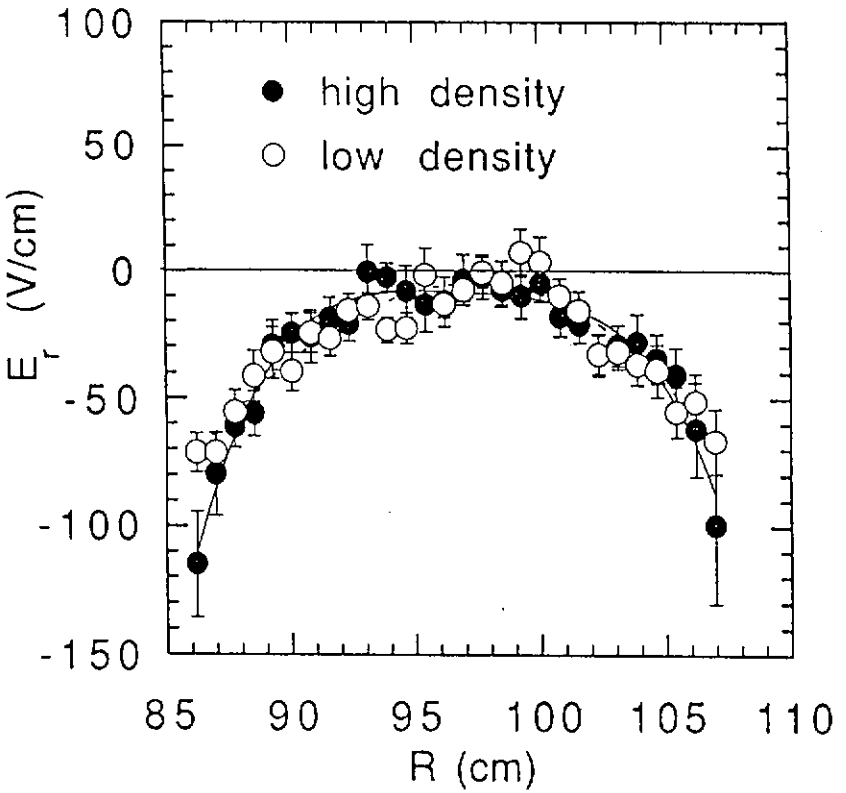

Figure 2(b) K.Ida et al.

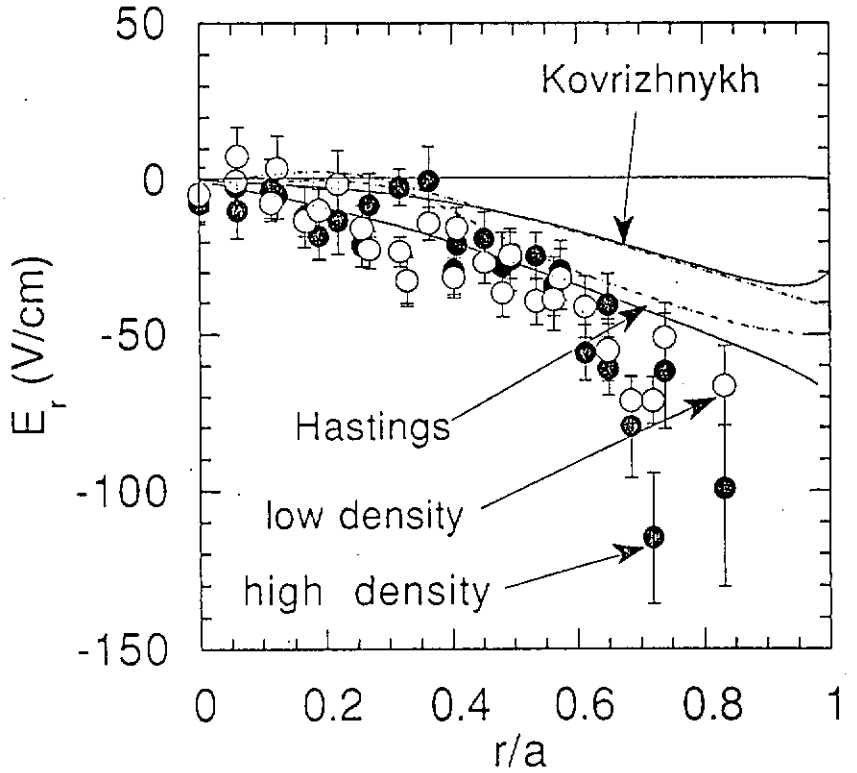

Figure 3 K.Ida et al.

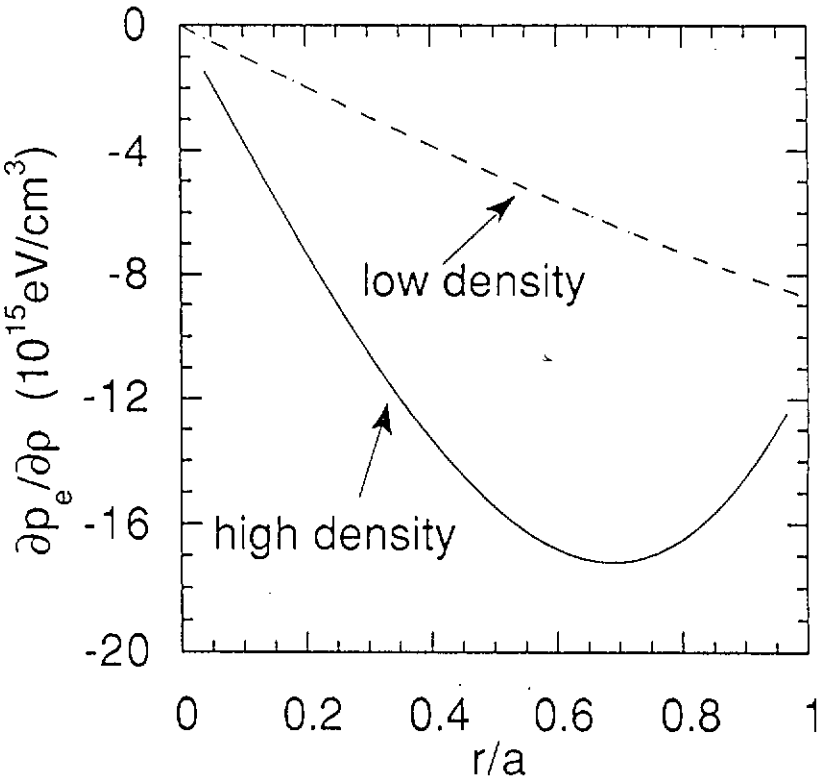

Figure 4 K.Ida et al.

X-Ray Spectra from High-Temperature Plasmas

Shigeru Morita
National Institute for Fusion Science

X-ray spectra (1-5Å) of Ti, Cr, Fe and Ni ions have been observed from the JIPPT-IIU tokamak and Heliotron E using crystal spectrometer. These spectra obtained are analyzed under considerations of various atomic processes in plasmas. The report gives brief summary on recent these results. In addition, a new crystal spectrometer is under construction for CHS stellarator to observe soft x-ray lines in a wavelength region of 10-40Å. Some calculations are presented for oxygen lines.

[I] JIPPT-IIU tokamak

A crystal spectrometer installed on the JIPPT-IIU tokamak is illustrated in Fig.1. The radius of focusing circle of the spectrometer is 3m and the crystal used is quartz(2023) with a area of 50x80mm^2. The spectra are displayed typically with a time interval of 10ms or 20ms.

Spectral resolution largely depends on a resolution of a crystal spectrometer. Figure 2 shows such a dependence. Upper two spectra are obtained using a crystal spectrometer with a focusing radius of 1m. The crystals used are different. Ge (2d=4.00Å) and quartz(2023) (2d=2.749Å) are used for top and middle displays, respectively. In a bottom display the quartz(2023) with a focusing radius of 3m, as described in Fig.1, is used. The spectral resolution obtained is indicated at each display. The corresponding ion temperature for each display is 100keV, 5keV and 300eV, respectively. From the top display we can get charge state distribution of the plasma. In contrast to it, detailed structures of heliumlike spectra of titanium ions are observed from the bottom spectrum. Using the bottom spectrum we can get ion temperature, electron temperature and toroidal rotation speed of the plasma.

A typical example of Doppler-broadened heliumlike titanium resonance line is shown in Fig.3. The plasma is additionally heated by

2MW ICRF injection during 140-200ms. The ion temperature obtained is indicated at each display. The line fitting with Voigt function which is indicated by solid curve is carried out at shorter wavelength side of the line, because many higher-order satellites are included at longer wavelength side of the line. The ion temperature obtained is compared with one from Fast Neutral Particle Energy Analyzer (FNA) as shown in Fig.4. Agreement during ICRF heating phase is very good. However, there is some disagreement between ion temperatures obtained from the crystal spectrometer and FNA in ohmic heating phase. The origin is not clear at present.

The toroidal rotation speed of the plasma is determined from Doppler shift of the heliumlike titanium line as shown in Fig.5. In ohmic phase the direction of the toroidal rotation is opposite to that of the plasma current and the speed is about 5×10^{3}m/s. In ICRF heating phase the rotation is accelerated to 2×10^{4}m/s. This acceleration is related to an increase of a radial electric field due to an increase of a plasma potential.

Typical example of an electron temperature measurement from an intensity ratio of n=3 dielectronic satellite lines to heliumlike titanium resonance line is shown in Fig.6. A dotted curve is obtained from ECE measurement calibrated with Thomson scattering. The discrepancy is remarkable at the ohmic phase, whereas it is small at ICRF heating phase. The difference clearly depends on the electron density. In the ICRF phase the electron density reaches 1×10^{14}cm^{-3}. Runaway electrons accelerated by a toroidal electric field are disappeared at such a high-density region. However, the electron density is normally less than 4×10^{13}cm^{-3} at the ohmic phase. There are lots of runaway electrons in the ohmic phase. It leads to enhancement of the heliumlike titanium line intensity. As a result, higher electron temperature is given from the calculation of the line intensity.

On the other hand, we can calculate a quantity of the runaway electrons or nonthermal electrons from the discrepancy of the electron temperature at the ohmic phase. The result is shown in Fig.7. At low electron density region the nonthermal electron abundance n_t ($=n_s/n_e$) increases up to 0.6% (n_s:nonthermal electron density, n_e:thermal electron density), since a collision frequency of the runaway electrons largely decreases for decreasing electron density. At high electron density of

$8x10^{13}cm^{-3}$ the nonthermal electron percentage is close to zero. It can be well explained with the analysis on the runaway electron in tokamak.

A full spectrum of iron 2p-1s transitions is shown in Fig.8. It is noticed that inner-shell excitation lines are very strong. From these line intensities we can see that beryllium like ions are dominant in the ICRF heated plasma. These spectral feature is strongly related to a transport of the ions in the plasma as described later. The analysis of the spectrum is in progress.

[II] **Heliotron E**

Charge state distributions of titanium ions in a central column of the Heliotron E ECH plasma were measured using a broad-band crystal spectrometer. The typical result is shown in Fig.9. The electron temperature and density are 800eV and $1x10^{13}cm^{-3}$, respectively. The intensity ratio of the 2p-1s transitions among charge states is a function of the transport coefficient of the ions. Calculations on the intensity ratio are carried out to determine the transport coefficient of the titanium ions in the ECH plasma, as shown in Fig.10. A value of D indicates the transport coefficient and it is called "diffusion coefficient". A particle confinement time τ_p of the ions in the plasma can be related with the diffusion coefficient ($\tau_p=r^2/5.8D^2$, r:plasma radius (20cm)). The spectrum obtained experimentally can be explained with the diffusion coefficient of $3000cm^2/s$. This value shows roughly good agreement with a result of impurity transport study using laser-blow-off experiment. However, a detailed study is disturbed by a lack of the knowledge on the detailed line structure and some uncertainties on the emission rate of the titanium 2p-1s transition.

[III] **CHS stellarator**

A new crystal spectrometer is designed for the x-ray spectroscopy of CHS stellarator. The spectrometer is constructed for an observation of carbon and oxygen Kα transition and titanium, chromium and iron Lα transition. Typical wavelength range of the spectrometer is 10-40Å. Spectral dispersion is 135mm/Å at heliumlike oxygen 21.6Å and spectral resolution will be more than 10^4. Calculations for the study are done on heliumlike oxygen ions as shown in Figs.11 and 12. In the case of an electron temperature of 100eV (see Fig.11) lithiumlike satellites may be

observed. The intensity ratios among the heliumlike ions (w: resonance line, x,y: intercombination line, z: forbidden line) are a function of the electron temperature and density. Then, at higher electron temperature (see Fig.12) the resonance line w becomes dominant. As a result, this tendency gives us an information of electron temperature and density.

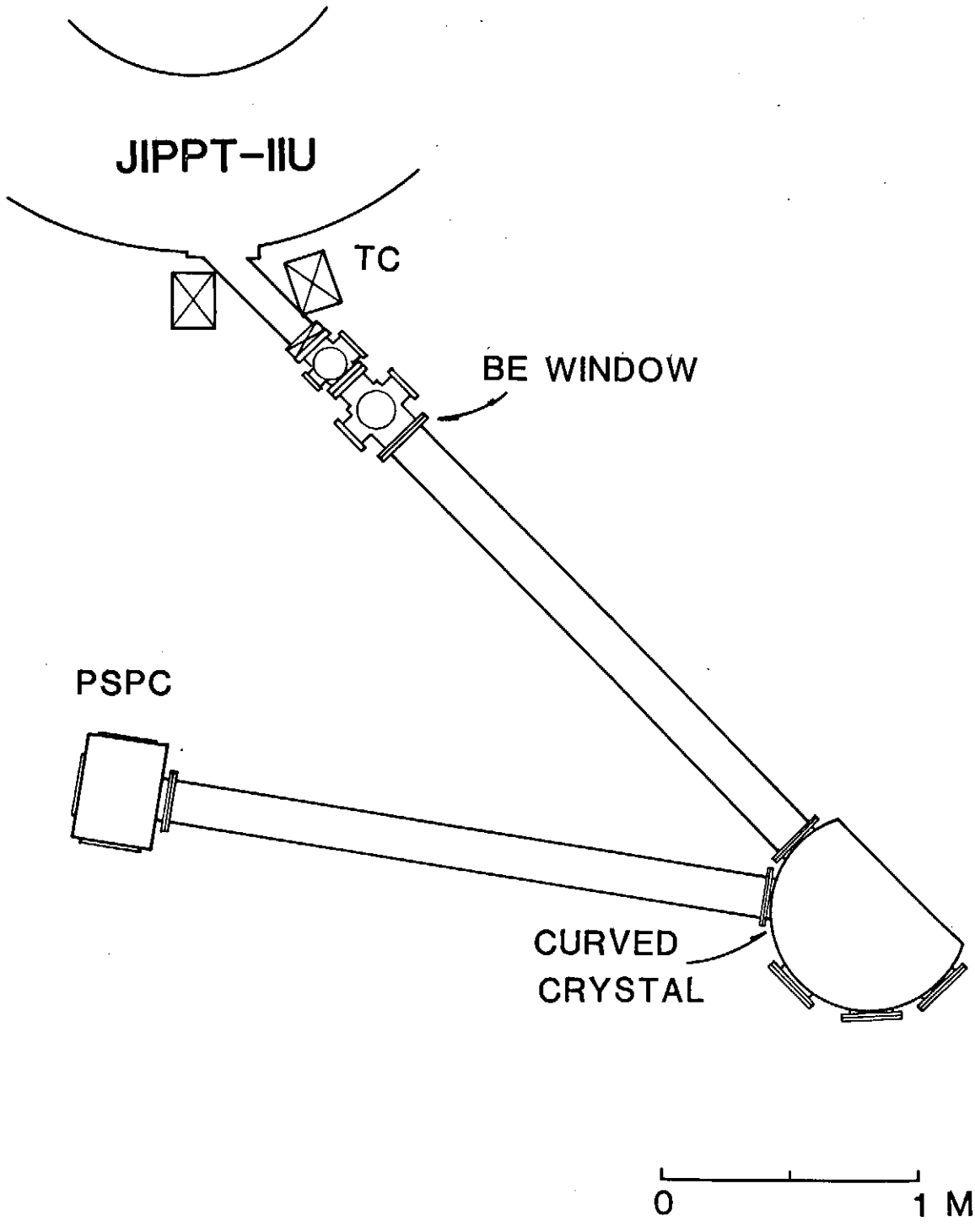

Fig.1 High-resolution crystal spectrometer installed on JIPPT-IIU.

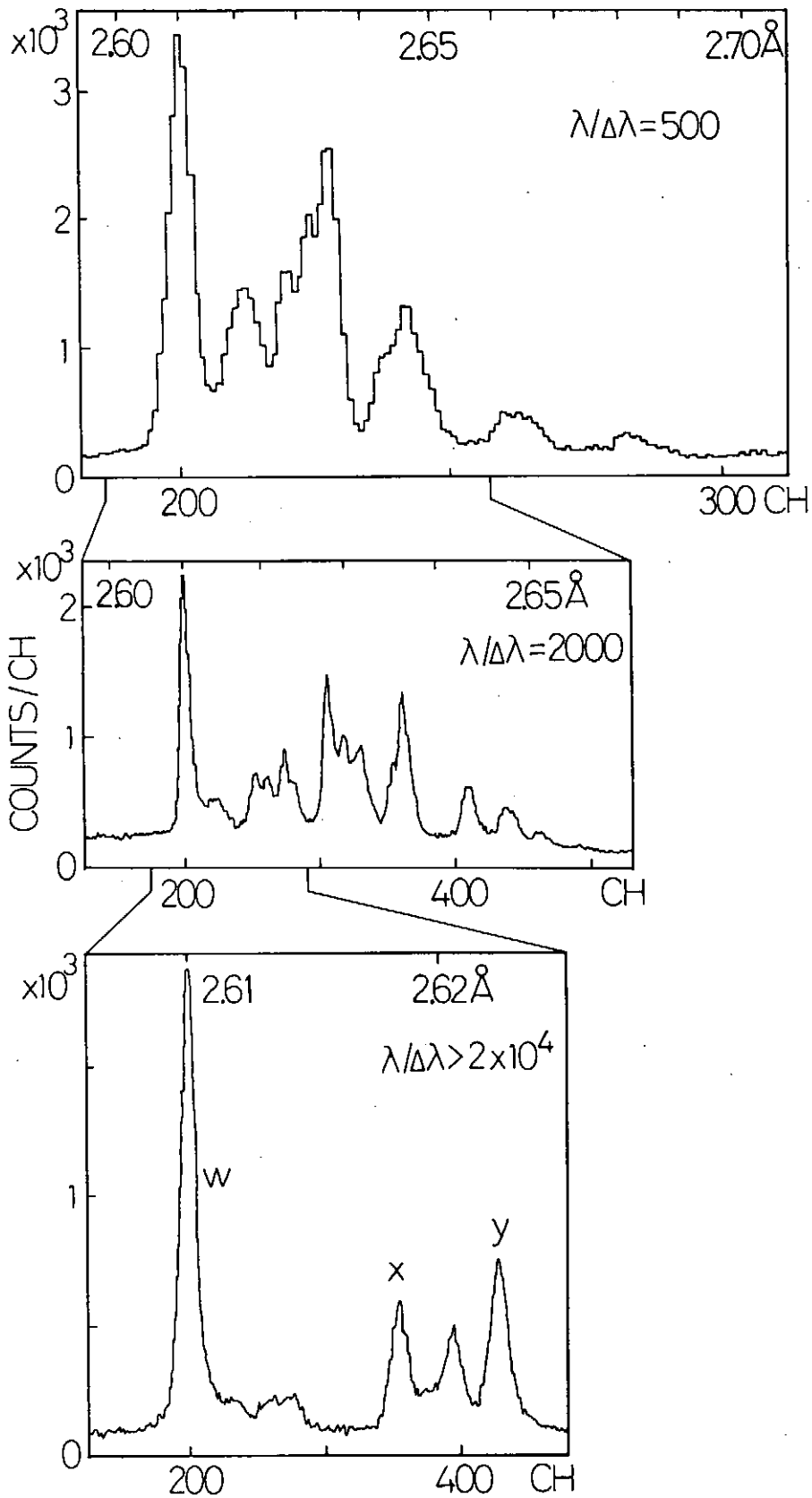

Fig.2 Titanium Kα spectra with different spectral resolution.

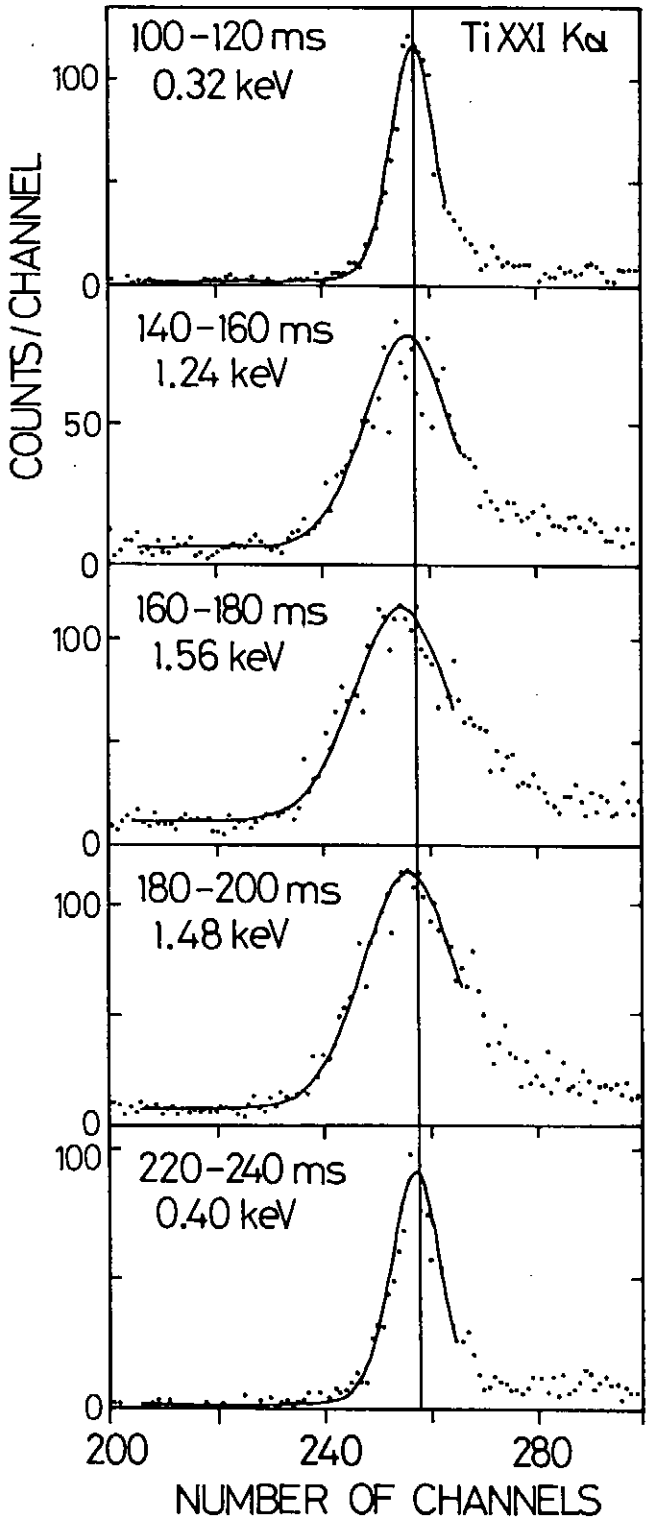

Fig.3 Doppler-broadened titanium heliumlike resonance line.

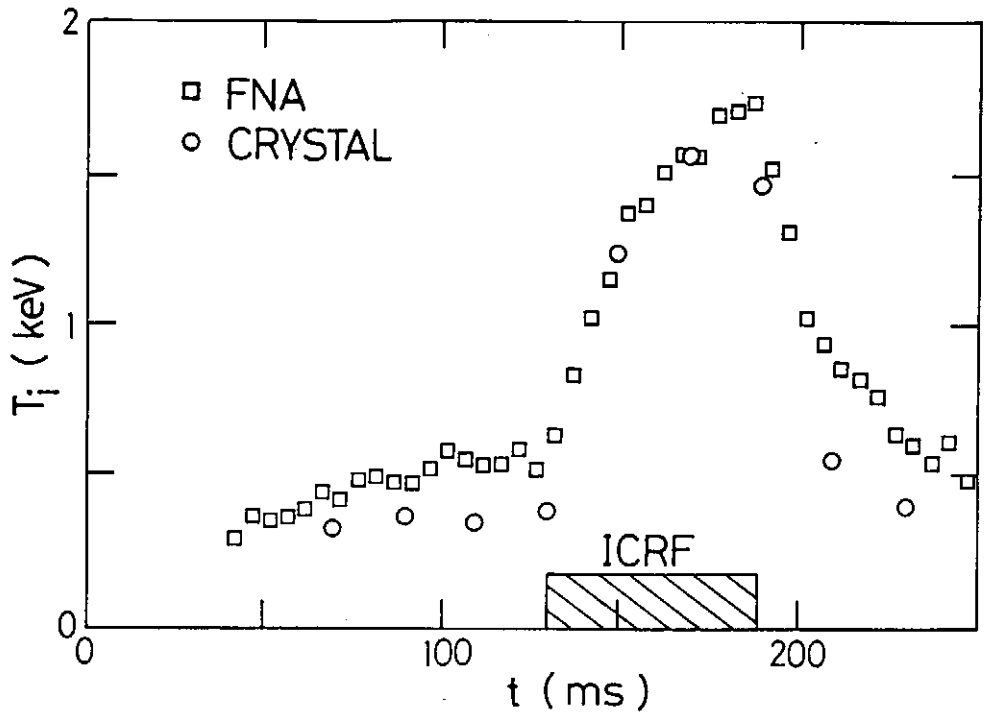

Fig.4 Comparison of ion temperatures obtained from Fast Neutral Particle Energy Analyzer (FNA) and crystal spectrometer.

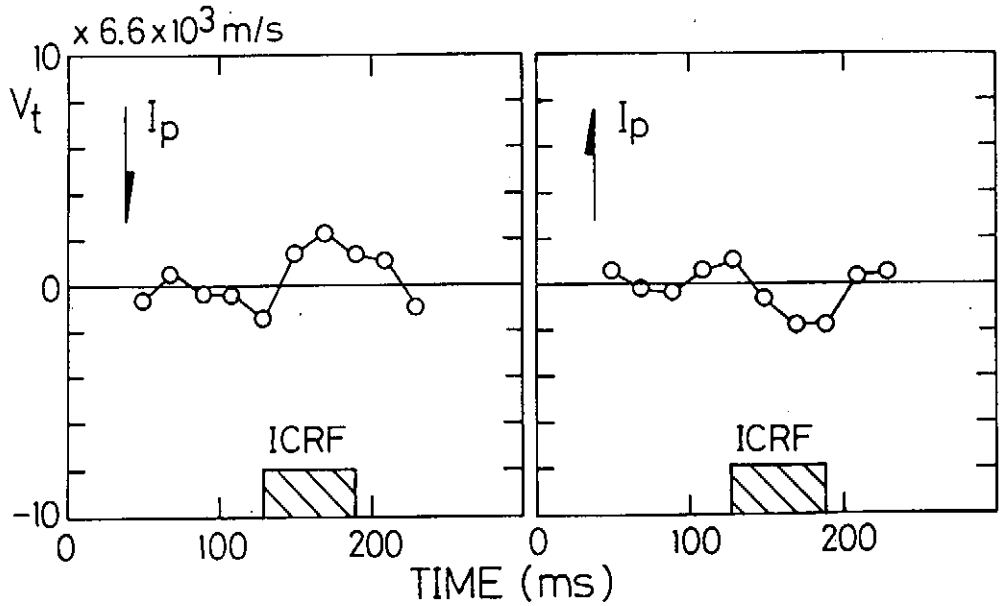

Fig.5 Toroidal rotation measurement using Doppler shift of titanium heliumlike resonance line.

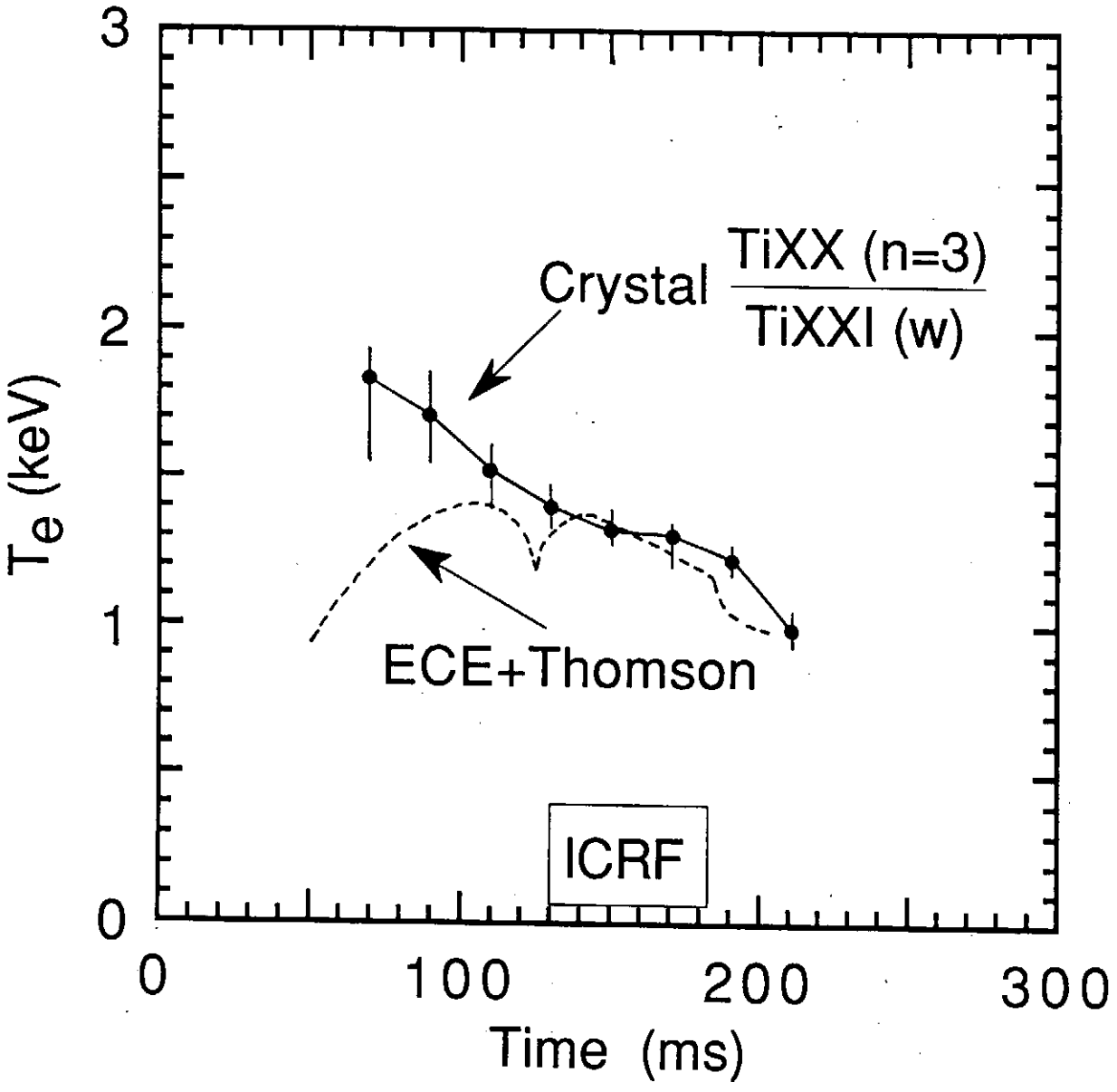

Fig.6 Comparison of electron temperatures obtained from Electron Cyclotron Emission (ECE) calibrated with Thomson scattering measurement and crystal spectrometer.

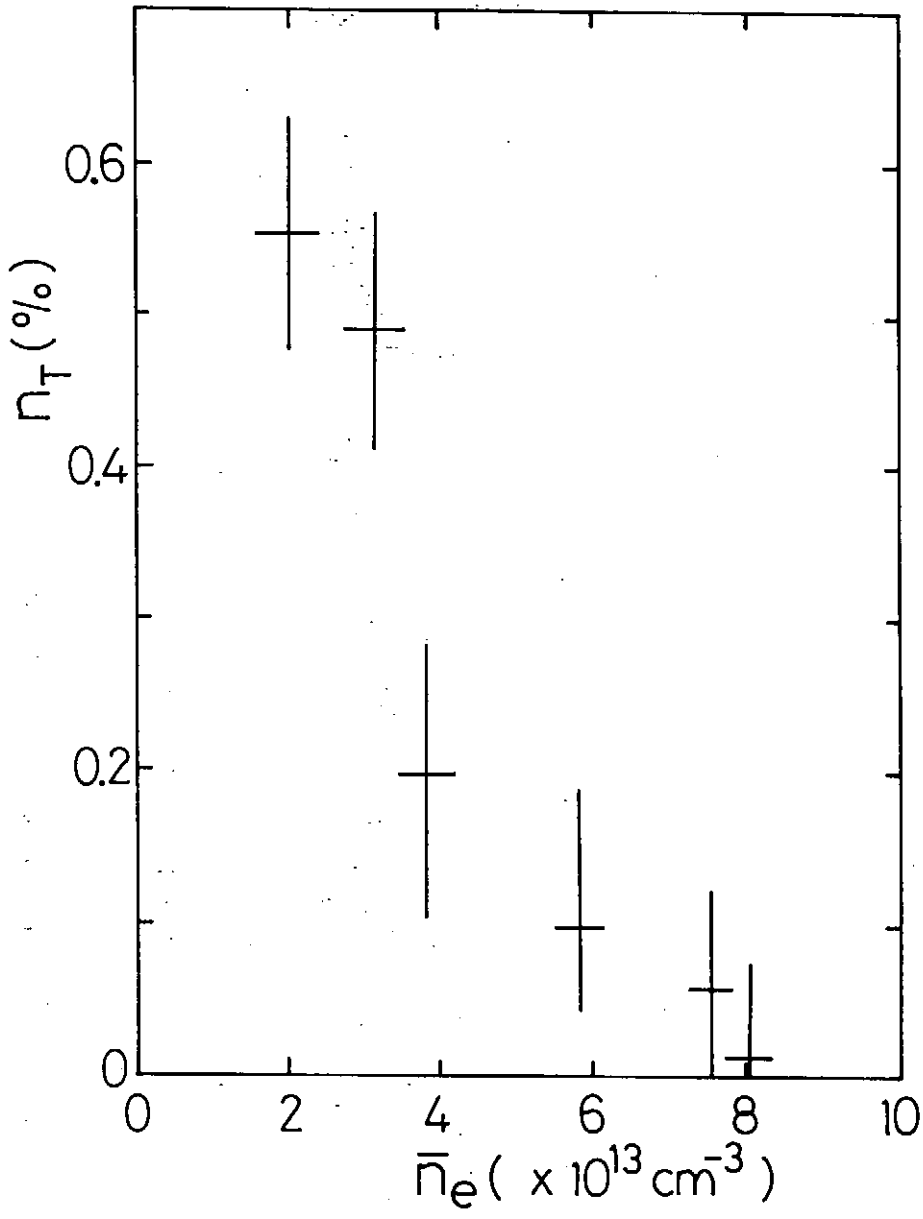

Fig.7 Nonthermal electron percentage in JIPPT-IIU.

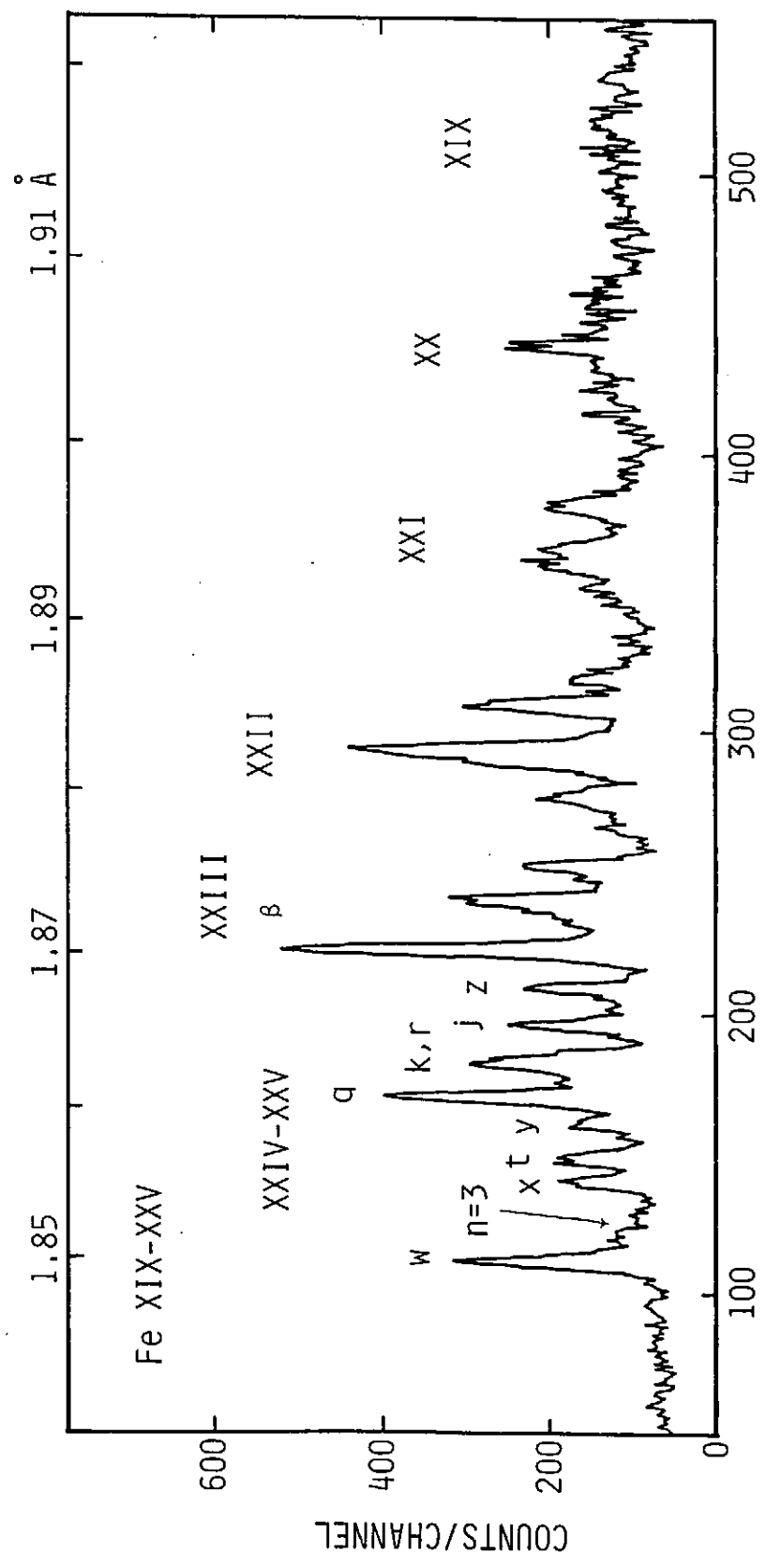

Fig.8 Full Kα spectrum of iron ions.

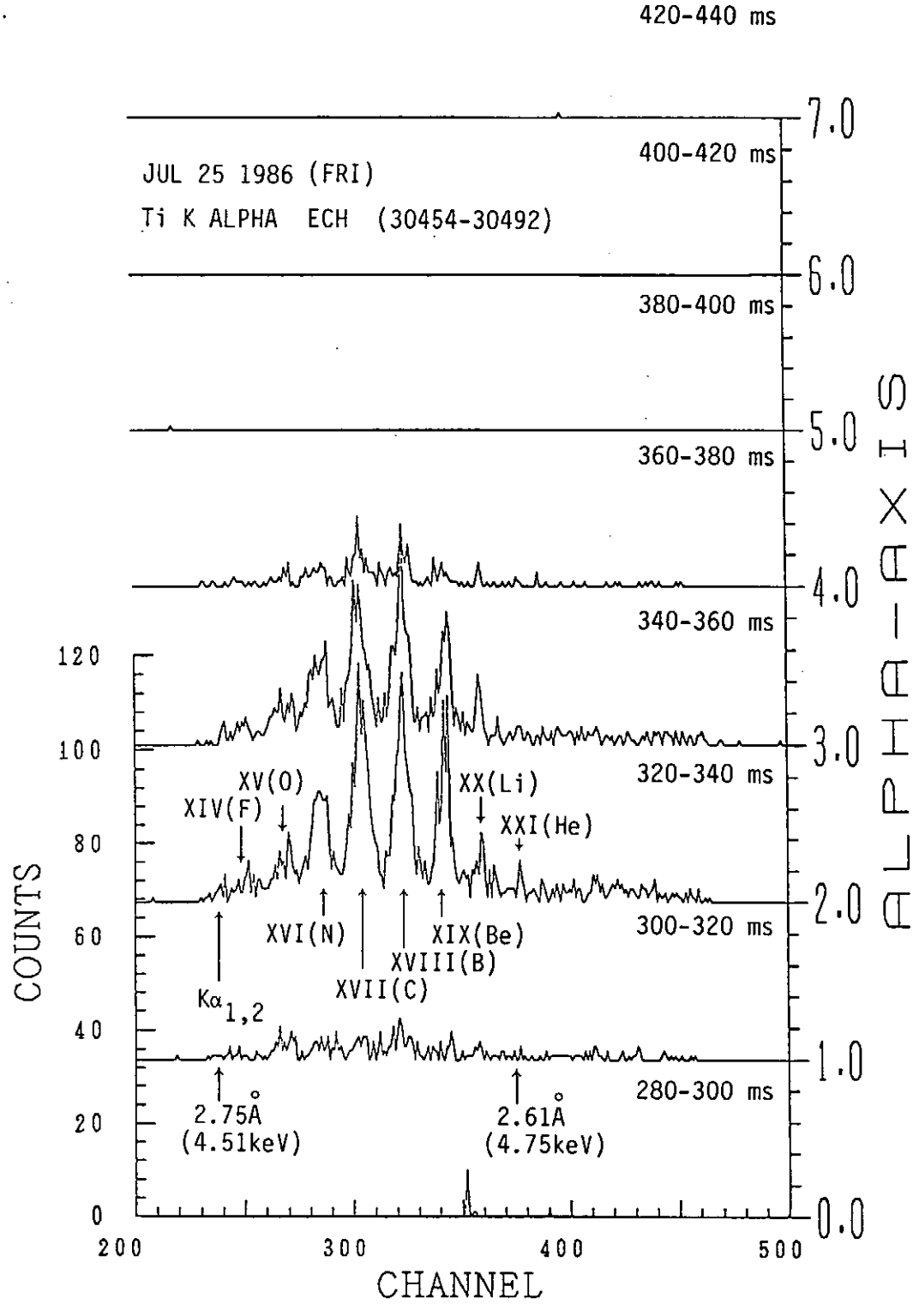

Fig.9 Charge state distribution of titanium ions in Heliotron ECH plasma.

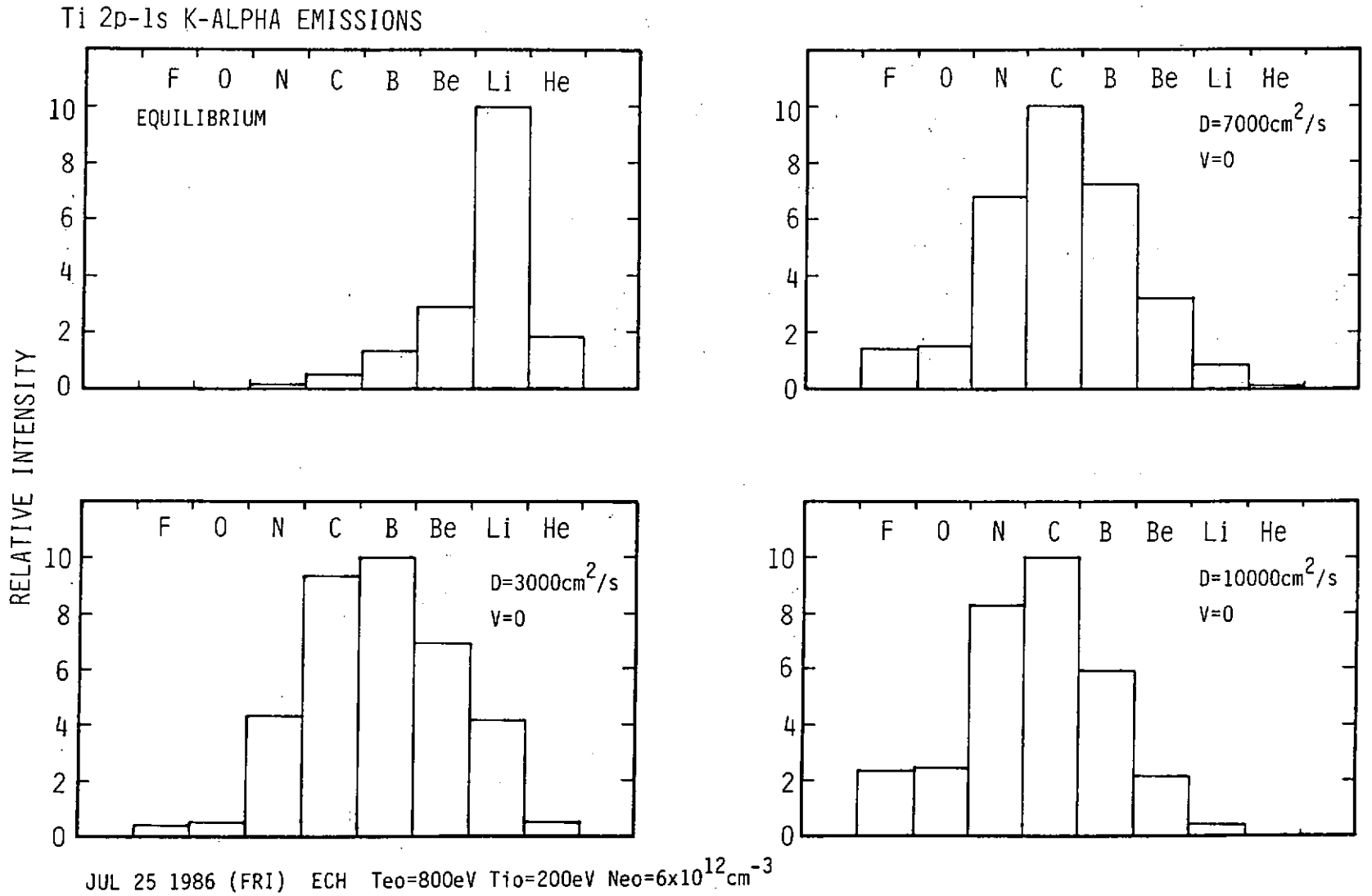

Fig.10 Calculation of charge state distribution of titanium ions as a function of transport coefficient D.

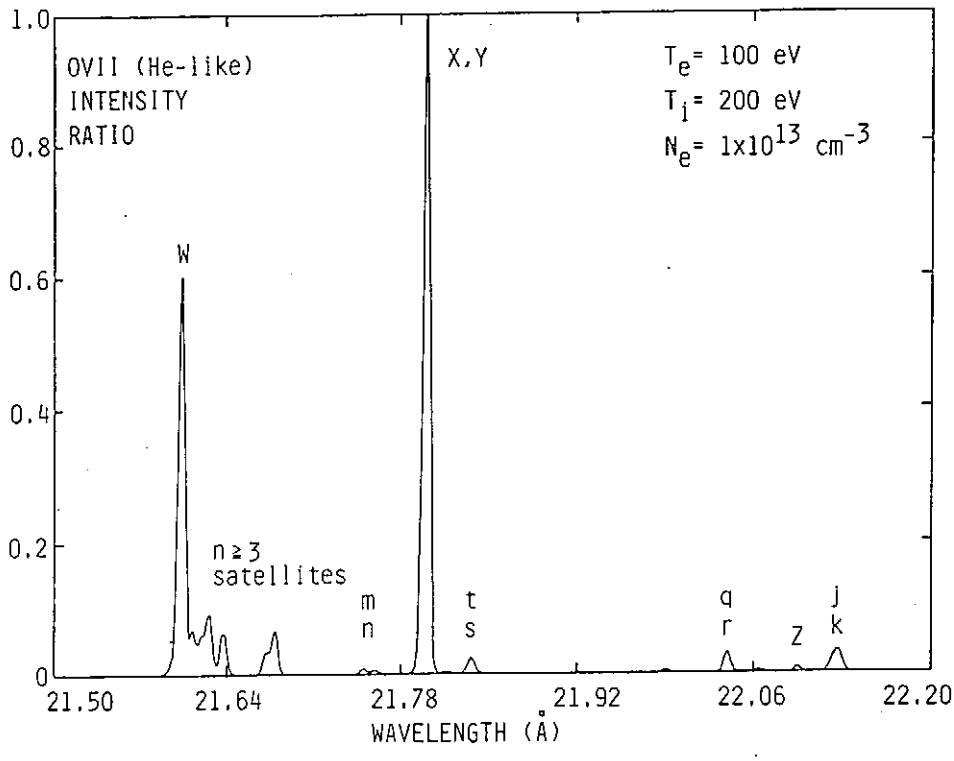

Fig.11 Calculation of heliumlike oxygen Kα transition (T_e=100eV).

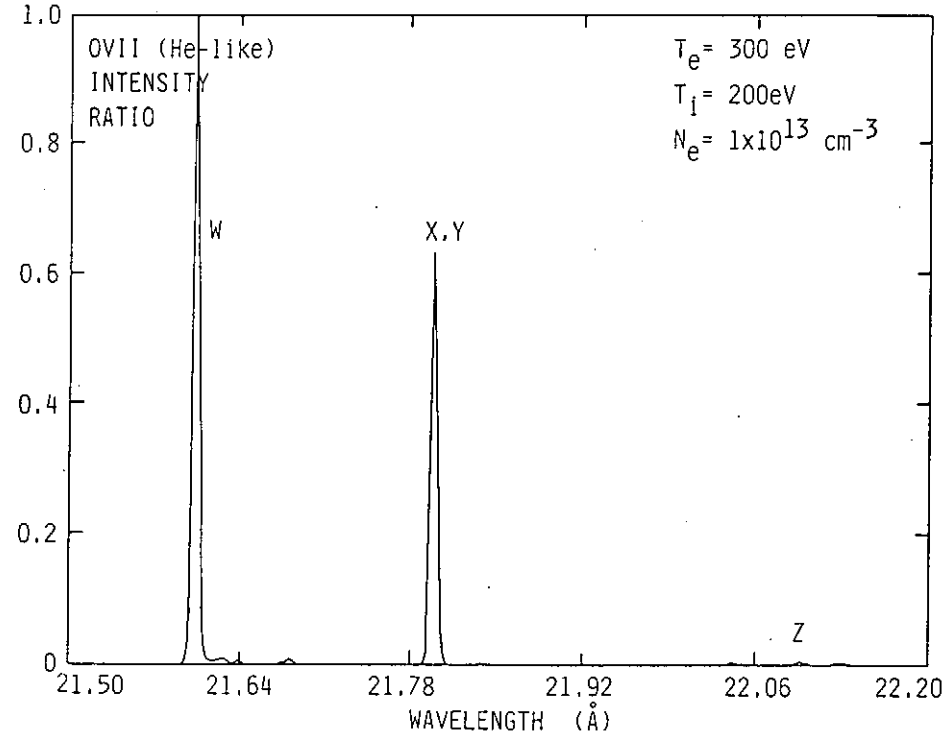

Fig.12 Calculation of heliumlike oxygen Kα transition (T_e=300eV).

X-Ray Amplification at 54.2 A on Balmer α Transition of H-Like Sodium

H.Shiraga and Y.Kato

Institute of Laser Engineering, Osaka University
2-6 Yamada-Oka, Suita, Osaka 565

Abstract

Planer and foil targets coated with NaF were irradiated with high intensity 351 nm laser radiation of 130 ps duration. Time-integrated gain of Na XI Hα at 54.2 A were measured to be $1.2^{+0.8}_{-1.1}$ cm^{-1}.

Introduction

One of the important objectives of the current X-ray laser research is to develop a soft X-ray laser useful for high-resolution holographic imaging of biological specimens. Recent theoretical study shows that the optimum laser wavelength for this application will be very close to, but slightly longer than the carbon K-edge at 43.7 A [1] . With electron-collisional excitation, amplification at 53.0 A was observed with Ni-like Yb [2] and theoretical evaluation for the Ni-like W laser at 43.1 A has been reported [3] .

Isoelectronic scaling of the recombination-pumped Hα laser to shorter wavelength requires target irradiation with short wavelength and short pulse laser at high irradiation intensity. We have performed an experiment on the Hα laser in order to observe amplification near and below 50 A. Stripe targets were irradiated with a 351 nm, 130 ps laser pulse and evidence for gain on Na XI Hα at 54.2 A was obtained in time-integrated measurement [4] .

Experimental Conditions

The experiment was carried out on GEKKO-XII neodymium glass

laser facility at the Institute of Laser Engineering, Osaka University. One of its 12 beams were used for this experiment in an optical layout shown in Fig. 1. The laser beam of 1053nm wavelength and 32 cm beam diameter was frequency-tripled to 351 nm with two KDP crystals. A combination of a weak negative cylindrical lens and an f/3 1 m aspheric lens produced 7-mm long line focus on target. The width of the line focus measured from the time-integrated X-ray emission pattern was 50 μ m in FWHM intensity. The UV laser energy on target was 63 J at a pulse length of 130 ps, corresponding to the intensity of 1.4×10^{14} W/cm^2.

The foil target was a 0.2 μ m-thick NaF coated over one surface of a 0.13 μ m-thick CH plastic foil. The target was positioned carefully relative to the line focus so that the 6 mm length was completely covered by the 7 mm long line focus in order to avoid the edge effects.

Two XUV spectrometers were used for spectroscopic diagnostics. Each of these spectrometers was equipped with a 3^0 grazing incidence spherical focusing mirror which formed a 10:1 reduced astigmatic image of the source onto the slit. The first spectrometer, aligned onto the target axis, had a 1200 lines/mm variable spacing diffraction grating for flat field recording of the spectra operated at 3.2^0. With X-ray film recording, it gave spectra from 30 A to 370 A with a resolution of 0.2 A at around 50 A. The second spectrometer positioned 60^0 off-axis had a 2400 lines/mm variable spacing grating operated at 1.2^0 grazing angle. It gave photographic spectra from 6 A to 150 A with 0.1 A resolution near 50 A. The spectra were recorded with calibrated Kodak 101-07 film. Time integrated X-ray emission image of the target was recorded with an X-ray slit camera which was composed of two orthogonal slits to provide a higher magnification perpendicular to the line focus.

Results

The procedure for gain determination used in this experiment was to compare the intensities emitted along (I_a) and transverse (I_t) to the X-ray laser axis. Approximating the plasma as a long

column of length L and area A, these intensities are given respectively by $I_a = I_{sp} A [\exp(gL)-1] / g$ and $I_t = I_{sp} AL$, where I_{sp} is the spontaneous emission intensity per unit volume. This is valid when the opacity along the transverse direction is small. Since

$$I_a/I_t = [\exp(gL)-1] / (gL) \qquad (1)$$

we can determine the gain-length product from I_a/I_t.

High spectral resolution achieved by recording spectra with the film enabled us to resolve and accurately assign spectral lines, and to determine gain or loss of each line. Line shapes of the axial and transverse spectra of NaF near 54 A are shown in Fig.2. The Na XI Hα is composed of a doublet structure, J=5/2-3/2 line at 54.194 A and J=3/2-1/2 line at 54.052 A, and is closely overlapped with Na IX $4p^2P$-$2s^2S$ at 53.860 A and slightly with F IX $5d^2D$-$2p^2P$ at 53.527 A. Although these lines are not clearly resolved in the spectra shown in Fig.2, we can determine the relative intensities and evaluate mutual overlaps knowing the wavelength of these lines and the spectral resolution curve of each spectrometer derived from nearby isolated spectral lines. The thin dotted curves in Fig.2 show the deconvoluted shapes of each line and thin line-dot curves are the convoluted lines shapes. The agreement between the data and the convoluted shape is less in Fig.2b due to smaller intensity of the transverse spectrum. From this analysis, we can evaluate the overlaps of the nearby lines to the Hα J=5/2-3/2 line which should show the highest gain.

Comparing the axial and transverse spectra shown in Fig.2, we find that the intensities of the Na XI Hα doublet relative to the Na IX $4p^2P$-$2s^2S$ line are stronger in the axial direction. By using the calibration data for the relative sensitivity of the spectrometers the actual I_a/I_t ratio is determined for each line and the result is given in Fig.2c. The Hα doublet have I_a/I_t larger than 1 showing that they have gain, whereas the resonance line of the Li-like Na has $I_a/I_t < 1$ showing it has absorption. The J=5/2-3/2 component of Hα has a higher gain than the J=3/2-

1/2 component as expected. The gL value is determined from the I_a/I_t ratio using (1) and then the gain coefficient g using L=0.6 cm to be $1.2^{+0.8}_{-1.1}$.

Conclusion

We have presented time-integrated measurement of gain on Na XI Hα at 54.2 A. Planer foil targets coated with NaF were irradiated with 351 nm laser light. Gain coefficient of $1.2^{+0.8}_{-1.1}$ was obtained. Finally we note that in the present experiment, gain on Mg XII Hα at 45.5 A was also measured and a time-integrated gain larger than the value for Na XI Hα was obtained. These results suggest that it will be possible to achieve significant gain at the wavelength near to, and possibly within, the water window when the irradiation conditions are optimized.

References

[1] R.A.London, M.D.Rosen, J.E.Trebes:Appl. Opt. 28,3397(1989).

[2] B.J.MacGowan, S.Maxon, C.J.Keane, R.A.London, D.L.Matthews, D.A.Whelan:J. Opt. Soc. Am. B5, 1858(1988).

[3] S.Maxon, S.Dalhed, P.L.Hagelstein, R.A.London, B.J.MacGowan, M.D.Rosen, G.Charatis, G.Busch: Phys. Rev. Lett. 63, 236(1989).

[4] Y.Kato, E.Miura, T.Tachi, H.Shiraga, H.Nishimura, H.Daido, M.Yamanaka, T.Jitsuno, M.Takagi, P.R.Herman, H.Takabe, S.Nakai, C.Yamanaka, M.H.Key, G.J.Tallents, S.J.Rose, and P.T. Rumsby:Appl. Phys. B, 50,247(1990).

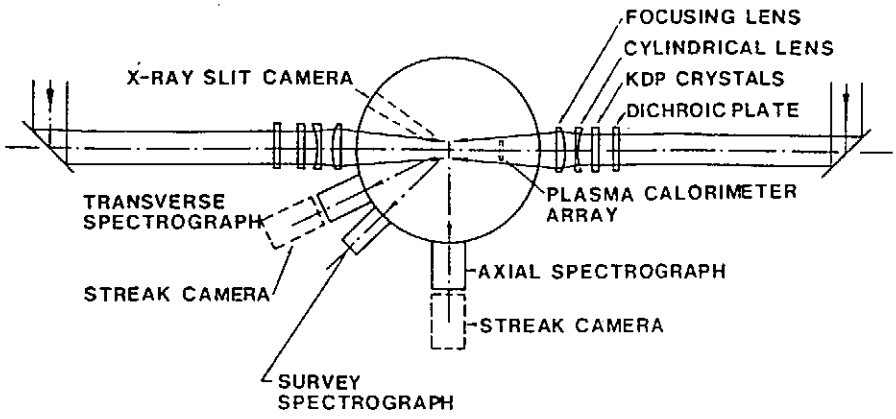

Fig.1. Layout of the laser beams and the diagnostic equipment.

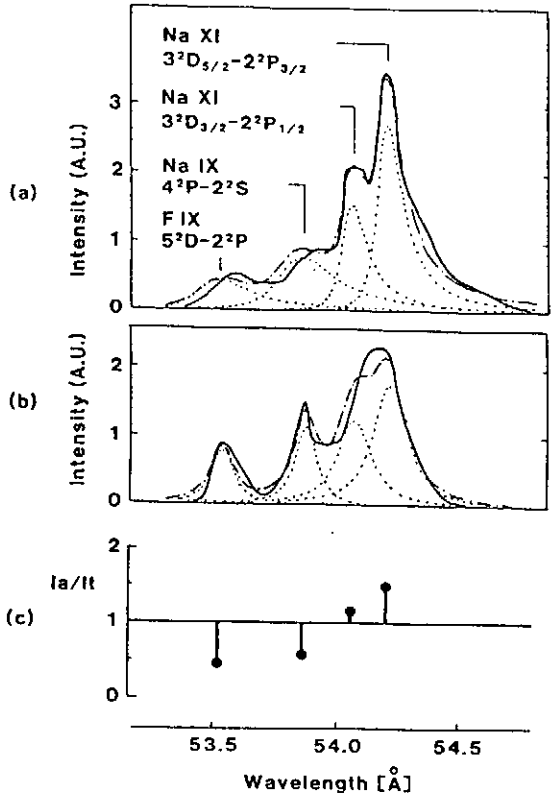

Fig.2. The thick solid curves show observed spectral profiles at 53.3-54.7 A for (a) axial and (b) transverse spectra. The Na XI H α J=5/2-3/2 and J=3/2-1/2 doublet are blended with Na IX 4p-2s and F IX 5d-2p lines. The thin dotted curves are the deconvoluted line shapes of these lines and thin line-dotted curves are the convoluted line shapes. The axial-to-transverse intensity ratio for each line is shown in (c).

Numerical Calculation of Atoms in Plasmas

Kazumi Fujima

Faculty of Engineering, Yamanashi University
Takeda 4, Kofu,
Yamanashi 400 Japan

$Introduction

The selection of tools of studying electronic structures in plasmas sometimes needs special care because of the complicated electronic environment in plasmas. Since many highly ionized ions are moving and interacting each other in plasmas, the number of orbitals should be accounted is usually much larger than that in an isolated system. Very sophisticated and accurate methods do not necessary work well in this field. Among these the discrete variational Xα method (DV-Xα method hereafter) provides one of the effective and practical tools. Thought this method has been applied to a plenty of molecules, solids, and solid surfaces, its basis idea is not familiar in the field of plasma physics. So, we like to review the fundamental idea of the DV-Xα method and numerical procedure for the better understandings and the help in the future application.

This report provides a brief sketch of Xα approximation first. Next, the numerical procedure of the DV-Xα method is summarized. As one of examples, we show how we calculates the charge transfer cross sections with the wavefunction obtained. An interesting result obtained by this method is reported elsewhere in this brochure as a separated article.

$Xα Approximation.

A modern understanding of the Xα-method takes it as a variety of density functional methods. However, starting with an ordinary Hartree-Fock equation and deriving the Xα approximation following J.C.Slater[1] is easy to understand and get the idea of it. Let's start with a total energy expression E_{HF} of the Hatree-Fock scheme. With the total wavefunction of n-electon system $\psi(r_1, r_2, \ldots, r_n)$ in a single Slater determinant

$$\psi(r_1, r_2, \cdots, r_n) = \frac{1}{\sqrt{n!}} \begin{vmatrix} u_1(r_1), & u_1(r_2), & \cdots, & u_1(r_n) \\ & & & \\ u_n(r_1), & u_n(r_2), & \cdots, & u_n(r_n) \end{vmatrix} \qquad 1$$

the total energy E_{HF} is

$$E_{HF} = \sum_i \int u_i^* f_i u_i \, dr_i + \sum_{i \neq j} \iint u_i^*(r_1) u_j^*(r_2) \, 2/r_{12} \, u_i(r_1) u_j(r_2) \, dr_1 dr_2 - \sum_{i \neq j} \iint u_i^*(r_1) u_j^*(r_2) \, 2/r_{12} \, u_j(r_1) u_i(r_2) \, dr_1 dr_2 \qquad 2$$

where f_i stands for the kinetic energy and nuclear Coulomb potential for i-th orbital and r_{12} represents the distance between r_1 and r_2.

A variational method minimizing E_{HF} leads the well known Hatree-Fock equation,

$$f_K U_K(r_1) + \int \rho(r_2) 2/r_{12}\, dr_2\, U_K(r_1) - \sum_j \left[\int U_j^*(r_2) 2/r_{12}\, U_K(r_2)\, dr_2\right] U_j(r_1) = \varepsilon_K U_K(r_1). \quad (3)$$

As is known well, the third term in eq. 2 is called the exchange interaction. This can not be written in the form of local potential and differs between orbitals. Most numerical difficulties comes from this integration. The Xα approximation is drived so to eliminate this non-local potential and modifies it into a fairly accurate unique potential for every orbital by averaging with the weight of the probabilities finding an electron at position r in the k-th orbital: i.e.,

$$\frac{U_K^*(r)\, U_K(r)}{\sum_j U_j^*(r) \cdot U_j(r)} . \quad (4)$$

With this manipulation the exchange interaction becomes

$$[V_{ex}]_{av} = \frac{\sum_{i,j} \int U_i^*(r_1)\, U_j^*(r_2) 2/r_{12}\, U_j(r_1)\, U_i(r_2)\, dr_2}{\sum_j U_j^*(r_1)\, U_j(r_1)} . \quad (5)$$

The next step of the Xα-approximation is to substitute the real set of the wavefunctions with that of non-interacting ideal gas which has the same electron density p(r) as that of the real system at position r.

Substituting U_i in eq. 5 with $1/\sqrt{V}\, \exp(ik_i.r_1)$, the straightforward calculation makes the exchange interaction into

$$[V_{ex}]_{av} = -\frac{1}{V^2} \frac{\sum_{i,j} \int \exp[i(k_i - k_j)\cdot(r_2 - r_1)] 2/r_{12}\, dr_2}{\rho(r_1)}$$

$$= -6\left[\frac{3}{4\pi}\rho(r)\right]^{1/3} . \quad (6)$$

Now we get an unique potential $V_{ex}(r)$ for every electron. This procedure mentioned above was originally derived by J.C.Slater. However, Kohn and Sham[2] took a different approach to get a local exchange potential applying an interacting electron gas with full account of electron correlation. Their results reduces the exchange correlation of the Slater by the factor 2/3. As is shown by Kohn and Sham, the total energy of the n-electron system can be written as an unique functional of charge density p(r). So it

is practical to introduce an uncountable parameter α and write the exchange correlation,

$$V_{ex}(r) = -6\alpha\left[\frac{3}{4\pi}\rho(r)\right]^{1/3}. \qquad 7$$

The total Hamiltonian of the system with Xα approximation can be written as,

$$E_{X\alpha} = \sum_i \int u_i^* f_i u_i \, dr_1 + \frac{1}{2}\iint \rho(r_1)^2/r_{12}\,\rho(r_2)\,dr_1\,dr_2 - \frac{9}{2}\alpha\left(\frac{3}{4\pi}\right)^{1/3}\int \rho(r_1)^{4/3}\,dr_1 . \qquad 8$$

We started the discussion with the single Slater determinant eq.1. Adjusting the parameter α, it is possible to make the total energy calculated by the Xα-approximation be the same with that calculated with a superposition of number of Slater determinants. This means we can indeed take the exchange correlation into account in the framework of Xα approximation. However α is fixed to be 2/3 or 0.7 throughout the calculation.

$ Discrete Variational Method

Though Xα-approximation reduces much of computational effects, we still have to over come multi-center integration for many atom systems. The integration technique depends on the basis function we use, i.e., Slater or Gaussian type. The DV-Xα method uses a kind of Monte Carlo integration with numerically solved Slater-type atomic basis functions. Let's write the one-electon molecular wavefunction u(r) in the scheme of Linear Combination of Atomic Orbital (LCAO-MO)

$$u(r) = \sum_j C_j \chi_j(r) \qquad 9$$

where X(r) is what we call symmetrized can be written as

$$\chi_j(r) = \sum_{\mu,n,l,m} W^j_{\mu,n,l,m}\,\phi_{AO}^{\mu,n,l,m}(r) \qquad 10$$

where W are the coefficients which reflect the geometrical symmetry of the system.

The atomic basis function ϕ_{AO} in eq. 10 is the product of radial wavefunction R(r) and spherical harmonics $P_l^m(\theta,\phi)$ around the μ-th atom.

$$\phi_{AO}^{\mu,n,l,m} = R_{\mu,n,l}(r-R_\mu)\,P_l^m(\hat{\theta},\hat{\phi}) \qquad 11$$

where R_μ stands for the position of u-th atom.
The radial wavefunction R(r) satisfies the Schoedinger equation around the μ th atom.

$$\left[-\frac{1}{r^2}\frac{\partial}{\partial r}r^2\frac{\partial}{\partial r} + 2u(r) + \frac{l(l+1)}{r^2}\right]R_{\mu,n,l} = \varepsilon_{\mu,n,l}\,R_{\mu,n,l} \qquad 12$$

The ordinary variation method leads the secular equation for the coefficients C in eq. 9 with the Hamiltonian and overlap matrices H_{ij} and S_{ij}

$$HC = \varepsilon SC$$

$$H_{ij} = \langle u_i | H | u_j \rangle , \quad S_{ij} = \langle u_i | u_j \rangle \qquad 13$$

Discrete Variational integration replaces the 3-dimensional integration by the weighted sum of the integrand at random sample point r_k. For example, H_{ij} is replaced with

$$H_{ij} = \sum_k D(r_k)\, u_i(r_k)\, H(r_k)\, u_j(r_k) \qquad 14$$

where $D(r_k)$ is the weight at r_k.

The distribution of sample point around each atomic core is taken to be Fermi-like function because the most radial wavefunctions oscillate near nuclei and damps smooth at infinite. With regard to the effectiveness of this integration method, consult the references 3.

$$1/D(r) \propto \frac{1}{1 + \exp(\beta r - R_0)} \qquad 15$$

The self-consistency of the calculation can be achieved by repeating the computation till the initial and obtained charge distribution come to be the same.

$ Charge Transfer Matrix Elements.

In the frame work of one electron Perturbed Stationary Stated (PSS) method, we find the solution of time-dependent Schroedinger equation[4)]

$$i\hbar \frac{\partial}{\partial t} \Psi(r, R, t) = H \Psi(r, R, t) \qquad 16$$

where r and R stand for electron and nuclear coordinates.
Omitting the electron translational factors we assume the solution of eq. 16 is in the form

$$\Psi(r, R, t) = \sum_j a_j(t)\, u_j(r, R)\, e^{-i\int^t \varepsilon_j dt} \qquad 17$$

where u_j satisfied the Schroedinger equation at fixed atomic configuration.

$$H u_j = \varepsilon_j u_j \qquad 18$$

Substituting eq.17 into eq. 16, we get the close coupling equation for the time dependent coefficient a(t).

$$\frac{d}{dt} a_j(t) = \sum_i \langle u_j | \frac{\partial}{\partial t} | u_i \rangle a_i(t) \exp\left[-i\int^t (\varepsilon_i - \varepsilon_j)\, dt\right] \qquad 19$$

Since u(r) depends on time only through the interatomic vector R(t) we can rewrite the matrix elements as

$$\langle u_j | \frac{\partial}{\partial t} | u_i \rangle = \langle u_j | \frac{\partial}{\partial R} | u_i \rangle \frac{dR}{dt} \qquad 20$$

This expression is valid not only for diatomic system but also

This expression is valid not only for diatomic system but also for polyatomic systems. However, we can reduce this expression in simpler form in the case of diatomic case. Since diatomic collision takes place on a collision plane, we can introduce the polar coordinate centered at the center of mass. With radial and rotational matrix elements defined as

$$\langle u_i | \frac{\partial}{\partial R} | u_j \rangle \quad , \quad \langle u_i | i L_y | u_j \rangle \tag{21}$$

the close coupling equation eq.19 is written in the form

$$\frac{d}{dt} a_j = \sum_i \left\{ V_R \langle u_i | \frac{\partial}{\partial R} | u_j \rangle + \frac{vb}{R^2} \langle u_i | i L_y | u_j \rangle \right\} a_i(t) \exp\left[-i \int^t (\varepsilon_i - \varepsilon_j) dt \right] \tag{22}$$

where V_R and b are the radial velocity and impact parameter respectively.
In eq.21 L_y represents the angular momenta

$$L_y = i \left(z \frac{\partial}{\partial x} - x \frac{\partial}{\partial z} \right) \tag{23}$$

and d/dR stands for the derivative respect to interatomic distance R.

As described in the previous section, the DV-Xα method writes the molecular wavefunction u as

$$u = \sum_j C_j \sum_{\mu,n,l,m} W^j_{\mu,n,l,m} \phi_{AO}^{\mu,n,l,m}(r - R_\mu) \tag{24}$$

$$\phi_{AO}^{\mu,n,l,m} = R_{\mu,n,l}(r - R_\mu) P_l^m(\hat{\theta}_\mu, \hat{\phi}_\mu)$$

u(r,R) depends on R through the electron coordinate $r-R_\mu$. Let's apply an operator d/dR to u(r,R).

$$\frac{d}{dR} u(r,R) = \sum_j \frac{dC_j}{dR} i \sum_{\mu,n,l,m} W^j_{\mu,n,l,m} \phi_{AO}^{\mu,n,l,m} + \sum_j C_j \sum_{\mu,n,l,m} W^j_{\mu,n,l,m} \frac{d}{dR} \phi_{AO}^{\mu,n,l,m} \tag{25}$$

The second term in eq. 25 can be calculated putting $s=r-R_u$ and differentiating respect to s.

$$\frac{d}{dR} = \frac{d}{ds} \cdot \frac{ds}{dR_\mu} = -\frac{d}{ds} \tag{26}$$

The atomic basis wavefunction ϕ_{AO} is a product of radial wavefunction R(s) and real spherical harmonics P_l^m. So, we can write

$$\frac{d}{ds} \phi_{AO} = \frac{d}{ds} R(s) P_l^m(\hat{\theta}, \hat{\phi}) + R(s) \frac{d}{ds} P_l^m(\hat{\theta}, \hat{\phi}) \tag{27}$$

The first term in eq 27 can be numerically obtained using cubic

Spline method because we use the numerically solved radial wavefunction. On the contrary the second term can be analytically derived using the expression

$$\frac{d}{ds} P_\ell^m(\theta,\hat{\phi}) = \frac{\partial}{\partial x} P_\ell^m(\theta,\hat{\phi}) \cdot \frac{dx}{ds} + \frac{\partial}{\partial y} P_\ell^m(\theta,\hat{\phi}) \frac{dy}{ds} + \frac{\partial}{\partial z} P_\ell^m(\theta,\hat{\phi}) \frac{\partial z}{\partial s}$$

where x,y, and z are the Cartesian coordinates and satisfy

$$x = \cos\hat{\theta}\cos\hat{\phi}$$
$$y = \cos\hat{\theta}\sin\hat{\phi}$$
$$z = \sin\hat{\theta}$$

Let's turn to the first term in eq.[25] again. dC(R)/dR is the derivative of coefficient with a infinitesimal shift of atomic configuration. We replace this with a finite difference $\{C(R+dr) - C(R)\}/dr$. Though two calculation at R and R+dr may not align the phases of the wavefunctions. So we flip the sign of wavefunction so that the largest component of atomic orbital has the same sign. This works well if dr is less than 2% of R

Phase of coupling matrices depends on that of wavefunction, too. There is no relation between the phase of wavefunction at each mesh point because calculation with fixed atomic configuration is indeed independent each other. To get the smooth coupling matrices, we again flip the sign of matrix elements so that the second derivative of coupling respect to the interatomic distance takes the minimum. This can make the phase of matrices elements consistent for the whole region of the interatomic distance.

$ References

1) for example, see J.C.Slater 'Quantum heory of Atomic Structure' Vol. 2 McGraw Hill , New York 1960

2) W.Kohn and L.Sham Phys.Rev., 140 A1133 (1965)

3) C.B.Haselbrove. Math.COmpt. 15 323 (1961)

4) for example, see M.R.C. McDowell and J.P.Coleman, Introduction to the Theory of Ion-Atom Collisions (North-Holland, Amsterdom (1970)

Charge Transfer Process in Collisions of Highly Charged Ions in Tokamak Plasma

Fumihiro Koike

School of Medicine, Kitasato University,
Kitasato 1-15-1, Sagamihara, Kanagawa 228
Japan

Recent progress of tokamak plasma diagnostics[1] has pointed out that the charge transfer process between highly ionized ions is important as the mechanism of the excited state formation of impurity ions. We decided to examine this point from the view point of atomic physics and to formulate the way of calculating the charge transfer cross sections in such the highly ionized collision systems. As one of the prototype of the collision systems, we took up the system consisting of titanium and oxygen ions; we investigate the following charge transfer process:

$$Ti^{20+}(1s^2) + O^{6+}(1s^12s^1) \rightarrow Ti^{19+}(1s^2n{=}5,l) + O^{7+}(1s^1),$$

here $n = 5$, l indicates that the transferred electron is populating in the excited atomic orbitals with the principal quantum number $n = 5$ and all the possible angular momentum quantum numbers l . We developed the method according to the following strategies.

1). To give useful data for plasma diagnostics, such as the total charge transfer cross sections and the intensity distributions of the charge transferred final states in principal as well as angular momentum quantum numbers.

2). To develop a numerical method which requires only a reasonable amount of the machine time retaining enough accuracy for the purpose of the plasma diagnostics.

To formulate the collision process, we took into account the following characteristic properties of the collision system.

1). The interatomic relative velocity, which lies typically between 0.05 atomic unit and 0.6 atomic unit, is very slow compared with the electronic orbital-velocity, which is typically 5 atomic unit. Therefore, the molecular-orbital method may fit for the description of the electronic state.

2). The de Broglie wave length of the interatomic relative motion is typically in the range between 0.006 a_0 − 0.0005 a_0, and this length is quite short compared with the characteristic length of the interatomic interaction, which is typically 0.1 a_0. Therefore, we may describe the interatomic motion classically, and in this case we will investigate the time-development of the electronic states.

We have adopted the Discrete Variational Xα (DV-Xα) method[2-4] for the calculation of the quasi-molecular electronic states. We have adopted the semiclassical time-dependent coupled-channel equations [5] for describing the collision process. Because the details of the electronic-state calculation is presented by Fujima elsewhere in the present proceedings, we try to concentrate ourselves, in this report, mainly on the description of the dynamics of the collisions.

Now, we take $H_{el}(r;R)$ as the total electronic Hamiltonian, where r and R represent the set of the electronic coordinates and the internuclear distance, respectively. We take $\Psi(r;R)$ as the total electronic wavefunction. Then, the semiclassical time-dependent Schroedinger equation of the system is written as

$$H_{el}(r;R)\Psi(r;R) = i\frac{\partial}{\partial t}\Psi(r;R), \tag{1}$$

where t is the time and i is the imaginary unit. The total wavefunction $\Psi(r;R)$ may be expanded in terms of the basis quasi-molecular electronic wavefunctions $\Phi_i(r;R)$ as

$$\Psi(r;R) = \sum_i c_i \exp\left[-i\int^t \varepsilon_i dt'\right]\Phi_i(r;R), \tag{2}$$

where c_i is the amplitude of the i 'th channel, say, of the i 'th quasi-molecular state, and where ε_i is the electronic energy of the i 'th channel. And $\Phi_i(r;R)$ and ε_i are given by the following stationary-state Schroedinger equations.

$$H_{el}(r;R)\Phi_i(r;R) = \varepsilon_i\Phi_i(r;R). \tag{3}$$

Substituting eqs. (2) and (3) into eq. (1), we obtain the following set of coupled-channel equations.

$$\dot{c}_i = -\sum_{i\neq j} <\Phi_i|\frac{\partial}{\partial t}|\Phi_j> \exp\left[i\int^t \left(\varepsilon_i - \varepsilon_j\right)dt'\right] c_j. \tag{4}$$

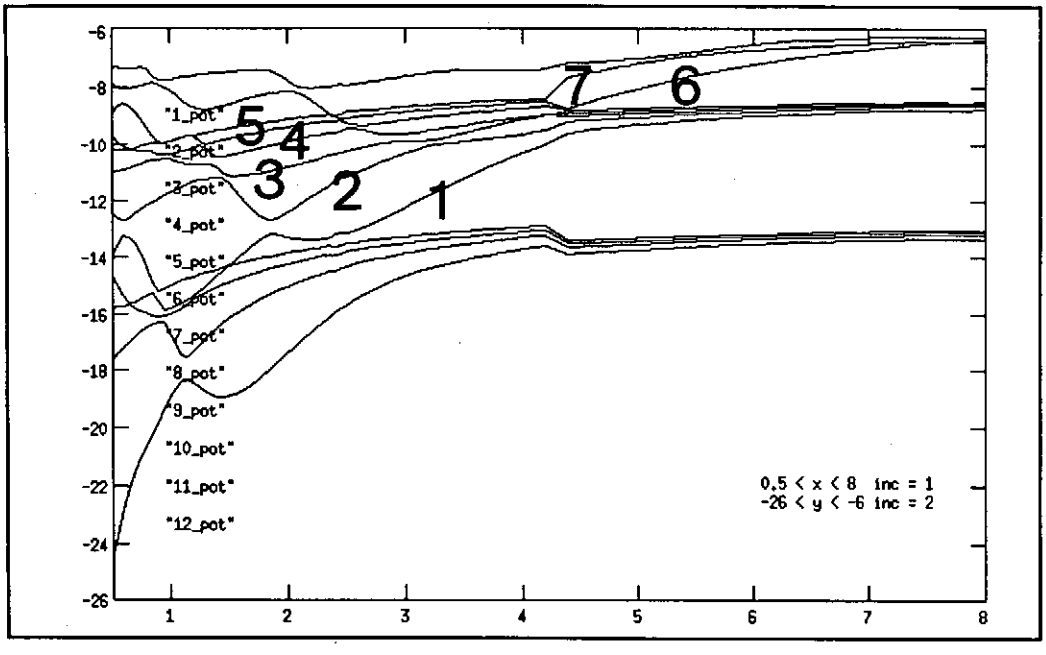

Fig. 1. Quasi-molecular potential energies ε_i in units of Hartree as functions of the internuclear distance R in units of Bohr radius a_0

The numbers from 1 to 7 on the curves indicate the associating channels. The channel number 6 is the initial channel, which is correlating to the state $Ti^{20+}(1s^2) + O^{6+}(1s^12s^1)$ in the separated atom limit. The channel numbers from 1 to 5 are the charge transferred final channels, which are correlating to the states $Ti^{19+}(1s^2n{=}5,l) + O^{7+}(1s^1)$, in the separated atom limit. And the channels 1, 2, 3, 4, and 5 correspond to the states with l = 4, 3, 2, 1, and 0 ,respectively. The channel 7 is a direct excitation channel, which is correlating to the state $Ti^{20+}(1s^2) + O^{6+}(1s^12p^1)$ in the separated atom limit.

We solve this set of equation under an appropriate initial condition for the set of c_i. The probability $P_i(b)$ of finding the system in the state $\Phi_i(r;R)$ after the collision is given for a specified impact parameter b by

$$P_i(b) = |c_i(\infty)|^2. \tag{5}$$

The total scattering cross section for the specified channel i is given by

$$\sigma_i = \int_0^\infty 2\pi b P_i(b)\mathrm{d}b. \tag{6}$$

To solve eq. (4), we need to evaluate the dynamical coupling matrix elements $<\Phi_i|\frac{\partial}{\partial t}|\Phi_j>$. Because we are now considering slow collisions and the charge transfer is considered as to take place at fairly large internuclear distances, we, firstly, neglect the rotational couplings between the quasi-molecular states, and we, secondly, neglect the effect of the so called Electron Translation Factor (ETF). Then we need only to evaluate the following radial coupling matrix elements.

$$<\Phi_i|\frac{\partial}{\partial t}|\Phi_j> = v_R<\Phi_i|\frac{\partial}{\partial R}|\Phi_j>, \tag{7}$$

where $v_R = \frac{dR}{dt}$ is the radial collision velocity.

In Fig. 1, we show the quasi-molecular potential energies ε_i as functions of the internuclear distance R , which are obtained by solving eq. (3) by means of the DV-Xα method. Although the DV-Xα calculation has been carried out on the 23-quasi-molecular states in total, we have shown in this figure only the 12-states that are included into the dynamics calculation. But in the present prototype calculation, we included only 7-channels. They are indicated by channel numbers from 1 to 7 in this figure. The channel $i = 6$, which is indicated as 6 in Fig. 1 and is correlating to the state $Ti^{20+}(1s^2) + O^{6+}(1s^12s^1)$ in the separated atom limit, is the initial channel for the present charge transfer processes. The energy curve of the channel 6 undergoes avoided crossings at around $R = 5a_0$ with a bunch of the energy curves which are of the channels correlating to the states $Ti^{19+}(1s^2n{=}5,l) + O^{7+}(1s^1)$. The charge transfer reaction can be interpreted as to take place mainly in this curve-crossing region.

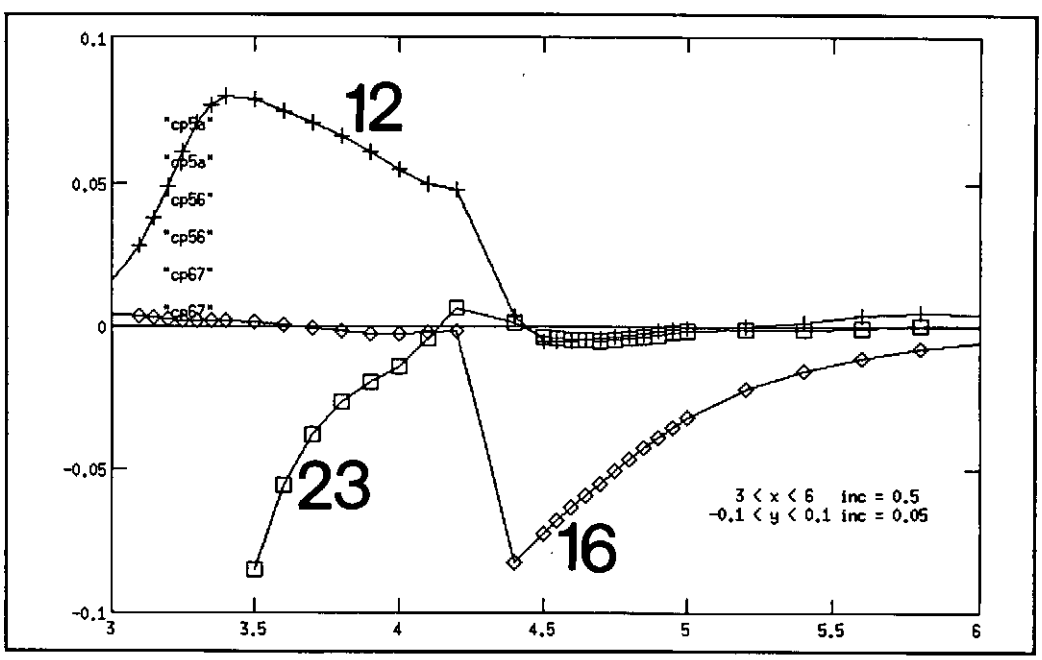

Fig. 2. Examples of the radial couplings at around the crossing radius $R = 5a_0$
Horizontal axis: internuclear distance R in units of Bohr radius a_0 . Vertical axis : coupling matrix elements $<\Phi_i|\frac{\partial}{\partial R}|\Phi_j>$ in atomic unit. The combinations of two digits on the curves indicate the pairs of coupled channels.

In solving the coupled-channel equations (4), we have taken into account all the radial coupling matrix elements which are realized by possible combinations of the channels; we do not make any a priori choice of the couplings according to their magnitudes or to their importance to the transitions for the current interests. This is only the way which can avoid introducing any unexpected truncation errors into the result of calculation. In Fig. 2, we show several examples of the radial couplings at around the

crossing radius $R = 5a_0$. We can see that the initial channel 6 couples primarily with the channel 1, which is correlating to the charge transferred state with angular momentum quantum number $l = 4$.

In Fig. 3, we show the cross sections for the charge transfer into the various angular momentum states $Ti^{19+}(1s^2n = 5, l = 0, 1, 2, 3, 4)$. We find in this figure that the cross sections have a sharp threshold at about 1.0keV of the collision energy. This threshold energy is determined mainly by the strength of the Coulomb potential between the colliding ions; below 1.0keV the collision system can not access the potential-curve crossing region at around $R = 5a_0$ due to the Coulomb repulsion.

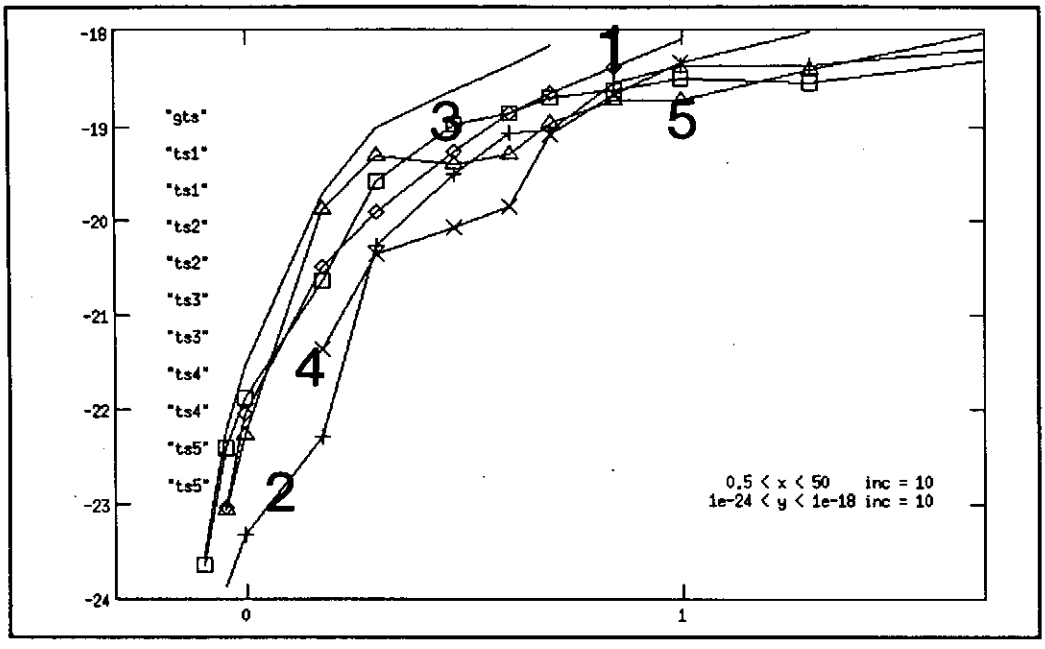

Fig. 3. The cross sections for the charge transfer into the various angular momentum states $Ti^{19+}(1s^2n = 5, l = 0, 1, 2, 3, 4)$.
Horizontal axis: collision energy E in units of log(keV) . Vertical axis : cross sections σ_i in units of log(cm^2). The numbers on the curves indicate the associating channels. The solid line with no symbols represents the total charge transfer cross sections.

We are now in the course of the extension of the numerical calculations changing the collision systems. The result will be seen elsewhere in forthcoming reports.

References

1. T. Kato , S. Morita, K. Masai, and S. Hayakawa, *Phys. Rev.*, vol. A36, p. 795, 1987.
2. H. Adachi , M. Tsukada, and C. Satoko, *J. Phys. Soc. Jpn.*, vol. 40, p. 875, 1976.
3. A. Rosen , *Chem. Phys.*, vol. 65, p. 3085, 1976.
4. K. Fujima , T. Watanabe, and H. Adachi, *Phys. Rev.*, vol. A32, p. 3585, 1985.
5. F. Koike , H. Nakamura, S. Hara, Y. Ichikawa, M. Matsuzawa, H. Sato, and I. Shimamura, *J. Phys.*, vol. B11, p. 4193, 1978.

Collision processes involving doubly excited states of He and H^-

Michio Matsuzawa
Department of Applied Physics and Chemistry
The University of Electro-Communications,
1-5-1, Chofu-shi, Tokyo, Japan 182

Here we report our theoretical studies on collisional behaviors of He atoms and H^- ions in strongly correlated doubly excited states in order to understand correlation effects in collision dynamics. Therefore we focus our studies mainly on the intrashell doubly excited states, in which electron correlation plays a decisive role.

We have calculated the energy levels and the wavefunctions of the doubly excited states of He and H^-/1, 2, 3/ using the hyperspherical coordinate approach. This approach enables us to take the correlation effects fully into account. We have investigated excitation of He by charged-particle impact such as e and C^{6+}/4, 5, 6/, excitation of He and H^- by neutal-particle impact such as Ar /7, 8, 9/ and double photoexcitation of H^-/10/. We look for some systematic trends, i.e. propensity rules in these collision processes to understand how an atom(or ion) in the strongly correlated doubly excited states behaves when interacts with other particles perturbatively.

To interpret the results obtained, we employed the classification scheme of the doubly excited states, ie, $[N(K,T)^{A}n]^{2S+1}L^{\pi}$ proposed by Lin/11/ and rely on the rovibrator model by Kellman and Herrick /12/, in which He is viewed as a floppy "$e\text{-}He^{++}\text{-}e$" linear triatomic molecule. Here N(n) is a principal quantum number

of an inner(outer) electron, K and T are the so called angular correlation quantum numbers, while A is the radial correlation quantum number. It is convenient for understanding of the character of the excitation processes studied here to introduce the vibrational quantum number v(=N-K-1) of doubly degenerate bending modes of the "floppy linear triatomic molecule", and the radial bending quantum number n_θ[=(v-T)/2]. The latter is the number of the nodes of bending vibrational wavefunctions on the body-fixed frame.

In the following, we mainly discuss electron-impact excitation processes of He in the doubly excited states/1, 2, 3/. We have evaluated the Born cross sections for excitation processes between the doubly excited states with L<2 using the hyperspherical wave-functions .

We have found some systematic trends in these collision processes, ie, a set of propensity rules , namely, a radial propensity rule

$$\Delta A=0 \qquad (1)$$

and angular propensity rules,

$$\Delta v=0, \quad \text{and} \quad \Delta T=0 \qquad (2)$$

The latter rules lead to the following one,

$$\Delta n_\theta=0 \qquad (3)$$

These rules indicate that a He atom in the stronly correlated doubly excited states tends to conserve their internal states as the "floppy linear triatomic molecule" during the excitation processes. This can be interpreted as a result of isomorphism of the surface density plot of the squared hyperspherical channel functions between the initial and final states/5/.

For the singlet-singlet optically allowed transitions with $|\Delta L|=1$, the radial propensity rule (1) is incompatible with

the angular propensity rules (2) because two atomic electrons obey Fermi statistics. In other words, this arises from the Pauli exclusion principle for two atomic electrons. For the initial states with A=+, the radial propensity rule dominates over the angular ones and the latter are modified into the following ones,

$$\Delta v=1 \text{ and } \Delta T=1 \qquad (2a)$$

However, n_2 tends to be conserved. Here it should be noted that the ground $^1S^e$ states have only A=+. On the other hands, for the initial states with A=-, the angular propensity rules (2) prevail over the radial propensity rule (1). The latter is changed into the following propensity rule;

$$\Delta A \neq 0 \qquad (1a)$$

A set of propensity rules, (1), (2a) and (3) applies to double photoexcitation of He in photoabsorption of He as is expected /2/. This also applies to double photoexcitation of H^- as is observed in the photodetachment of H^-/10/.

For Ar-impact excitation of He and H^-, one sees similar trends though there are some difference in the propensity rules. Furthermore, the selectivities becomes weaker for neutral-particle impact /7, 8, 9/. This is considered to be due to the short rangeness of He, H^- and Ar interaction.

In conclusion, we have theoretically found that the He and H^- in strongly correlated doubly excited states tend to conserve their internal states as the "floppy linear triatomic molecule" during the excitation processes between the doubly excited states except for the restrictions arising from the Pauli exclusion principle. We may conjecture that this physically simple statement for collision dynamics for the doubly excited states may be generalized to the multiply excited states if we succeed in finding a language to describe collective motion of atomic

electrons in the multiply excited states of the atoms.

References

1) N. Koyama, H. Fukuda, T. Motoyama and M. Matsuzawa, J. Phys. B19 L331 (1986)

2) H. Fukuda, N. Koyama and M. Matsuzawa, J. Phys. B20, 2959(1987)

3) N. Koyama, A. Takafuji and M. Matsuzawa, J. Phys. B22, 553(1989)

4) M. Matsuzawa, T. Motoyama, H..Fukuda and N. Koyama, Phys. Rev. A34, 1793(1986)

5) T. Motoyama, N. Koyama and M. Matsuzawa, Phys. Rev. A38, 670(1988)

6) M. Matauzawa, T. Atsumi and N. Koyama, Phys. Rev. A41, 3596(1990)

7) A. Takafuji, N. Koyama and M. Matsuzawa, Abstracts of Papers 16th ICPEAC, New York, 26 July-1 Aug. 1989, p703

8) N. Koyama, A. Takafuji and M. Matsuzawa, Chinese J. Phys. 27, 323 (1989)

9) M. Maeda, N. Koyama and M. Matsuzawa, Abstracts of Papers, Workshop on Physics of H^-, Albuquerque, 9 -11 Jan. 1990

10) M. Matsuzawa, N. Koyama, M. Maeda and T. Ishihara, Abstracts of Papers, 12th ICAP, Ann Arbor Michigan, 29 July-3 Aug. 1990

11) C. D. Lin, Ad. At. Mol. Phys. 22 , 77, (1983) and references therein

12) a) M. E. Kellman and D. R. Herrick, Phys. Rev. A 22, 1536. (1980)
b) D. R. Herrick, Ad. Chem. Phys. 52, 1, (1983) and references therein.

ELECTRON SPECTRA FROM DOUBLY EXCITED CHARGED IONS

Y. Kanai, H. A. Sakaue*, K. Ohta*, M. Kushima*, T. Inaba**, S. Ohtani+,**, K. Wakiya*, H. Suzuki*, T. Takayanagi*, T. Kambara, A. Danjo#, M. Yoshino$, and Y. Awaya

The Institute of Physical and Chemical Research (RIKEN), Wako, Saitama 351-01 Japan

INTRODUCTION

Recently multi-electron transfer processes in slow highly-charged ion-atom collisions have been studied by energy gain spectroscopy[1-3], ejected electron spectroscopy[4-10], and x-ray spectroscopy[11,12]. Those studies are being done for the following two purposes; (1) to study the atomic structure of highly charged ions, (2) to investigate the mechanism of the multi-electron transfer processes in the highly-charged ion-atom collisions. In the double electron transfer into bear nucleus projectiles by collisions with the single target atoms such as He and H_2, only the singlet states of the doubly excited configurations can be produced unless the collision has changed an electron spin[13]. When the doubly excited states produced in such collisions are the (2lnl') configuration, a possible final state after ejecting one electron should be the 1s state of H-like

---

Present address
* Department of Physics, Sophia University, Chiyoda-ku, Tokyo 102 Japan
** Institute for Laser Science, University of Electro-Communications, Chofu, Tokyo 182,Japan
+ National Institute for Fusion Science, Nagoya 464-01, Japan
# Department of Physics, Niigata University, Niigata 950-21, Japan
$ Laboratory of Physics, Shibaura Institute of Technology, Omiya, Saitama 330, Japan

ions. Therefore, in these collision systems, the electron spectra should be simple enough to analyze easily. Here we report the spectroscopic studies of ejected electrons from autoionizing state of doubly-excited He-like ions[14].

EXPERIMENT AND RESULTS

We measured ejected electrons produced by the following double-electron transfer collisions;

$$67\ \text{keV}\quad C^{6+} + He(1s^2) \longrightarrow C^{4+}(2lnl')^1L + He^{2+} \qquad (1)$$
$$\qquad\qquad\qquad\qquad\qquad\qquad\qquad\qquad\qquad\qquad \big\downarrow \longrightarrow C^{5+}(1s) + e^-$$

$$50\ \text{keV}\quad B^{5+} + He(1s^2) \longrightarrow B^{3+}(2lnl')^1L + He^{2+} \qquad (2)$$
$$\qquad\qquad\qquad\qquad\qquad\qquad\qquad\qquad\qquad\qquad \big\downarrow \longrightarrow B^{4+}(1s) + e^- \ .$$

The bare projectiles were produced by the ECRIS(Electron Cyclotron Resonance Ion Source) which was constructed as an ion source for RIKEN AVF cyclotron[15]. Ejected electrons were measured by the technique of the zero-degree electron spectroscopy. Experimental procedure will be published elsewhere[16].

(1) *C^{6+} on He system*

Spectra observed for the collisions of the $^{13}C^{6+}$ with He are shown in figure 1. The energy scale of the spectra was calibrated by using Auger peaks from the $1s2s2p(^2P)$ and $1s2s(^3S)3d(^2D)$ states of Li-like carbon ions which were produced by double collisions with target He atoms at high target pressure of 3×10^{-3} Torr(figure 1b). The energy values of these Auger lines from Li-like carbon ions were determined by Mann[17]. The measured spectrum at a low gas pressure(3×10^{-4} Torr), which is considered as a single collision condition, is shown in figure 1a.

There are two features of the spectrum shown in figure 1a: (1) no peaks of the 2l2l' configurations(around 270 eV) and (2)

peaks of 2lnl' configurations in a wide range of n($\geq$3) are observed. These features can be explained in terms of a "reaction window". From the estimation of the reaction window[18], the crossing radius R_c to produce the 2121' states in the double-electron transfer collisions is estimated to be outside the reaction window under our experimental conditions.

High resolution spectra of ejected electron from 2131' states are shown in figure 2. By comparing theoretical calculations[19-22] with observed spectra, we identify each peak as denoted by vertical lines in the figure. Experimental energy values of ejected electrons from C^{4+}(2131') are listed in Table 1 together with the theoretical ones[19-22,28]. The determination of the energy for 2p3d $^1D^o$ has large uncertainty($\pm$ 0.5 eV) because the ejected electrons from this state do not show a clear peak. In Table 1, the term representations(K, T, and A) with the correlated classification scheme are shown as well as the single-particle notations. Theoretical values noted as Lipsky are extrapolated values from those of Lipsky et al[19] by using a method described by Lin [23]. Observed peak positions in the energy spectra are shifted due to the PCI effect. The PCI shift is given by Mack et al[9],

$$E = - Q[1-V/|V-v_o|]/2V\tau , \qquad (3)$$

where Q is the charge of the PCI-inducing collision partner, V the projectile velocity, v_o the ejected electron velocity and τ the life time of the decaying state.

Energy values of PCI shift using the theoretical life time[24] are also listed in Table 1. Experimental values of ejected electron energies from the 2131' states(^1S, ^1P) are in good agreement with theoretical values of Ho[20] and Safronova[28] after the PCI correction.

(2) *B^{5+} on He system*

Spectra observed for the collisions of the $^{11}B^{5+}$ with He are

shown in figure 3. The measured spectra at a low gas pressure(3 x 10-4 Torr) and at high gas pressure(3 x 10-3 Torr) are shown in figure 3b and 3a, respectively. In this system, we observed the ejected electrons from the 2121' states. This is consistent with the calculated "reaction window"[18].

High resolution spectra of ejected electrons from 2121' and 2131' are shown in figure 4 and 5, respectively. We identify each peak as denoted by vertical lines in the figures. Precise analysis is in progress now.

DISCUSSION

Total angular momentum L-distributions in the double electron transfer processes have been discussed for O^{6+}(3131'), N^{5+}(3131')[8], C^{4+}(3131')[9], and $O^{4+}(1s^2 2pnl)$ n=6,7 [25]. Those previous studies suggest that high-angular momentum states are dominantly populated by double-capture collisions of highly charged ions. In the present observations, most of the ejected electrons(about 80 %) come from D and F states rather than S and P, as shown in figure 2 and 5. If we assume that all of the magnetic sublevels m_L are equally populated, differential cross sections for electron emission in the forward direction will be proportional to the total emission cross sections for the respective L-states. Under this assumption, we could conclude that high L-states are dominantly populated in the present collision systems for C^{6+} + He at 67 keV and B^{5+} + He at 50 keV. At the present, however, since we have no accurate information on the m_L population[26], systematic observation of spectral behaviors as a function of ejection angles are needed[27].

ACKNOWLEDGEMENT

We acknowledge Dr. K. Hatanaka and Mr. H. Nonaka for managing the ECR ion source.

REFERENCES

[1] S.Tsurubuchi et al., J. Phys. **B15**, L733(1982).

[2] H. Cederquist et al., J. Phys. **B18**, 3951(1985).

[3] M. Barat et al., J. Phys. **B20**,5771(1987).

[4] A. Bordenave-Montesquieu et al., J. Phys. **B17**, L127(1984).

[5] N. Stolterfoht et al., Phys. Rev. Lett. **57**, 74(1986).

[6] R. Mann and h. Schultz, Z. Phys. **D4**,343(1987).

[7] P.Benoit-Cattin et al., J. Phys. **B22**,271(1989).

[8] P. Moretto-Capelle et al., J. Phys. **B22**,271(1989).

[9] M. Mack et al., Phys. rev. **A39**, 3846(1989).

[10] R. Hutton et al., Phys. Rev. **A39**,4902(1989).

[11] M. F. Politis et al., J. Phys. **B20**, 2267(1987).

[12] D. Vernhet et al., J. Phys. **B21**,3949(1988).

[13] M. Mack, Nucl. Instrum. Methods **B23**, 74(1987).

[14] H. A. Sakaue et al., Abstracts of 16th ICPEAC(New York), 570 (1989).

[15] K. Hatanaka and H. Nonaka, J. Physique, **C1**, 827(1989).

[16] H. A. Sakaue et al., to be published in J. Phys. **B** (1990).

[17] R. Mann, Phys. Rev. **A35**, 4988(1987).

[18] A. Niehaus, J. Phys. **B19**, 2925(1986).

[19] L. Lipsky et al., Atom. Data & Nucl. Data Tables **20**, 127(1977).

[20] Y. K. Ho, Phys. Rev. **A23**, 2137(1981).

[21] E. Holøien and J. Midtdal, J. Phys. **B4**, 1243(1971).

[22] H. Doyle et al., Phys. Rev. **A5**, 26(1972).

[23] C. D. Lin, Phys. Rev. **A39**, 4355(1989).

[24] U. I. Safronova, Physca Scripta, **T26**, 59(1989).

[25] F. W. Meyer et al., Phys. Rev. Lett. **60**, 1821(1988).

[26] Z. Chen and C. D. Lin calculated the double electron capture cross section of our system. Their results are in agreement with our results, if we posturate that only m_L=0 sublevel are cupied.

[27] S. M. Shafroth, private communication(1990).

[28] U. I. Safronova, private communication(1990).

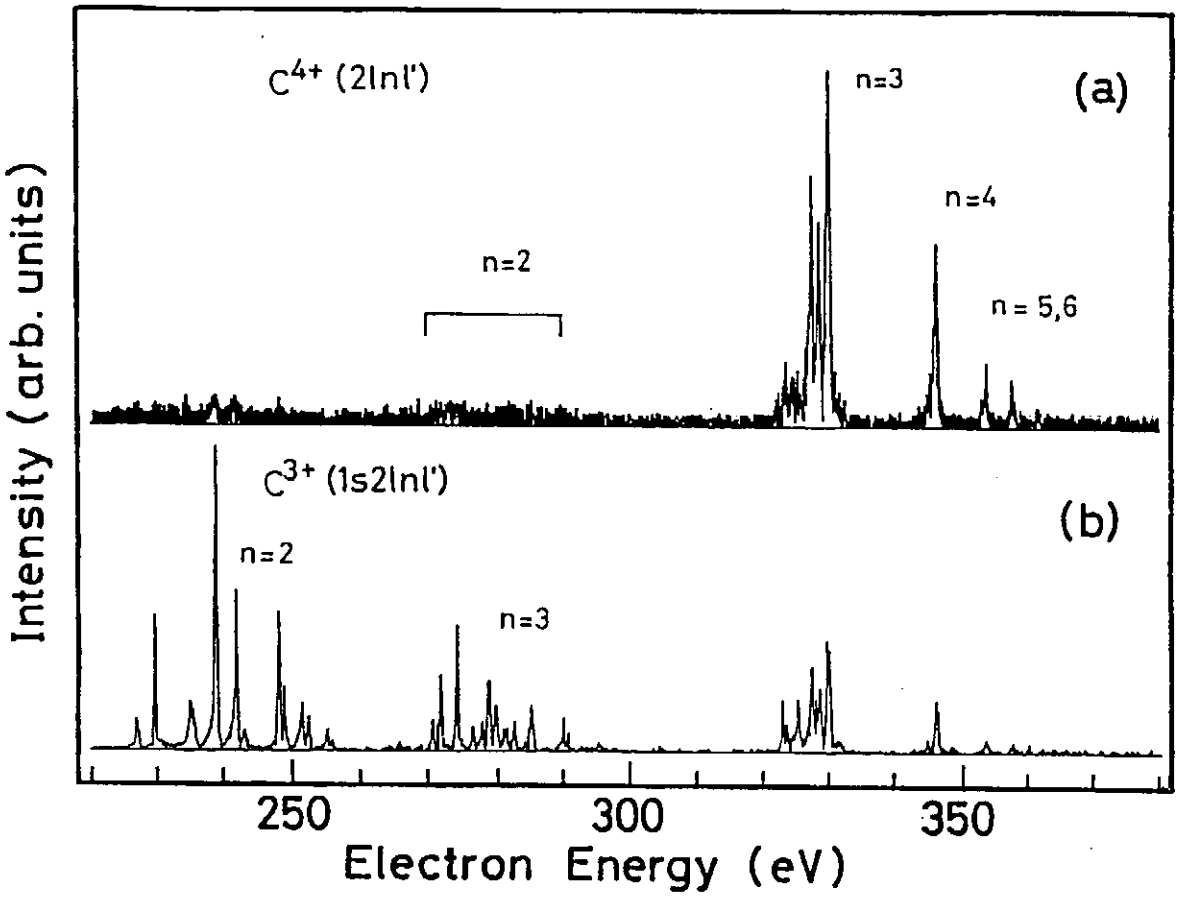

Figure 1 Ejected electron spectra produced by the collision of C^{6+} with He atoms. (a) Spectra from $C^{4+}(2lnl')$ $n \geq 3$ configuration, obtained under the single collision condition. (b) Spectra obtained at the high target pressure. Auger peaks from the $C^{3+}(1s2lnl')$ $n \geq 2$ states are observed as well as the peaks from the $C^{4+}(2lnl')$.

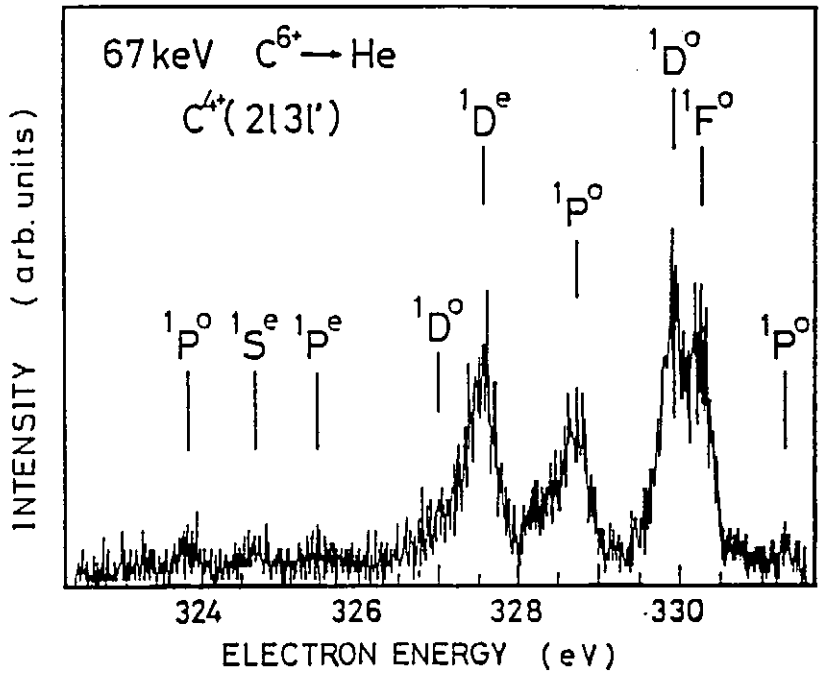

Figure 2 High resolution ejected electron spectrum from the 2131' configuration of C^{4+}.

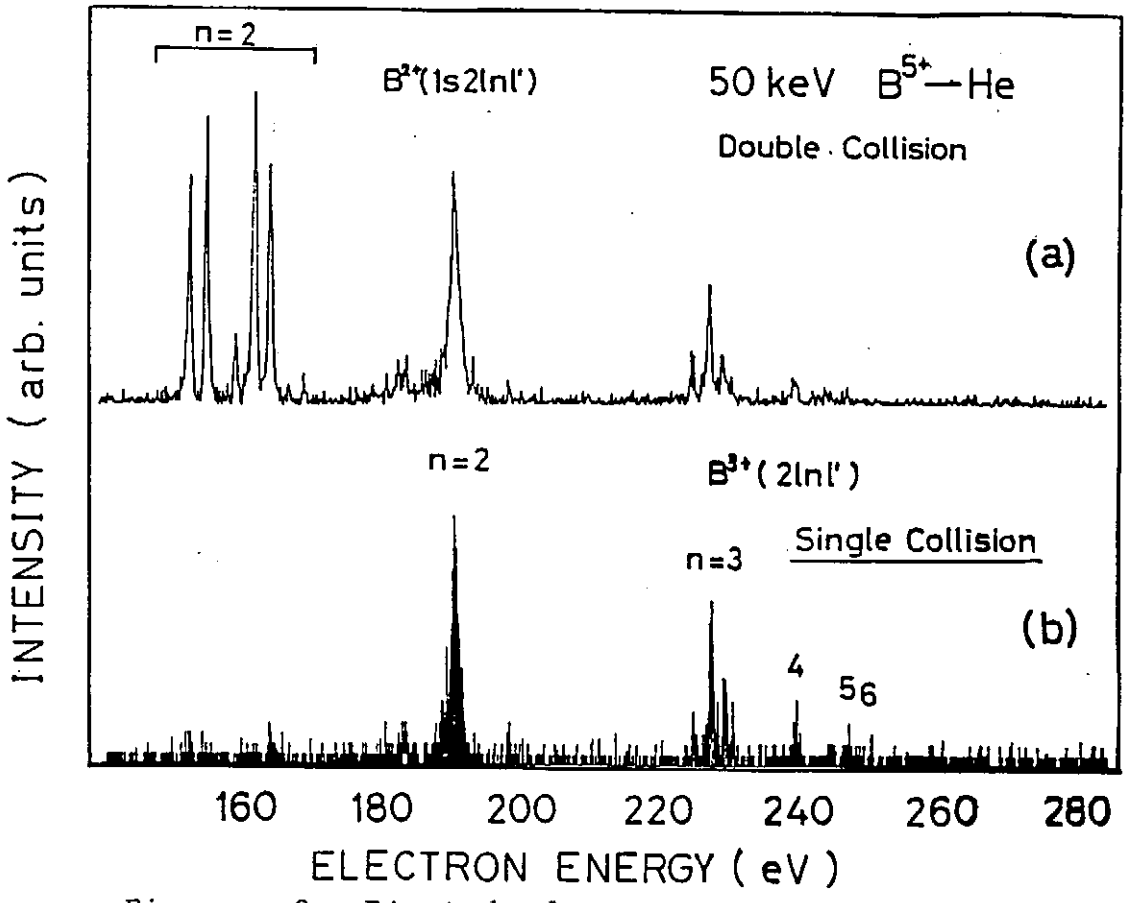

Figure 3 Ejected electron spectra produced by the collision of B^{5+} ions with He atoms. (a) Spectra obtained at the high target pressure. Auger peaks from the $B^{2+}(1s2lnl')$ $n\geq 2$ states are observed as well as the peaks from the $B^{3+}(2lnl')$ states. (b) Spectra from $B^{4+}(2lnl')$ $n\geq 2$ configuration, obtained under the single collision condition.

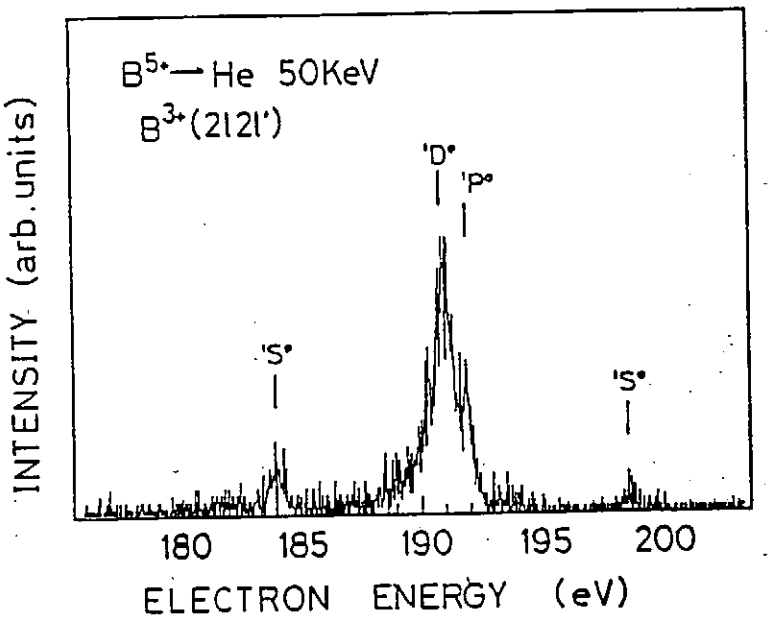

Figure 4 High resolution ejected electron spectrum from the 2121' configuration of B^{3+}.

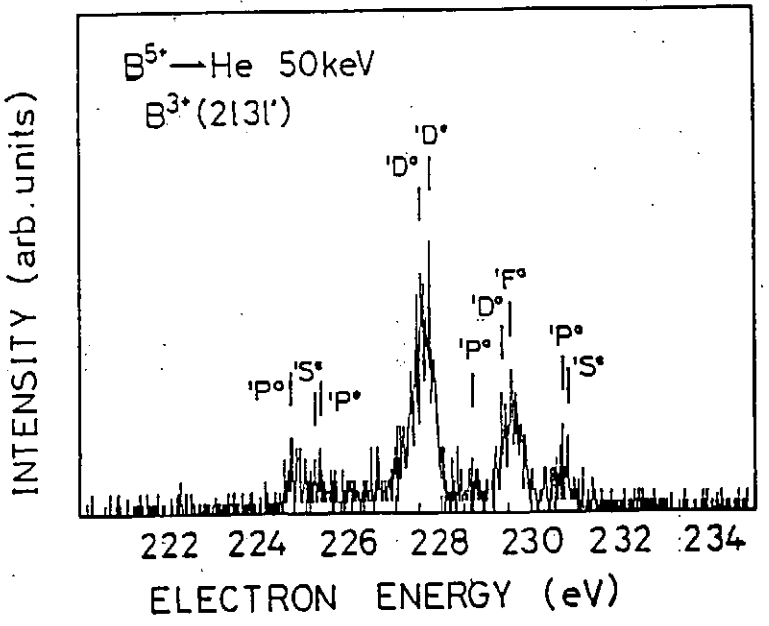

Figure 5 High resolution ejected electron spectrum from the 2131' configuration of B^{3+}.

Table 1 Energy of electron from the $C^{4+}(2131')$.

Observed values (eV)	PCI shift (eV)	Single particle nortation	$^{2S+1}L^{\pi}$	$(K,T)^{A}$	Theory				
					Lipsky [19]	Safronova [28]	Ho [20]	Holøien [21]	Doyle [22]
323.7 ± 0.2	0.0	2p3s	$^{1}P^{o}$	$(1,0)^{-}$	323.91	323.82	323.88		
324.7 ± 0.2	0.2	2s3s	$^{1}S^{e}$	$(1,0)^{+}$	325.16	324.86	324.96		
325.5 ± 0.2	0.0	2p3p	$^{1}P^{e}$	$(0,1)^{-}$	325.71	325.64		325.65	325.65
327.0 ± 0.5	0.0	2p3d	$^{1}D^{o}$	$(0,1)^{0}$	327.56	327.83			327.48
327.5 ± 0.2	0.2	2p3p	$^{1}D^{e}$	$(1,0)^{+}$	328.17	327.88			
328.7 ± 0.2	0.1	2s3p	$^{1}P^{o}$	$(0,1)^{+}$	329.41	328.78	328.90		
329.9 ± 0.2	0.0	2p3d	$^{1}D^{e}$	$(0,1)^{0}$	330.34	330.06			
330.2 ± 0.2	0.0	2p3d	$^{1}F^{o}$	$(1,0)^{0}$	330.71	330.16			
331.2 ± 0.2	0.0	2p3d	$^{1}P^{o}$	$(-1,0)^{0}$	331.70	331.16	331.36		

RESONANCE STATES OF MUONIC MOLECULES AND MUON-CATALYZED FUSION

Isao Shimamura
RIKEN, Hirosawa, Wako, Saitama 351-01, Japan

The d-t and d-d fusion catalyzed by muons without the need of high-temperature plasmas has been the subject of increasing experimental and theoretical interest particularly in these years. It has been established experimentally that a single muon can catalyze d-t fusion about 150 times on the average during its lifetime in a dense mixture of deuterium and tritium under certain conditions.[1-5] In the pure deuterium without tritium less efficient muon-catalyzed d-d fusion occurs.

The clue to the mechanism of the catalysis is the formation of muonic molecular ions $(dt\mu)^+$ or $(dd\mu)^+$,[1,6,7] which are essentially Coulomb three-body systems similar to the hydrogen molecular ions H_2^+, D_2^+, HD^+, etc. The equilibrium internuclear distances R_e of the muonic molecules are smaller than the R_e of the electronic molecules by a factor of about 207. This greatly reduces the Coulomb barrier against nuclear fusion in muonic molecules compared with the barrier for electronic molecules, thus enhancing the intramolecular fusion rate by, for example, ninety-five orders of magnitude in going from DT^+ to $(dt\mu)^+$.[8]

The high intramolecular fusion rates have stimulated extensive theoretical and computational studies of bound states of muonic molecules.[7,9-12] Particular attention has been paid to weakly bound states, since they are considered to be formed efficiently in thermal collisions

$$d + t\mu \rightarrow (dt\mu)^+ + \Delta E \quad \text{or} \quad d + d\mu \rightarrow (dd\mu)^+ + \Delta E \qquad (1)$$

between a deuteron in a deuterium and a $t\mu$ (or $d\mu$) atom in the ground state. This is because the excess energy ΔE is small for weakly bound states of the muonic molecule, and is efficiently absorbed by the vibrational-rotational motion of a hydrogenlike electronic molecule $d^+(dt\mu)^+e^-e^-$ [or $d^+(dd\mu)^+e^-e^-$], in which the

muonic molecular ion $(dt\mu)^+$ [or $(dd\mu)^+$] has a much smaller size than the electron orbitals and plays a role of a "pseudo-nucleus" in the electronic molecule.

Most $d\mu$ atoms and many of the $t\mu$ atoms are formed initially in highly excited states and are then deexcited down to lower and lower states. In a D_2-T_2 mixture, $t\mu$ atoms in the lower states are formed also in the muon-transfer processes $t + d\mu \rightarrow d + t\mu$, which appear to occur with a higher rate for excited states than for the ground state.[13] Therefore, many $t\mu$ and $d\mu$ atoms are expected to be in the metastable 2s state for quite a long time. An interesting question to be posed, then, is whether processes (1) may occur with a high rate when the $t\mu$ (or $d\mu$) atom is in the 2s or 2p state. If they do, they may play an important role in the muon-catalyzed fusion. Especially, they may play a role as intermediate resonance states in the muon-transfer processes that determine the population densities of different states of muonic atoms.

For processes (1) with $t\mu(n=2)$ or $d\mu(n=2)$ to occur appreciably the ex cess energy ΔE must be small enough to be transferred efficiently to some degrees of freedom of motion, such as the vibrational-rotational motion of an electronic molecule, just as in processes (1) with atoms in the ground state. In other words the $(dt\mu)^+$ or $(dd\mu)^+$ molecule must have a level or levels lying considerably close to the dissociation limit $d + t\mu(n=2)$ or $d + d\mu(n=2)$. Such levels are autodissociating or resonance states, because they are embedded in the continuum above the dissociation limit $d + t\mu(n=1)$ or $d + d\mu(n=1)$.

The purpose of this paper is to study the possibility of existence of resonance states of three-body muonic molecules that might be relevant to muon-catalyzed fusion. Resonance states of the $(dt\mu)^+$ molecule are studied also in Ref.14, but they are reported to lie at several eV above the $d\mu(n=1)$ threshold, i.e., far below the $t\mu(n=2)$ threshold, and appear to be formed by a mechanism different from that discussed in this paper.

The region of the configuration space that is most crucial to the present arguments is the asymptotic region where particle 3 with positive charge +e and mass M_3 lies far from the atom con-

sisting of particle 1 with charge +e and mass M_1 and particle 2 with charge -e and mass M_2. We define a set of Jacobi coordinates (r,R), r being the position vector of particle 2 relative to particle 1, and R being that of particle 3 relative to the center of mass of the atom (1,2).

Let $J\hbar$ and $M\hbar$ be the total angular momentum and its z component. To describe the angular-part wave function of the three-body system we form eigenfunctions of $(J\hbar)^2$ and $M\hbar$ from spherical harmonics $Y_{lm}(\hat{r})$ and $Y_{l'm'}(\hat{R})$. The space-part wave function may be expanded in terms of these angular functions and the radial wave functions of the atom (1,2).

For energies close to the level n=2 of atom (1,2), the only channels in this expansion that are important in the asymptotic (i.e., large-R) region are those three with n=2.(One of the channels vanishes for J=0, leaving only two important channels.) Substituting this expansion with only these three channels into the Schrödinger equation for the three-body system, projecting this equation onto the angular functions and the atomic radial wave functions, expanding the potential matrix in terms of inverse powers of R, and retaining only the leading term, we obtain three coupled second-order differential equations in which the potential matrix elements are proportional to R^{-2}. This long-range potential is due to the linear Stark effect, and is a result of the degeneracy between the 2s and 2p levels.

These coupled equations may be diagonalized (because the potential matrix may be diagonalized) by a unitary transformation of the channels. This leaves three uncoupled single-channel equations with potentials proportional to R^{-2}. It is easy to prove for low J that the potential in one of these channels is attractive and strong enough to support an infinite number of bound states. For dtμ and ddμ, for example, there are an infinite number of states for all J smaller than and equal to seven.

The wave function of any of these bound states is complicated for small R. For large R for which our three-channel expansion is valid, the wave function is a modified Bessel function of the second kind and of imaginary order, and is easily calculable. An approximation of small binding energy (or high-lying bound state)

leads to a simple formula for the levels E_v measured relative to the n=2 dissociation limit, namely, $E_v=-Aa^v$, where A and a are constants and v is an integer for labeling the bound state. The constant a is calculable in terms of J and M_i only, and is smaller than unity. Thus the infinite number of bound states converge to the n=2 dissociation limit. These bound states change into resonance states due to a weak coupling with the 1s channel. The size of the muonic molecules in these states satisfies a simple formula $\{4\sqrt{|E_v(eV)|}\}^{-1}$ in angstroms. Therefore, the molecules lying within an electron volt from the n=2 dissociation limit are quite large and can no more be regarded as 'pseudo-nucleus.'

Validity of this theory may be tested on the resonance positions available in the literature.[15] Figure 1 proves the validity of the approximate E_v expression. Figure 2 of the wave functions is also instructive.

The highest-lying resonance found in the literature lies at about 1.2 eV below the n=2 threshold. This work has shown that resonances exist at positions within any small energy from the threshold. If the relativistic and QED effects are taken account of, however, the 2s and 2p states split and the number of resonance states becomes finite.

Further details of this work is reported elsewhere.[16]

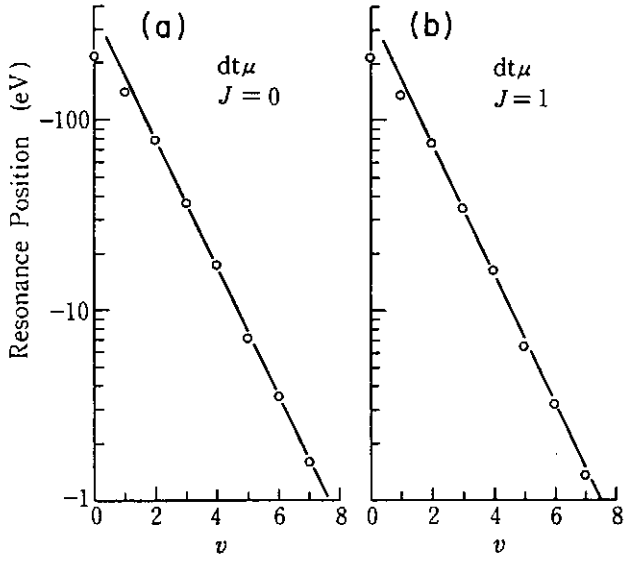

Fig. 1

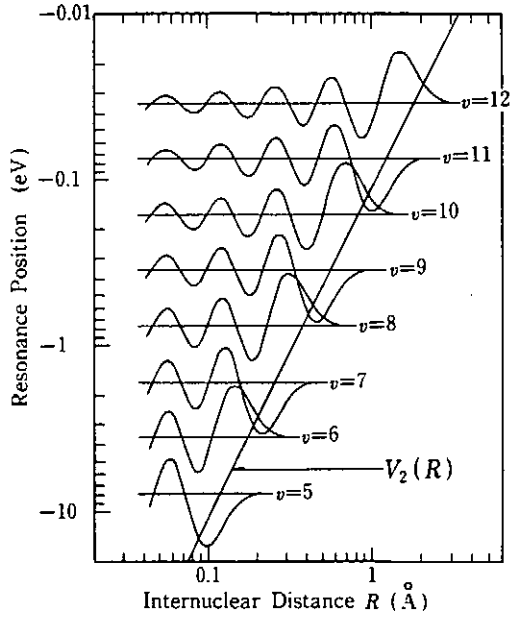

Fig. 2

REFERENCES

1) S.E. Jones, Nature **321**, 127 (1986).
2) S.E. Jones, A.N. Anderson, A.J. Caffrey, J.B. Walter, K.D. Watts, J.N. Bradbury, P.A.M. Gram, M. Leon, H.R. Maltrud, and M.A. Paciotti, Phys. Rev. Lett. **51**, 1757 (1983).
3) W.H. Breunlich, M. Cargnelli, P. Kammel, J. Marton, P. Pawlek, J. Werner, J. Zmeskal, K.M. Crowe, J. Kurck, A. Janett, C. Petitjean, R.H. Sherman, H. Bossy, and W. Neumann, Phys. Rev. Lett. **53**, 1137 (1984).
4) S.E. Jones, A.N. Anderson, A.J. Caffrey, C. DeW. Van Siclen, K.D. Watts, J.N. Bradbury, J.S. Cohen, P.A.M. Gram, M. Leon, H.R. Maltrud, and M.A. Paciotti, Phys. Rev. Lett. **56**, 588 (1986).
5) W.H. Breunlich, M. Cargnelli, P. Kammel, J. Marton, N. Naegele, P. Pawlek, A. Scrinzi, J. Werner, J. Zmeskal, J. Bistirlich, K.M. Crowe, M. Justice, J. Kurck, C. Petitjean, R.H. Sherman, H. Bossy, H. Daniel, F. J. Hartmann, W. Neumann, and G. Schmidt, Phys. Rev. Lett. **58**, 329 (1987).
6) E.A. Vesman, Sov. Phys. J.E.T.P. Lett. **5**, 91 (1967).
7) L.I. Ponomarev, Atomic Physics 10, eds. H. Narumi and I. Shimamura (Elsevier, Amsterdam, 1987), p.197.
8) I. Shimamura, Progr. Theor. Phys. (Kyoto) **82**, 304 (1989).
9) S. Hara, T. Ishihara, and N. Toshima, Muon Catalyzed Fusion **1**, 277 (1987).
10) C.Y. Hu, Phys. Rev. A**36**, 4135, 5420 (1987).
11) M. Kamimura, Phys. Rev. A**38**, 621 (1988).
12) S.E. Haywood, H.J. Monkhorst, and K. Szalewicz, Phys. Rev. A**37**, 3393 (1988); ibid. A**39**, 1634 (1989).
13) L.I. Menshikov and L.I. Ponomarev, Z. Phys. D**2**, 1 (1986).
14) P. Froelich and K. Szalewicz, Muon Catalyzed Fusion **3**, 345 (1988); Phys. Lett. A**129**, 321 (1988).
15) S. Hara and T. Ishihara, Phys. Rev. A**40**, 4232 (1989).
16) I. Shimamura, Phys. Rev. A**40**, 4863 (1989).

Code ATOM for calculation of atomic characteristics.

L.A. Vainshtein

P.N.Lebedev Physical Institute, Moscow, USSR.

1. Introduction.

In applications of atomic physics to the problems of plasma diagnostic it is necessary to know atomic characteristics - energies, transition probabilities et ct. for very many atoms, ions, transitions. Two approaches are possible.

i. Compilation of big data base including experimental data,results of sophisticated calculations that were provided by different authors using different approximations.

ii. Development of general Code for calculation of many types of atomic characteristics based on the general but comparatively simple approximate methods.

The second approach gives of course less accurate data but the errors have the similar origin the quality being useful in applications. The data obtained with such a code can also provide an initial basis for the compilation mentioned above.

The program ATOM is the attempt to use such a general code. The program was developed in Lebedev Physical Institute. In this report I give short description of the methods used, the possibilities and the limitations of the Code.

There are two kinds of data - energies (wave-lengths) and probabilities (cross-sections, rates). They require entirely

different approaches. For probabilities the accuracy of the order of 10% is acceptable in most cases and 1% accuracy is a very good result. For energies the accuracy better then $10^{-4}$is required in most applications. One can not achieve that with any simple method The computer codes exploring such sophisticated methods as multi configuration Hartree(Dirack)-Fock or Z-expansion are available. The last method is used in the MZ-program developed in our laboratory.

Below the atomic units with Ry=0.5au for energy are used. The asymptotic charge of the atomic electron is

$$z = Z - N + 1 \qquad (1.1)$$

where Z is nuclear charge and N is the number of electrons. We use also the designations

$$[J_1 J_2 \ldots] = ((2J+1)\cdot(2J_2+1)\cdot\ldots)^{1/2}$$
$$\delta(J_1 J_2 \ldots, J_1' J_2' \ldots) = \delta(J_1', J_1)\cdot\delta(J_2', J_2)\ldots \qquad (1.2)$$

2. Energies and wave functions of atomic electron.

The Code ATOM does not calculate precise values of energies. The calculation of probabilities and cross-sections is based on one-electron approach. The corresponding wave-functions and energies of the optical (atomic) electron that is responsible for transition are calculated using the semi-empirical method

$$\left[\frac{d^2}{dr^2} - \frac{l(l+1)}{r^2} + \frac{2\zeta(r/\omega)}{r} + \varepsilon\right]\cdot P_{nl}(r) = -2G(r/\omega)/r. \qquad (2.1)$$

Here $U(r)=-\zeta(r/\omega)/r$ - approximate potential with scale factor ω.

Exchange part G/r usually is omitted. The program uses the library of energies ε (experimental values or calculated in other works) in the file A.LIB. If ε for a given state is included in A.LIB scale factor ω is calculated as eigen value of eq.(2.1). If ε is not found in A.LIB it is calculated as eigen value of eq.(2.1).

Eq.(2.1). can not describe the relativistic effects. It means that using the experimental value of ε for large z it is necessary to subtract the relativistic part.

3. Transition characteristics.

The characteristics of the following processes can be calculated by ATOM:

- radiative transitions between discreet levels - f, A;
- radiative ionization and recombination - σ_{ν_i}, σ_{ν_r}, $æ_\nu$;
- collisional excitation and ionization by electron impact - σ, <vσ>;
- collisional excitation and ionization by point heavy particle (Born approximation only) - σ, <vσ>;
- dielectronic recombination - $æ_d$;
- autoionization - W_a;

3.1. Radiative transitions

Radiative characteristics are the simplest for calculation. Oscillator strength for transition a_1-a_2 is equal

$$g_{a1} f(a_1-a_2) = Q(a_1-a_2)\cdot f(12) \qquad (3.1)$$

where Q is the angular factor depending on orbital and spin quan-

tum numbers only, f(12)=f(21) is the "radial part" or (symmetrical) one-electron oscillator strength:

$$f(12) = [l_1 l_2] \begin{Bmatrix} l_1 & l_2 & 1 \\ 0 & 0 & 0 \end{Bmatrix} \int_0^\infty P_1 P_2 r dr \ , \qquad (3.2)$$

Similarly photoionization cross-section

$$\sigma_{\nu i}(a_1) = \sum_{l_2} Q(a_1) \cdot \sigma_\nu(n_1 l_1, E l_2). \qquad (3.3)$$

one-electron cross-section $\sigma_\nu(12)=\sigma_\nu(n_1 l_1, E l_2)$ is expressed similarly (3.2). f(12) and $\sigma_\nu(12)$ are calculated by ATOM using solutions of eq.(2.1) for the orbitals $n_1 l_1 E_1$, $n_2 l_2 E_2$. It is often convenient to use Gaunt-factor G

$$\sigma_\nu(12) = \sigma_\nu^{Cr} \cdot G, \qquad \sigma_\nu^{Cr} = \frac{64/3\sqrt{3} \cdot 137}{\Delta E^{3/2}(1+E/\Delta E)^3} \ . \qquad (3.4)$$

or generalized Gaunt-factor G':

$$G = \frac{1}{(1+X^2)^{lo+1}} \exp\left[\frac{4}{\sqrt{E}}\left(1 - \frac{\mathrm{arctg}X}{X}\right)\right] \cdot [1-\exp(-2\pi/\sqrt{E})]^{-1}$$
$$* \prod_{s=1}^{l_1} \frac{1+(sX/n_o)^2}{1+X^2} \cdot \tilde{G}, \qquad X = (E/\Delta E)^{1/2} \ . \qquad (3.5)$$

They can be obtained from classical asymptotic approximation. G' is also calculated in ATOM.

4. Electron - atom (ion) collisions.

ATOM explore Born (B, for z=1) or Coulomb-Born (CB, for z>1) approximations. In both cases exchange and normalization can be included.

For transition a_1-a_2 cross-section

$$\sigma(a_1-a_2) = \sum_{æ}\left[Q_{æ}(a_1-a_2)\sigma'_{æ}(12) + Q''_{æ}(a_1-a_2)\sigma''_{æ}(12) \right] \qquad (4.1)$$

$$æ = æ_{min}, æ_{min}+2, \ldots æ_{max}: \quad æ_{min}=|l_1-l_2|, \quad æ_{max}=l_1+l_2$$

where $Q_{æ}$, $Q''_{æ}$ are the angular factors, σ' and σ'' are one-electron cross-sections; σ' includes direct and mixed parts, σ'' - exchange part. In B approximation (without exchange) a simple q- representation is possible

$$\sigma^B_{æ}(12) = \frac{8}{k_1^2}\int_{k_1-k_2}^{k_1+k_2} |R^B_{æ}(q)|^2 \frac{dq}{q^3} . \qquad (4.2)$$

$$R^B(q) = [æ l_1 l_2]\begin{pmatrix} l_1 & l_2 & æ \\ 0 & 0 & 0 \end{pmatrix}\cdot\int_0^\infty P_1(r)P_2(r)[j_{æ}(qr)-\delta_{æ0}]rdr$$

CB approximation as well as B with exchange or normalization require more elaborate partial wave representation

$$\sigma'_{æ} = \sum_{\lambda_1\lambda_2}\sigma'_{æ}(\lambda_1\lambda_2), \qquad \sigma''_{æ} = \sum_{\lambda_1\lambda_2}\sigma''_{æ}(\lambda_1\lambda_2) \qquad (4.3)$$

where λ_1 are orbital momentum of the outer electron and partial cross-sections $\sigma_{æ}(\lambda_1\lambda_2)$ are expressed through radial integrals of the type

$$R_{æ} = [l_1 l]\begin{pmatrix} l_1 & l_2 & æ \\ 0 & 0 & 0 \end{pmatrix}[\lambda_1\lambda_2]\begin{pmatrix} \lambda_1 & \lambda_2 & æ \\ 0 & 0 & 0 \end{pmatrix}\int_0^\infty\int_0^\infty F_1F_2P_1P_2\frac{r_<^{æ}}{r_>^{æ+1}}dr_1dr_2 \qquad (4.4)$$

with Coulomb radial functions F(r). Introduction of distorted wave (DW) functions would not give a considerably more complicated program. We however prefer B or CB approach. The physical meaning of DW is the result of a short distance attraction of outer electron to the center of atom. However the distance between optical and outer electrons is not reduced and can even increase do to their

repulsion (polarization of atomic orbitals). Consequently in the vicinity of maximum $\sigma^{DW}>\sigma^{B}$ the last usually being greater then experimental one. Of cause if atom polarization is included as for example in many channel close coupling method the DW basis can be preferable.

4.1. Exchange.

As is well known the Born-Oppenhimer (Op) approximation with permutation of variables in transition amplitude

$$f^{Op} = \langle a_1(1)e_2(2)|r_{12}^{-1}|a_1(2)e_2(1)\rangle \qquad (4.5)$$

overestimate the cross-section more then 10 times. This deficiency is greatly reduced in the close coupling method, however for I order approximation special methods are necessary.

i. Ochkur metod (Och)) keeps only the first term in series $\Sigma a_k/E^k$. This gives for transition amplitude

$$f^{Och} = \frac{q^2}{k^2}\langle 1|e^{i\mathbf{qr}}|2\rangle b(S_1,S_2) \qquad (4.6)$$

i.e. we get q-representation - important advantage of the method. However this approach is applicable only to neutral atoms.

ii. Orthogonaliezed functions method (OF). In Op approximation the total wave-functions of the system are not orthogonal:

$$\langle a_1(1)e_1(2)|a_2(2)e_2(1)\rangle \neq 0$$

because a_i and e_i correspond to asymptotical charge z and z-1. In OF method functions g are used in place of $F_i=|\lambda_i\rangle$:

$$g_1 = F_1-\langle F_1|P_2\rangle P_2\delta(l_2,\lambda_1)$$
$$g_2 = F_2-\langle F_2|P_1\rangle P_1\delta(l_1,\lambda_2), \quad \langle F|P\rangle=\int_0^\infty FPdr \qquad (4.7)$$

This method require partial wave representation. It is applicable both to atoms (z=1) and ions (z>1).

In the code ATOM both methods are present and one can choose Och or OF cross-sections.

4.2. Transitions with ΔS = 0.

Intercombination transitions with change of spin ΔS=1 in LS-coupling are possible only due to exchange. For allowed transitions with ΔS=0 exchange is correction. The total cross-section has the form

$$\sigma(a_1-a_2) \sim f^d(f^d - f^{ex})\delta(S_1,S_2) + (f^{ex})^2 b((S_1,S_2) \qquad (4.8)$$

where f^d, f^{ex} are direct and exchange amplitudes. Two possible cases are illustrated on fig.1. Energy transfers are

$$\delta E^d=\Delta E=E_1-E_2, \qquad \delta E^{ex}=\mathcal{E}+E_2,$$

We see that near the threshold ($\mathcal{E}\approx\Delta E$) if $\Delta E \gg E_2$ (case 1a) $\delta E^{ex}\approx\delta E^d$ and therefore

$$f^d \approx f^{ex}, \quad \sigma \approx b((S_1,S_2)\sigma^B \qquad \text{(case 1a)}$$

For He-like ions, S=0 we have $b={}^1/_4$, $\sigma\ll\sigma^B$. In the case 1b $E_2 \gg \Delta E$, $\delta E^{ex}\gg\delta E^d$. For large energy $\mathcal{E}\gg\Delta E$ also $\delta E^{ex}\gg\delta E^d$. Therefore

$$f^d \gg f^{ex}, \quad \sigma \approx \sigma^d \approx \sigma^B \qquad \text{(case 1b)}$$

We see that for transitions with ΔS=0 exchange may be very important in the vicinity of threshold if $\Delta E \sim E_1 \ll E_2$. On fig.2,3 cross-sections for 1^1S-2^1P transition in He and He-like ion FeXXV are shown.

One can see on fig.2 large disagreement between σ(OF) and σ(Och) near threshold. In this case the orthogonalization (4.7) is

not gives small difference of two large very contributions. On fig.2 the cross-sections without contributions from waves that were orthogonaliezed is also shown. Note that we met such a situation not often in our calculations. On fig.3 we see that contribution of orthogonaliezed waves is small.

4.3. Ionization.

The calculation of ionization cross-section is similar to calculation of excitation cross-section. The main difference is that additional sum over the angular momentum l_2 and energy E_2 of the ejected electron greatly increases a required computer time.

5. Normalization.

he normalization is the part of the general problem of non linear channel interaction. We use the K-matrix method to solve the problem.

In the I order approximation scattering S-matrix is not unitary. We can however calculate in the I order the K-matrix

$$K_{ij} = K_{ij} \sim \langle a_1\lambda_1 k_1 | V_{12} | a_2\lambda_2 k_2 \rangle \qquad (5.1)$$

and calculate S-matrix with matrix relation

$$S = \frac{1 + iK}{1 - iK} , \qquad (5.2)$$

This S-matrix is unitary over the channels included in K-matrix. The general approach is released in the optional program EXIN In the ATOM itself only the normalization in own channel is included. In this approach normalized partial cross-section

$$\sigma^N_{æ}(1\lambda_1,2\lambda_2) = \frac{\sigma^I_{æ}(1\lambda_1,2\lambda_2)}{(1+c\bar{\sigma}^I_{æ}(1\lambda_1,2\lambda_2))^2}$$

$\sigma^I_{æ}\sim|K|^2$ is the I order (without normalization) cross-section $\bar{\sigma}^I_{æ}$ is a slightly modified value. In particular when $V_{12}\to\infty$, $\sigma^I_{æ}\to\infty$, but $\sigma^N_{æ}\to 0$. The close coupling calculations support this result but K-matrix method can overestimate the effect.

6. Dielectronic recombination.

The rate of dielectronic recombination through the level γ

$$X_z(a_0) \to X^{**}_{z-1}(\gamma) \to X^{*}_{z-1}(\gamma') \qquad (6.1)$$
$$\qquad\qquad\qquad\qquad\quad \to X_z(a') + e \qquad \gamma=anlLSJ$$

$$æ^{DR} \sim \sum_{nlLSJ}\sum_{\gamma'} \frac{g_\gamma W_a(\gamma,a_0)\, W_r(\gamma\gamma')}{W_a(\gamma) + W_r(\gamma)} \qquad (6.2)$$

The number of terms in the sum (6.2) is very large and we can't apply usual analytical methods to sum over LSJ because eq.(6.2) is nonlinear.

In ATOM the simplified method is used. We suppose that in the denominator W_r is independent of nlLSJ and replace W_a by averaged value $\bar{W}_a \sim \sigma_{thr}(a_0-a_1)/n^3$, where σ_{thr} is a threshold value of excitation cross-section. The one-channel or 2-3 channels approximations are possible in ATOM.

It worth note that the secondary processes of collisional redistribution over l sub level and ionization are important for final dielectronic rate. However such secondary processes are out of frame of the code ATOM.

Figure cuptions.

Fig.1. Illustrations to excitation process;

1a - direct excitatin, 1b - exchange excitatin.

Fig.2. Excitatin cross-sections for $1^1S - 2^1P$ transition in He.

1 ——— - Born approximation;

2 ------ - Born with excange, CF - method;

3 ····· - the same without contribution of orthogonaliesed waves;

4 -·-·-· - Ochkur method.

Fig.3. The same as on fig.2 for He-like ion Fe XXV.

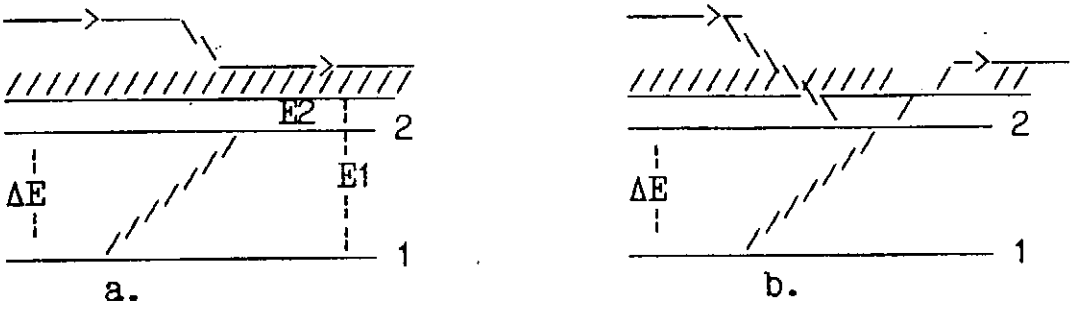

Fig.1

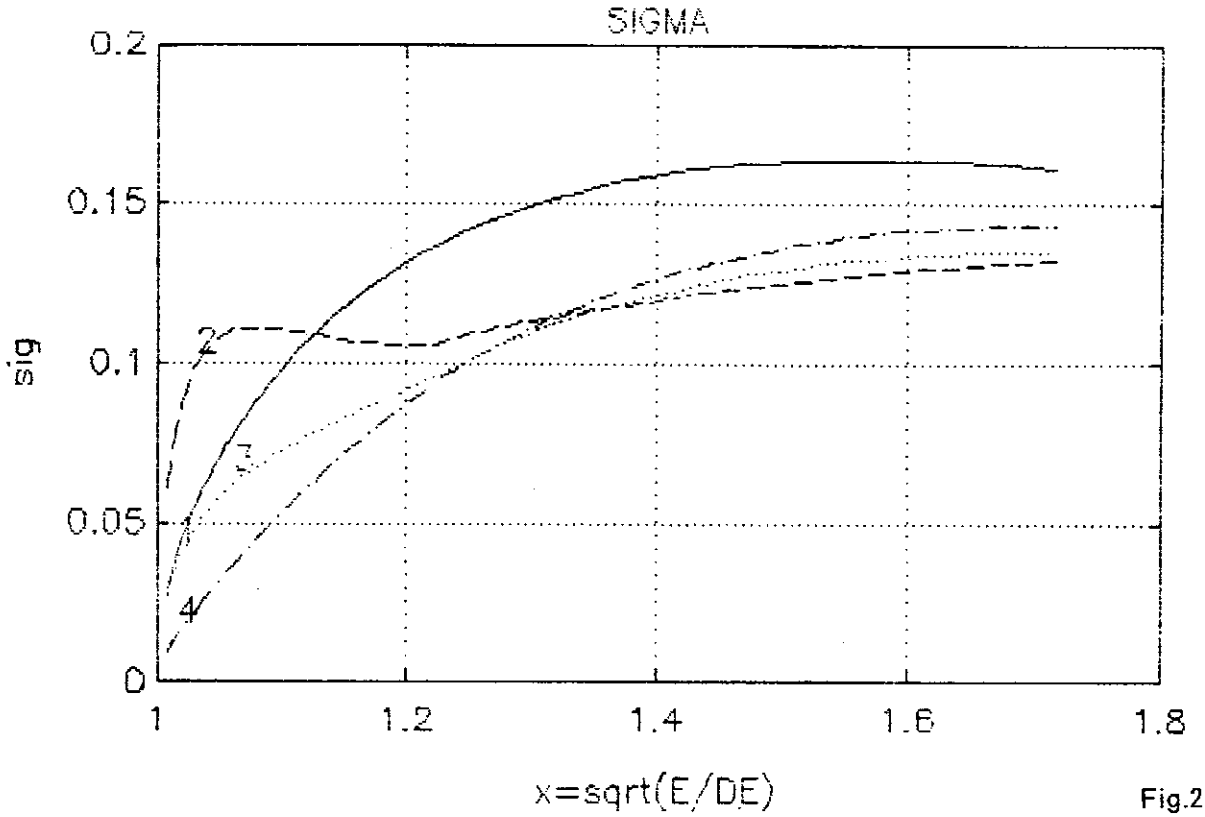
SIGMA
0.2
0.15
0.1
0.05
0
sig
2
3
4
1
1.2
1.4
1.6
1.8
x=sqrt(E/DE)

Fig.2

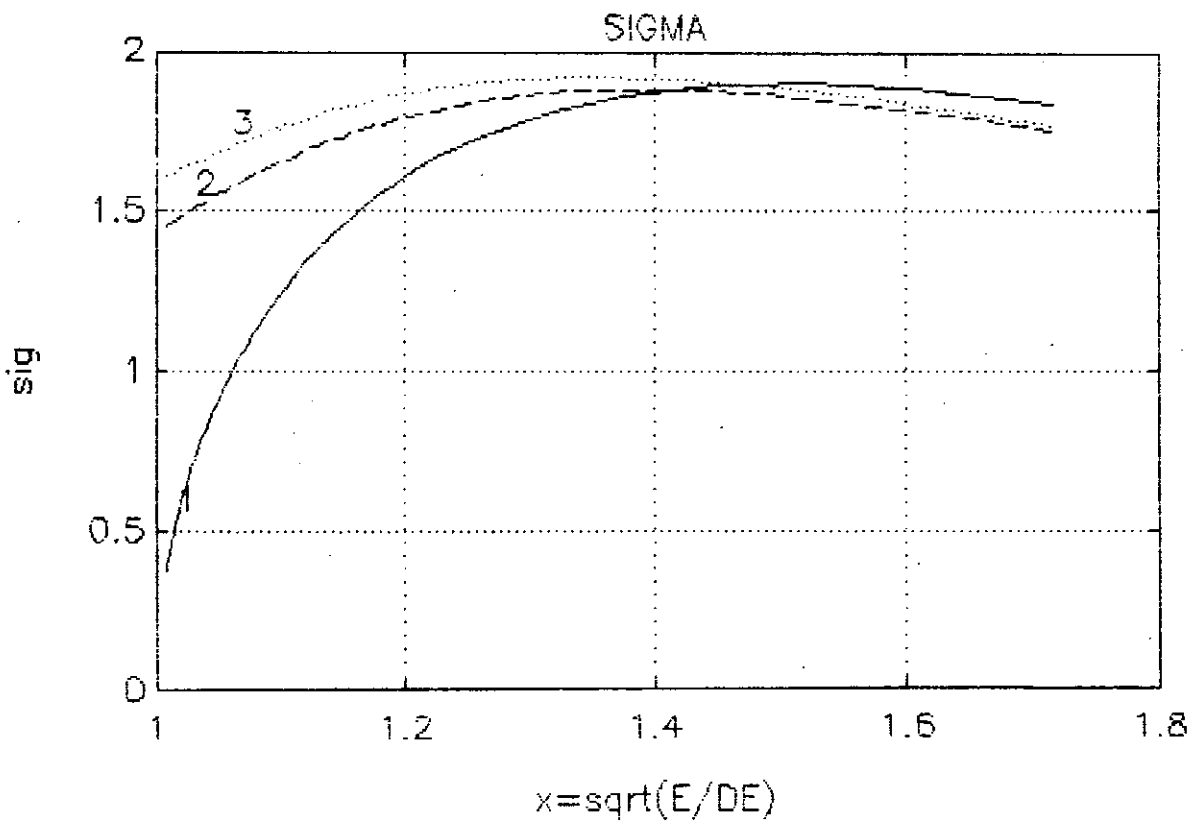
SIGMA
2
1.5
1
0.5
0
sig
3
2
1
1.2
1.4
1.6
1.8
x=sqrt(E/DE)

Fig.3

Differential Cross Sections for Electron-Impact Excitation of Atomic Ions

Yukikazu Itikawa and Kazuhiro Sakimoto
Institute of Space and Astronautical Science
Yoshinodai, Sagamihara 229

We have been working on a theoretical study of electron-impact excitation of atomic ions. Recently our calculation has been extended to differential cross sections (DCS). Differential cross section gives much detailed information about the excitation mechanism. In particular, it is interesting to see how the DCS change along an isoelectronic sequence and how is the difference between the DCS for ions and that for neutral atoms. Furthermore, DCS is useful in making clear the difference in various theoretical approximations.

The present calculation is based on a distorted wave method. In some cases, use is made of the Coulomb-Born approximation for comparison. First we introduce a distortion potential, U^{DW}. In principle, any potential can be chosen as U^{DW}. Here we employ a spherical average of the electrostatic potential of the target ion in its initial state. We use the same distortion potential for both the initial and the final states. We take into account an electron exchange only between the two electrons interacting with each other. The last but very important point is that, in our method, an accurate target wave function is used as far as possible. In most cases of electron-ion collision, the accuracy of the target wave function is essential in obtaining reliable cross section. More details of the present calculation are given in a previous paper.[1]

Figures 1 and 2 show the DCS calculated for the excitations of $2\ ^3S$ and $2\ ^1S$ states of He-like ions, respectively. To show the DCS for different ions along the isoelectronic sequence, we multiply the DCS by Z^4 (Z being the nuclear charge of each ion) and compare them at a given electron energy in threshold units. The DCS shown in Figs.1 and 2 are calculated at a given value of X ($X=E/\Delta E$, ΔE being the excitation energy). For the excitation of $2\ ^3S$ state (Fig.1), the angular dependence of the cross section is similar for all the ions. Even the cross section of neutral He has qualitatively the same angular dependence. This means that the essential mechanism of the excitation is the same for He and all the He-like ions. On the contrary, the cross section for the excitation of $2\ ^1S$ state (Fig.2) has a different feature depending on the nuclear charge. The cross section of He has a minimum at around 60°, but the cross section for highly charged ions has no such structure. The cross section of Li^+ has a shape in between. The DCS calculated for

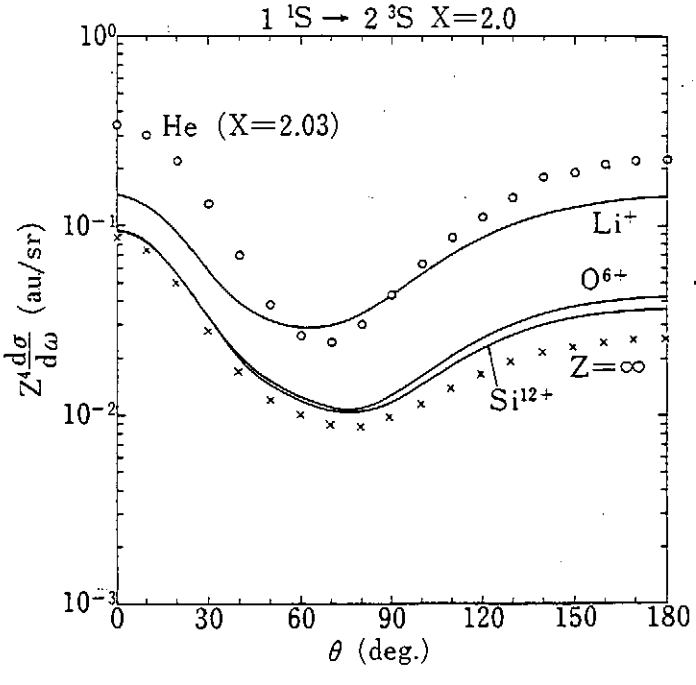

Fig.1

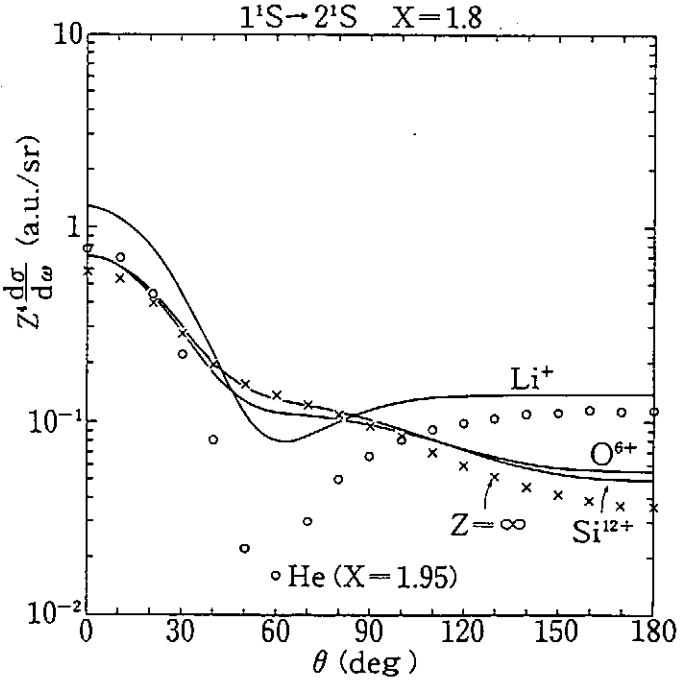

Fig.2

other transitions and/or other energies are shown in our papers.[2,3]

Now one typical example is shown of the usefulness of the DCS in understanding the collision mechanism. In Fig.3, the integral cross sections for the 2 ^{1}S excitation are plotted against collision energy. Excitation cross section of neutral atoms usually starts from zeroat the threshold. In the case of ions, however, cross sections start from a finite value. Then as the collision energy increases, some cross section (e.g., O^{6+}) goes down, but other one (e.g., Li^+) goes up. What makes this difference? Figures 4 and 5 show the corresponding DCS calculated at X=1.2 and 1.8. The cross section is roughly divided into two parts: the forward scattering and the backwardone. In the case of O^{6+}, the forward scattering decreases but the backward one increases, as the collision energy goes down to threshold. The latter increase overcomes the former decrease so that the integral cross section increases. In the case of lithium, the forward scattering decreases also, but the contribution of the backward scattering does not change much. (Actually the backward peak increases but the area under the curve does not change.) As a result, the integral cross section of lithium decreases as the energy goes to

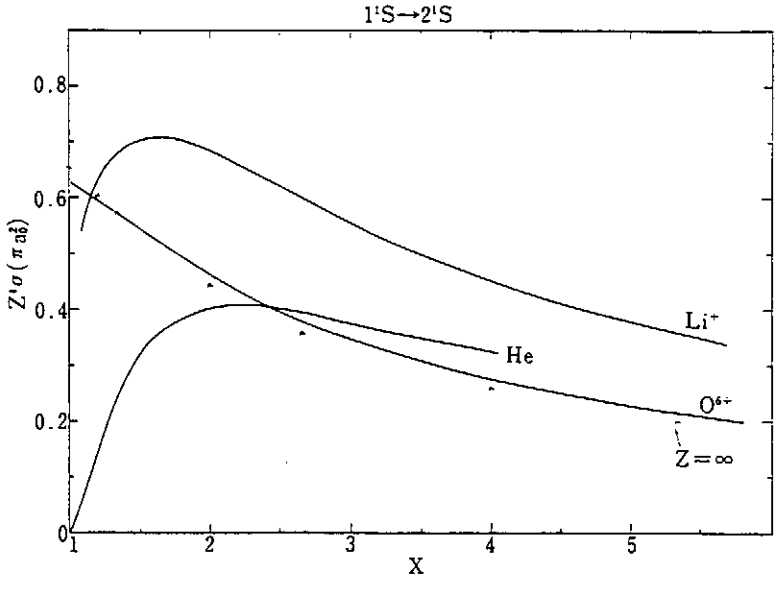

Fig.3

threshold. In the case of highly charged ions, the incident electron is attracted by the strong Coulomb potential and comes closer to the target. This effect is enhanced near threshold, because the electron speed is relatively low. Thus the short-range interaction dominates near threshold in the excitation of O^{6+}. This is the reason of the increase of the backward scattering for O^{6+}.

As in this example, we can understand the collision process more clearly with the use of DCS. More recently we have calculated the orientation and alignment parameters in the excitation of H- and He-like ions.[4] Those parameters provide another detailed information about the collision mechanism. These our calculations would be helpful in the spectroscopic study of high temperature plasmas.

References

1. Y.Itikawa and K.Sakimoto, Phys.Rev.A 31, 1319 (1985).
2. Y.Itikawa and K.Sakimoto, Phys.Rev.A 38, 664 (1988).
3. K.Sakimoto and Y.Itikawa, Phys.Rev.A 40, 3646 (1989).
4. R.Srivastava, Y.Itikawa and K.Sakimoto, in preparation.

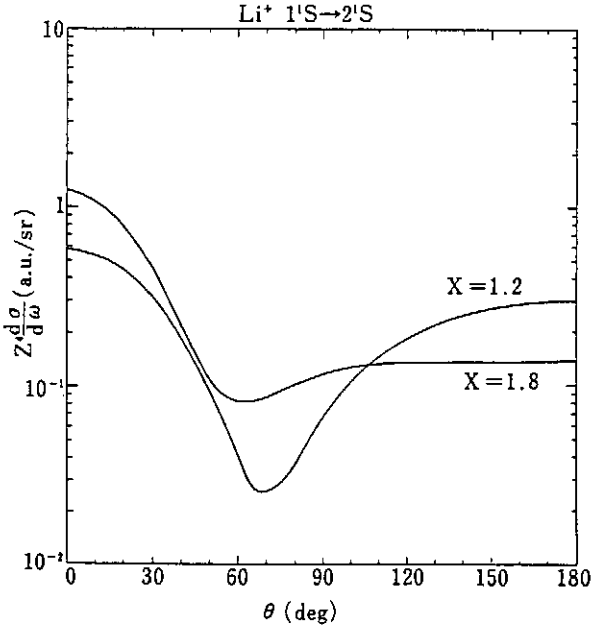

Fig.4

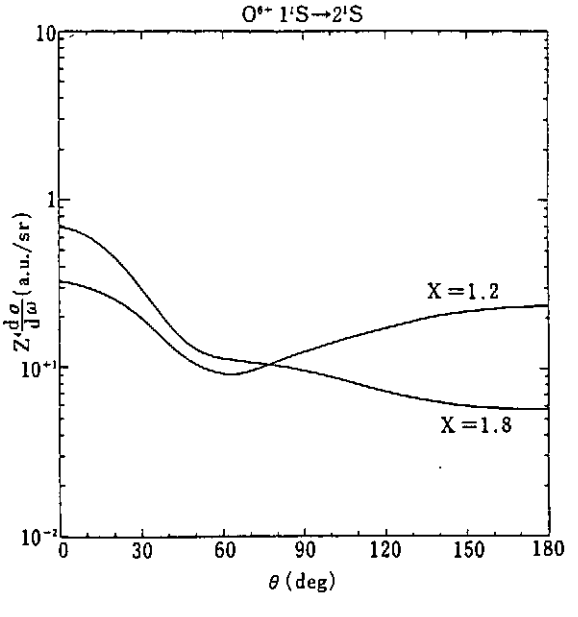

Fig.5

Plasma Diagnostics Using Line Intensity Ratios

Kuniaki MASAI

Plasma Science Center, Nagoya University
Nagoya 464-01, Japan

ABSTRACT We discuss atomic concepts for electron temperature and density diagnostics of plasmas by use of line emission therefrom. The principle is related to competitive processes for the level population of atoms. Results of the measurement on the JIPP T-IIU tokamak are presented to demonstrate their usefulness for plasma research. The T_e measure deduced from the line intensity ratio indicates underionization of oxygen in the plasma peripheral region, suggesting a presence of significant transport toward the higher temperature region.

1. Introduction

Spectroscopy of radiation from plasmas is of practical importance for diagnostics as well as of interest of atomic physics. Spectra of various species in a plasma give information of their abundances and ionization states, and also of the electron temperature (T_e) and the electron density (n_e) which are the primary quantities of the plasma. Although the temperature and the density of a plasma can be measured also by other means, e.g., Thomson scattering, the ones derived from line spectra have another meaning; they directly reflect the environment of the emitting ion to be a probe for the local plasma conditions.

In view of atomic physics, basic concepts for obtaining T_e and n_e are so simple as to be applied easily for various configurations of atomic structure. We here discuss T_e and n_e measurements by use of line spectra of oxygen and iron. These are the representative impurity species in laboratory plasmas and also the key elements in astrophysical plasmas because of their stable atomic nuclei. In the following section, excitation process associated with T_e measurement is discussed for line pairs of oxygen ions with L-shell electrons. In section 3 we discuss n_e dependence of line intensity ratio of B-like iron. All examples shown here to demonstrate T_e and n_e sensitivities

are those observed from tokamak plasmas on the JIPP T-IIU device of National Institute for Fusion Science. We have watched the line spectra to obtain T_e and n_e, however, our interest has not been focused only on this subject. Based on T_e and n_e derived, we have further tried to investigate the physical surroundings of the emitting ions. From this point of view, in section 4 we mention the impurity transport suggested from the T_e measurement by line emission.

2. T_e sensitive line pairs

We consider electron-impact excitation which is immediately followed by line emission. In practical applications for plasma, where the electrons are substantially in a Maxwell distribution, so called rate coefficients are more convenient rather than cross sections. Integrating the cross section over the electron velocities with a Maxwellian kernel, one can obtain the rate coefficient straightforward in a form

$$C(T_e)=\langle \sigma v\rangle \propto \langle g\rangle T_e^{-(1/2+\alpha)} e^{-E/T_e}, \qquad (1)$$

where E is the excitation energy, σ the cross section, g the Gaunt factor, and the bracket $\langle A\rangle$ means the average of the quantity A over the Maxwellian characterized by the temperature T_e. α is a numerical factor introduced to represent the effect of spin change; $\alpha \simeq 0$ for electric dipole transitions (E1), and $\alpha > 0$ for transitions accompanied with spin quantum number changes. The dependence, $T_e^{-(1/2+\alpha)}$, is of practical importance at temperatures higher than a temperature T_m, at which the rate coefficient reaches its maximum. Because of a weak dependence of this part, the application is not good for temperatures higher than T_m; also $\langle g\rangle$ is noted to depend weakly on the electron temperature. Therefore, the temperature diagnostics is valid practically at $T_e < T_m$, where the exponential part in eq. (1) plays a dominant role.

Line intensity is proportional to the excited-state population, which is determined generally by a couple of equations of all the transitions among all the energy levels. However, the problem is much reduced for two extreme cases of the electron density, which is compared to the radiative transition

probability divided by the rate coefficient of the competitive collisional process. At a high density limit, de-excitation is dominated by collisional transitions, and the population is ruled by a Boltzmann distribution, as described in more detail in the next section. On the other hand, at electron densities so low that radiative transition dominates de-excitation, the population of excited state is negligible in comparison to that of the ground state, in other words, corona condition holds. Here we consider the latter case which is approximately attained for tokamak plasmas.

Under a corona condition, since the excitation is followed immediately by radiative decay to lower levels, the radiation intensity is directly proportional to the rate of excitation from the ground state. Then, for the intensity ratio of two lines following excitation from the ground state, we have

$$I'/I \simeq \langle \sigma' v \rangle n'/\langle \sigma v \rangle n \propto (n'/n)(\langle g' \rangle/\langle g \rangle) T_e^{-(\alpha'-\alpha)} e^{-(E'-E)/T_e}, \quad (2)$$

where n and n' represent the ground state populations or immediately the ion abundances if corona conditions are attained. As readily seen, eq. (2) further reduces by an appropriate choice of the line pair with n'=n and $\alpha'=\alpha \simeq 0$; the former means the same ionic state of the same species, and the latter suggests a use of E1 transition lines, which are favorable also for satisfying corona conditions because of their larger values of radiative transition probability and for little influence of T_e on $\langle g' \rangle/\langle g \rangle$. Furthermore, a line pair with large difference in the excitation energy is useful because a large value of $(E'-E)/T_e$ means a good sensitivity to the electron temperature. Finally, one has to recall the practical validity of application for temperatures lower than T_m, which should hold for a line at least of the pair.

We have applied the above concept to diagnose the peripheral region of plasmas in a way complementary to the measurement by use of Thomson scattering technique. We use 2s-3p to 2s-2p ratio of resonance series lines of B-, Be- and Li-like oxygen.[1] The 2s-2p lines are the resonance lines of such ionic states with incomplete L-shells. The excitation energy for the resonance line is rather small because of the transition between the same

principal quantum numbers. Therefore, the combination with the 2s-3p line is good to realize the requirement of much different excitation energies.

In Figs. 1(a), (b), (c) shown are the time evolution of the line intensity ratios of 2s-3p to 2s-2p transitions of O IV, O V and O VI, respectively. These line intensity ratios were observed for the ohmic discharge with additional heating by radio of ion cyclotron range of frequency (ICRF) accompanied with gas puffing at around 150 ms.[2] In coincidence with ICRF heating and gas puffing, a rapid decrease in the line intensity ratio was observed for all of O IV, O V and O VI. This indicates a rapid decrease of the electron temperature in the environment of these ions. When RF turned off, the intensity ratio or the electron temperature recovered from its level during the RF heating phase. The behavior found by the O IV-VI lines were confirmed by Thomson scattering focused specially on the outermost region of the plasma. In contrast to the plasma peripheral, a monotonic increase of the electron temperature by RF heating was observed for the plasma core region.

The same manner was applied for a plasma after 'carbonization', which is a technique to coat the vessel wall with carbon to suppress the radiation loss due to metal impurities coming from the wall surface. The intensity ratios obtained from the O V and VI lines after carbonization are shown in Fig. 2. In comparison with Fig. 1 before carbonization, one can see the T_e measure being kept at a low level still after ICRF turn off. This may be explained straightforward by 'T_e suppression' triggered by the application of ICRF. It could be entirely the case if the electron density in the environment of the oxygen ions were not changed. If we recall the oxygen ions are in an ionizing condition, however, the apparent decrease in T_e may be accounted for also by an increase in n_e. Finally, comparison with the results from other diagnostics reveals that the hydrogen recycling rate, which tends to be enhanced after carbonization, is increased by stimulation of the wall surface through the application of ICRF and results in suppression of the T_e measure observed. T_e and n_e measurement by emission lines has a meaning different from usual one such as Thomson scattering, and their combination gives more fruitful results for plasma research than what each measurement does.

3. n_e sensitive line pairs

Radiative transition probability (Einstein's A coefficient) of hydrogenic ions is proportional to Z^4 for E1, where Z is the nuclear charge, while the rate coefficient of collisional transition is proportional to Z^{-3} at a characteristic temperature $\sim T_e/Z^2$ normalized to a hydrogenic ionization potential. Accordingly the density to satisfy a corona condition increases roughly in proportion to Z^7 with increasing the atomic number in the case of a level associated with electric dipole transitions.

In a tokamak plasma, the corona condition is primarily satisfied for resonance series lines of oxygen. This gives a theoretical ground for their intensity ratios to be a measure of T_e without significant influences of the electron density. For some metastable excited levels, however, the corona population is not attained; this means a possible application for density diagnostics. For illustrative purpose, a schematic energy diagram of O V is shown in Fig. 3, where $2s2p(^3P)$ is a metastable excited level. Excitation rate to $2s2p(^3P)$ is in proportion to n_e and the excitation rate to $2p^2(^3P)$ therefrom is again in proportion to n_e. If de-population of $2s2p(^3P)$ state is dominated by excitation to $2p^2(^3P)$, the intensity of following line emission, $2s2p(^3P)$-$2p^2(^3P)$, is to be nearly proportional to n_e^2. Thus, the intensity ratio of this line to an E1 transition line excited directly from the ground state, e.g., resonance line $2s^2(^1S)$-$2s2p(^1P)$, should exhibit a density dependence proportional to n_e. In practice, however, the level population with metastable excited levels is complicated more than the above qualitative account because of various possible branching in transitions,[1)] and the resultant intensity of line emission following excitation from the metastable level is not always proportional to n_e^2.

As seen also from the above argument, density diagnostics by line intensity ratios is based on the level population in the intermediate regime between a corona distribution and a Boltzmann distribution. Focusing on this point, we here discuss the electron density dependence of a line pair of B-like iron.[3)] The ground state of such highly ionized iron with incomplete L-shell consists of two or more sublevels being multiplet. At a low density limit the population of the upper sublevel is negligibly

small compared to the lowest one. With increasing the electron density, the population of the upper sublevel increases and results in the enhancement of line emission following excitation therefrom. Therefore, the intensity ratio of a line excited from the upper sublevel to a line excited from the lower sublevel is to be a measure of n_e. It should be noted, in contrast to the case of temperature diagnostics, that a line pair of close excitation energies is favorable for density diagnostics to be free from a significant influence of T_e dependences.

A box in Fig. 4 shows a schematic diagram of energy levels related to the density diagnostics, the doublet ground state and the upper state excited therefrom, of B-like iron (Fe XXII). Here the energy levels are referred to the indices, level 1 to 4, on the right hand side of the respective levels. Physical quantities related to transition are distinguished thereby with subscripts as A_{ij}, C_{ij}, E_{ij} and so forth for the transition from level i to level j, as also shown in Fig. 4 for rate coefficients of collisional excitation. At the beginning we consider a 4-level atom to give a simple account for density dependences, and afterward present the results from computation including more levels.

The line intensity ratio of I_{42} (114 A) to I_{31} (117 A) can be written approximately,

$$I_{42}/I_{31}\simeq(b_{42}/b_{31})[(C_{14}/C_{13})+(C_{24}/C_{13})(n_2/n_1)], \qquad (3)$$

where $b_{jk}=A_{jk}/(\Sigma_i A_{ji}+n_e\Sigma_i C_{ji})$ represents the branching ratio of the radiative transition, and n_1 and n_2 are the population densities of level 1 and level 2, respectively. For the 4-level system, the relative population is easily obtained from a balance of transitions as,

$$n_2/n_1\simeq[n_e(C_{12}+C_{14}B_{42})]/[n_e(C_{21}+C_{24}B_{41})+A_{21}], \qquad (4)$$

where $B_{4k}=(A_{4k}+n_eC_{4k})/(\Sigma_i A_{4i}+n_e\Sigma_i C_{4i})$ is the branching ratio for the transition from level 4 to k.

The radiative transition probability, $A_{21}\simeq1.39\times10^4 s^{-1}$, compared to other competitive collisional transitions from level 2 gives a clue for the density dependence of I_{42}/I_{31}. The density dependence of the line intensity ratio can be classified into three regimes depending on the population of the ground

state sublevels, as (Ⅰ) corona equilibrium, (Ⅱ) intermediate regime and (Ⅲ) Boltzmann equilibrium with increasing the electron density. We begin with two extreme cases, Ⅰ and Ⅲ.

(Ⅰ) At densities so low as $n_e \ll A_{21}/C_{2j}$ for a given j in eq. (4), $n_2/n_1 \simeq A_{21}^{-1}$ is much smaller than unity or the population of level 2 is negligible compared to level 1. This is just a requirement for a corona condition as described in section 2. Then eq. (3) much reduces to

$$I_{42}/I_{31} \simeq (b_{42}/b_{31})(C_{14}/C_{13}), \tag{5}$$

and in proportion to the ratio of the excitation rate coefficients which are functions only of T_e. Because of a small difference of the excitation energies, temperature dependences of C_{14} and C_{13} are very similar to each other as seen in Fig. 4. Thus, eq. (5) gives a value nearly constant in a wide electron temperature range. This corona regime is attained for electron densities practically as $n_e \lesssim 10^{12} cm^{-3}$, and is established at $n_e \lesssim 10^{11} cm^{-3}$ which gives a corona limit value, $I_{42}/I_{31} \simeq 0.17$.

(Ⅲ) Now we consider the opposite extreme case. At $n_e \gg A_{21}/C_{2j}$, the population of the ground state is determined by a collisional balance. Then, n_2/n_1 is independent of n_e, and the resultant line intensity ratio is given by

$$I_{42}/I_{31} \simeq (b_{42}/b_{31})(C_{24}/C_{13})[(C_{12}+C_{14}B_{42})/(C_{21}+C_{24}B_{41})], \tag{6a}$$

which depends much weakly on n_e through B_{4i}. With increasing n_e, B_{4k} approaches $C_{4k}/\Sigma_i C_{4i}$ which is independent of n_e, and the population of the 4-level atom is ruled completely by collisional processes to be a Boltzmann distribution. Then, eq. (4) reduces $n_2/n_1 \simeq C_{12}/C_{21} \simeq 2$, where the last expression comes from the statistical weight taking into account $E_{12} \ll T_e$ of interest for B-like iron. Hence, at a high density limit the line intensity ratio is approximated by

$$I_{42}/I_{31} \simeq 2(b_{42}/b_{31})(C_{24}/C_{13}). \tag{6b}$$

As seen from Fig. 4, since the value C_{24}/C_{13} is almost unity over a wide range of T_e, eq. (6b) may further reduce to $I_{42}/I_{31} \simeq 2(b_{42}/b_{31}) \simeq 2.3$. This value or eq. (6b) is valid for

$n_e \gtrsim 10^{20} cm^{-3}$, and eq. (6a) is attained for $n_e \gtrsim 10^{15} cm^{-3}$, where the line intensity ratio is little sensitive to n_e.

(II) In the intermediate region, $10^{12} \lesssim n_e \lesssim 10^{15} cm^{-3}$, the intensity ratio is to vary from the value at the regime I to one at the regime III. On account of the n_e dependence in eq. (4), we introduce a parameter defined as,

$$q \equiv [1+(C_{24}/C_{14})(C_{12}+C_{14}B_{42})/(C_{21}+C_{24}B_{41})]^{-1/2}, \quad (7)$$

with which the line intensity ratio is approximately expressed as what is proportional to $n_e^{(1-q)/(1+q)}$. After some algebra, we can derive the line intensity ratio in a form

$$I_{42}/I_{31} \simeq q^{-1}(b_{42}/b_{31})(C_{14}/C_{13})(n_e/n_{e0})^{(1-q)/(1+q)}, \quad (8)$$

where $n_{e0} \equiv qA_{21}/(C_{21}+C_{24}B_{41})$ is the density at which the power of n_e takes its maximum value. Since q remains nearly constant being $\simeq 1/3$ in the range of $n_e \simeq 10^{13}$-$10^{14} cm^{-3}$, eq. (8) gives a dependence as $I_{42}/I_{31} \propto n_e^{1/2}$. This is realized in particular at around n_{e0}, where the line intensity ratio is most sensitive to n_e according to its definition.

The result of computations for a 10-level system is shown in Fig. 5. We take into account possible competitive transitions to and from all n=2 levels, including excitation by proton and deuteron impact, for which rate coefficients are denoted by C^p_{12} and C^d_{12}, respectively as shown in Fig. 4. Fig. 6(a) shows the intensity ratio observed for the tokamak discharge of H/D mixed gas, where ICRF is applied with gas puffing through 120 ms to 160 ms. In comparison, shown in Fig. 6(b) is the line-averaged electron density measured by use of microwave interferometer; one can see that the line intensity ratio exhibits a time behavior very similar to the line-averaged n_e. The line intensity ratios at 100 ms and 140 ms are plotted on Fig. 5 against the line-averaged n_e and the central n_e obtained by Thomson scattering. A disagreement at 140 ms, the excess of I_{42}/I_{31}, can be ascribed to an additional contribution of the suprathermal deuterons enhanced by ICRF.

4. Summary and remarks

In the previous sections principles for the measurement of temperature and the density are discussed in view of atomic processes. Fig. 7 demonstrates combination of the temperature measure from O V and the density measure from Fe XXII observed for 4 conditions of tokamak discharge. Here one can see a good response of the line intensity ratios to the respective plasma conditions. The temperature and the density in the environment of the ions responsible for emission are an immediate outcome from the line intensity ratios. It should be noted, however, that T_e and n_e measurement by emission lines stands on a different meaning from one by such Thomson scattering as on an absolute spatial coordinate; the local values of T_e and n_e from the former are referred not to the geometrical structure of a plasma but to the thermal structure through the location of emitting ions, and this difference gives valuable information in a different way.

We briefly mention nonequilibrium ionization reflecting transport of impurities from the wall surface toward the plasma center. As seen in Fig. 1, the electron temperature deduced from the line intensity ratio is high relatively to the ionization state; at such a high temperature oxygen could be more ionized if collisional ionization equilibrium were attained. Deviation from ionization equilibrium can be represented by a collision time effective for ionization process. Without transport, time required for ionization equilibrium at a given T_e is roughly estimated as $t_{EQ} \sim 0.1(n_e/10^{13}\mathrm{cm}^{-3})^{-1}\mathrm{s}$. Under a presence of the transport as significant as $v\nabla \ln T_e > t_{EQ}^{-1}$, where v is an inward velocity characterizing the transport, however, any equilibrium condition is not attainable in a time-like trajectory. Hence, in the case of $v \gtrsim 100(a_p/10\mathrm{cm})(n_e/10^{13}\mathrm{cm}^{-3})\ \mathrm{cm\ s}^{-1}$, where a_p is the plasma radius, the impurity transported toward the higher T_e region is in a stationary state of underionization compared to one in an equilibrium at the local T_e. This suggests another aspect of the temperature diagnostics by line emission for the impurity-transport study.

References

1) Kato, T., Masai, K. and Mizuno, J., J. Phys. Soc. Japan 52, 3019, 1983.

2) Ogawa, Y., Masai, K., Watari, T. et al., Nucl. Fusion 29, 1873, 1989.

3) Masai, K. and Kato, T., Phys. Lett. A 123, 405, 1987.

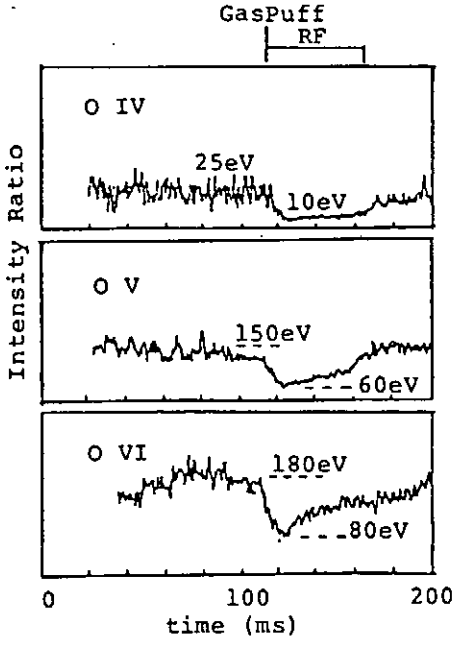

Fig.1 Time variation of the intensity ratio; O IV $2s^22p(^2P)-2s^23d(^2D)/2s^22p(^2P)-2s2p^2(^2D)$, O V. $2s^2(^1S)-2s3p(^1P)/2s^2(^1S)-2s2p(^1P)$, and O VI $2s(^2S)-3p(^2P)/2s(^2S)-2p(^2P)$.

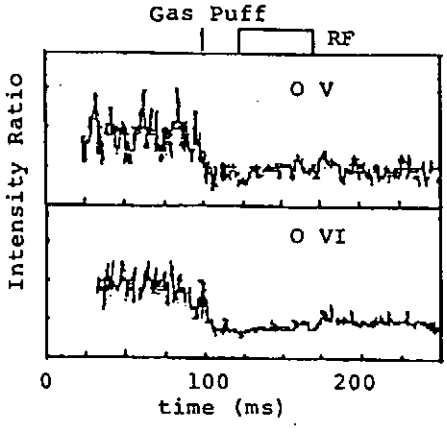

Fig.2 Intensity ratio of O V and VI lines from plasmas after carbonization (see text).

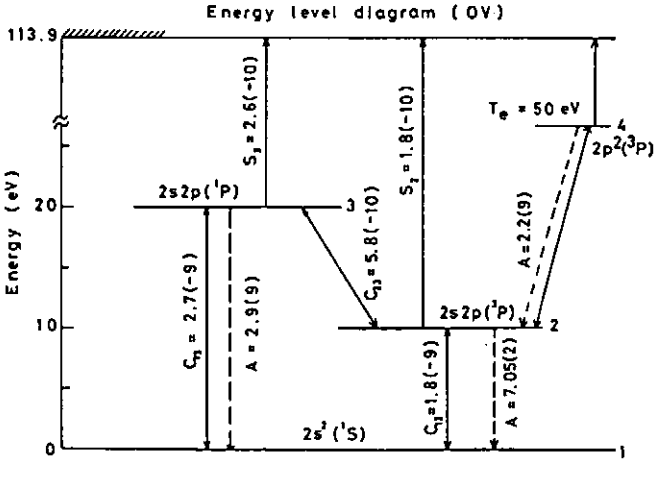

Fig.3 Schematic energy diagram of O V.

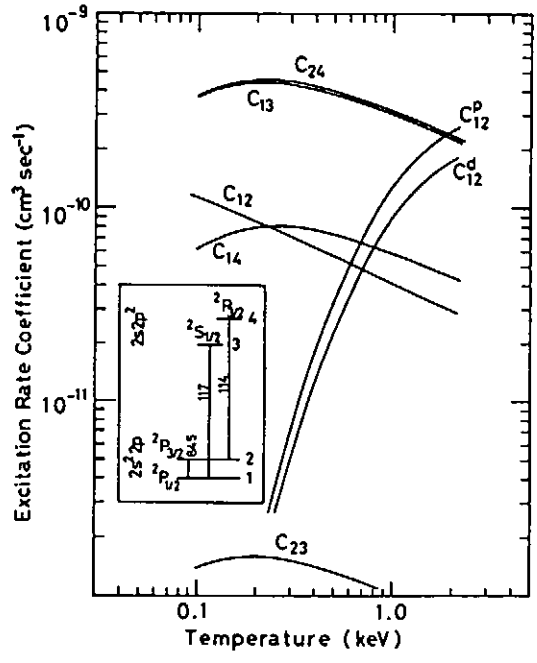

Fig.4 Temperature dependences of rate coefficients for collisional excitation and the schematic energy diagram of Fe XXII.

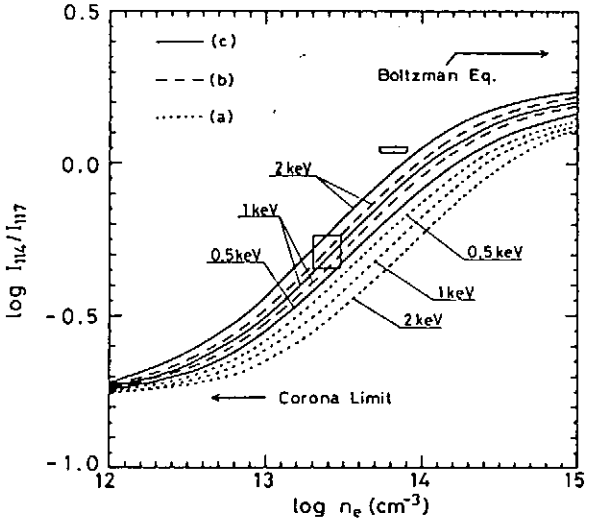

Fig.5 Density dependence of I_{42}/I_{31}, line intensity ratio $2s^22p(^2P_{3/2})$-$2s2p^2(^2P_{3/2})$ to $2s^22p(^2P_{1/2})$-$2s2p^2(^2S_{1/2})$ of Fe XXII. Excitation by (a) electrons, (b) electrons, deuterons and protons with e/d/p=1.0/0.9/0.1, and (c) electrons and protons with e/p=1.0/1.0 is taken into account. Boxes represent the observed values for the electron densities measured by Thomson scattering and microwave interferometer.

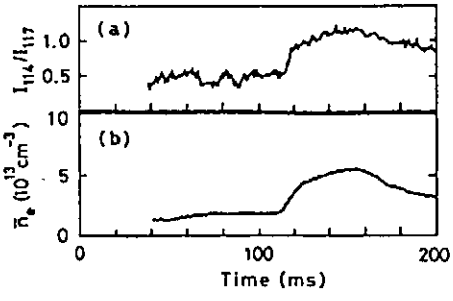

Fig.6 Time variations of (a) I_{42}/I_{31} and (b) line-averaged electron density measured by microwave interferometer.

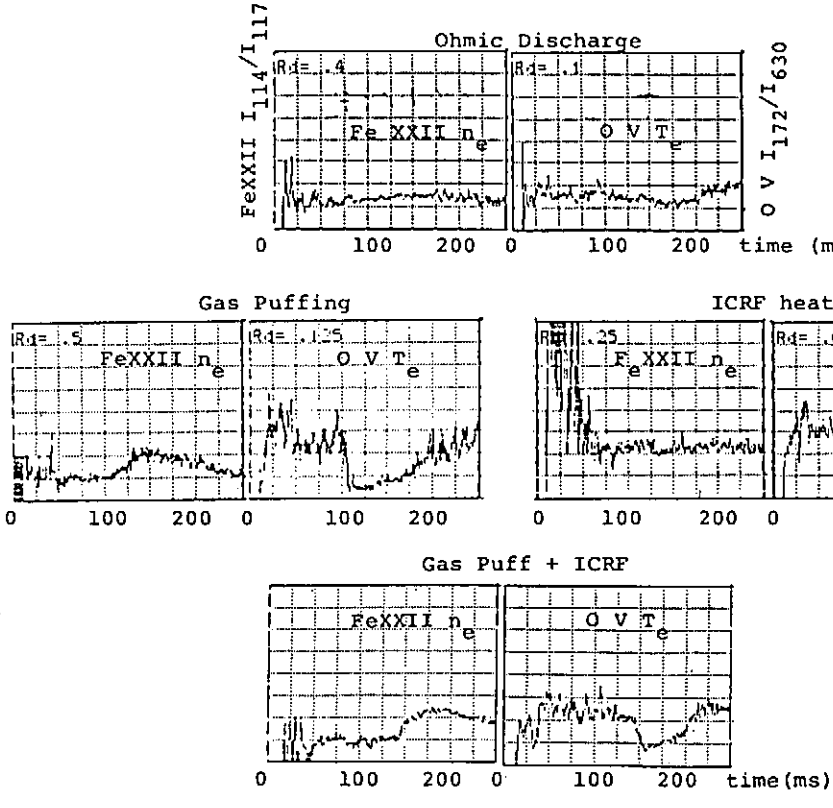

Fig.7 Time variations of the electron temperature measure from O V lines and the density measure from Fe XXII lines for 4 cases of discharge; (a) ohmic heating, additional (b) gass puffing at 105ms, (c) ICRF heating at 120ms, and (d) gass puffing and ICRF heating at 145ms.

Plasma Diagnostics of Solar Flares with SOLAR-A/ Bragg Crystal Spectrometer (BCS)

Tetsuya Watanabe
National Astronomical Observatory
Mitaka, Tokyo 181, Japan

Abstract: The BCS experiment on the Japanese satellite of SOLAR-A launched by ISAS in 1991 has capability of observing the highest temperature solar flare plasma from 3 to 100 million deg. with increased sensitivities and temporal resolutions. The primary scientific target of this experiment is to reveal plasma heating and dynamics of solar flares at their impulsive phases, which has keys to understand the mechanisms of energy release and energy deposition of solar flares in the outer atmospheres of the sun. The instrument has four crystals, which cover the wavelengths of the resonance lines of helium-like ions of sulpher, calcium, and iron and the Lyman alpha line of the hydrogen-like iron. The onboard microprocessor of BCS controls its observing mode, taking the shutter speed of spectra less than a second at the initial phase and gradually longer ones in the decay phase of flares. Combining the increased sensitivity of crystals and detectors, and the increased capability of the onboard microprocessor, the SOLAR-A/BCS will contribute in understanding the problems left unresolved in the last maximum of solar activity.

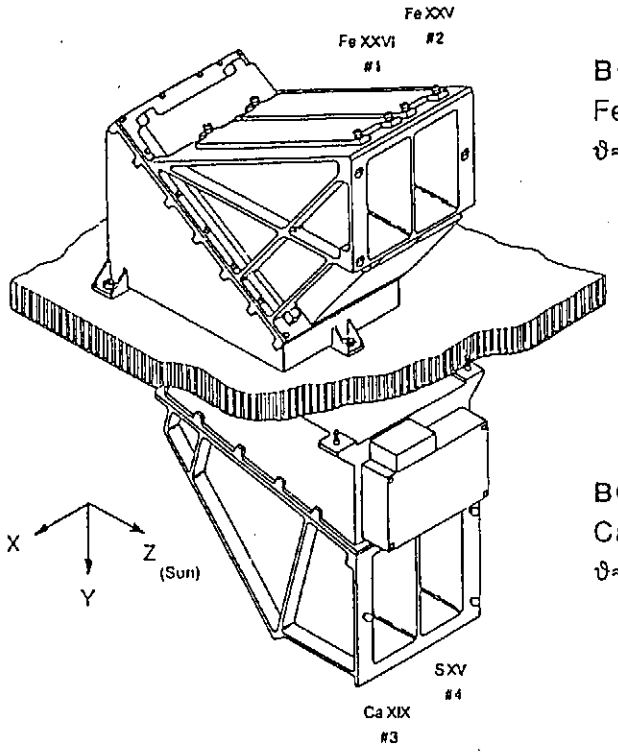

TABLE OF SOLAR A BCS CHANNELS

Channel no.	Ion	T_{max} (K)	Crystal	$2d$ (Å)	Crystal area cm × cm	Wavelength Range (Å)	Sensitivity w.r.t. *SMM*
1	S XV	1.6×10^7	Ge 111	6.5331	3.8 × 11.4	5.0160 – 5.1143	63.
2	Ca XIX	3.2×10^7	Ge 220	4.000	3.8 × 11.4	3.1631 – 3.1912	5.8
3	Fe XXV	7.1×10^7	Ge 220	4.000	3.8 × 17.9	1.8298 – 1.8942	8.7
4	Fe XXVI	15.8×10^7	Ge 220	4.000	3.8 × 17.9	1.7636 – 1.8044	9.2

* With respect to the *SMM* FCS, scanning at 100 arc sec per second.

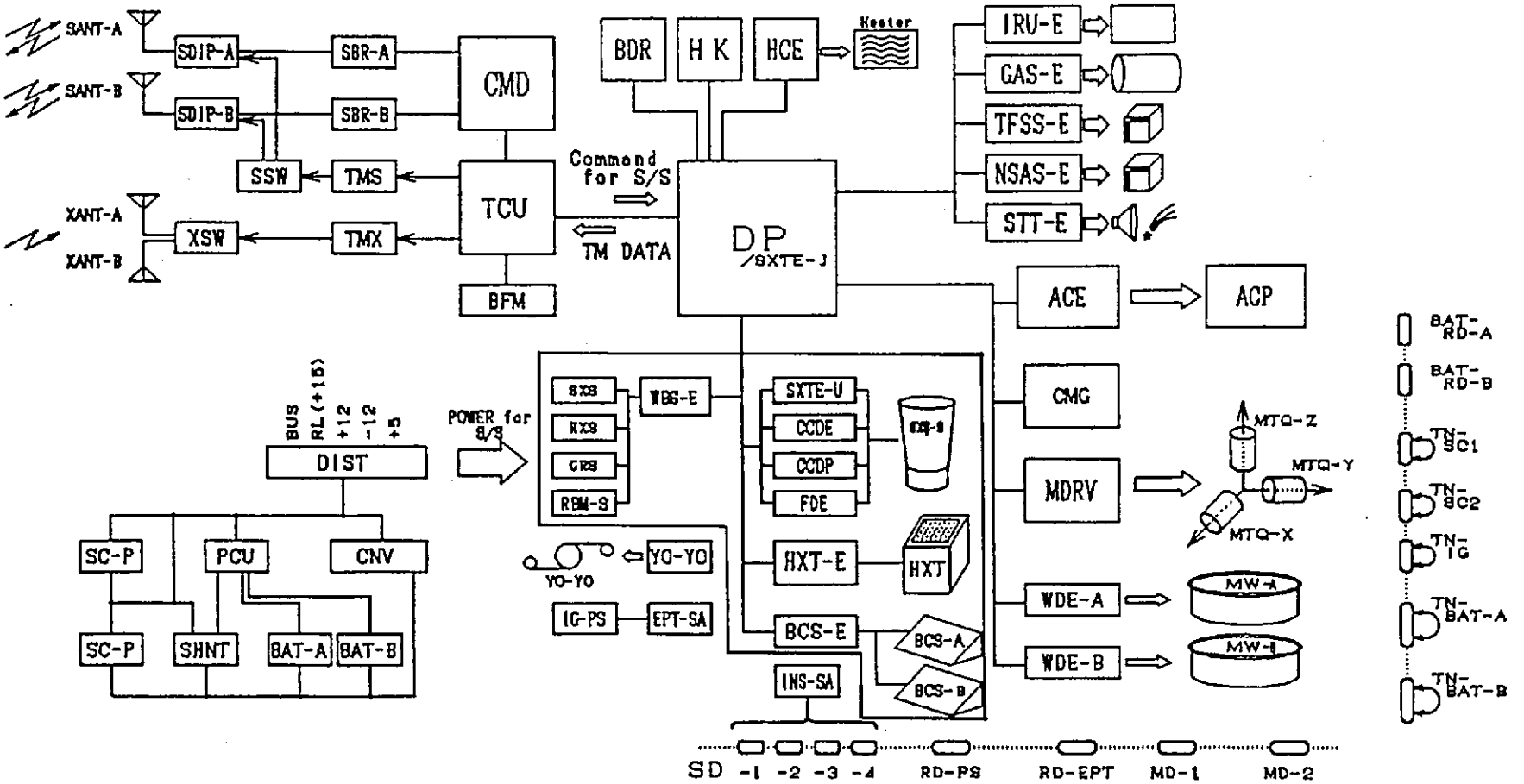

Fig.7-3 SOLAR-A System Block diagram

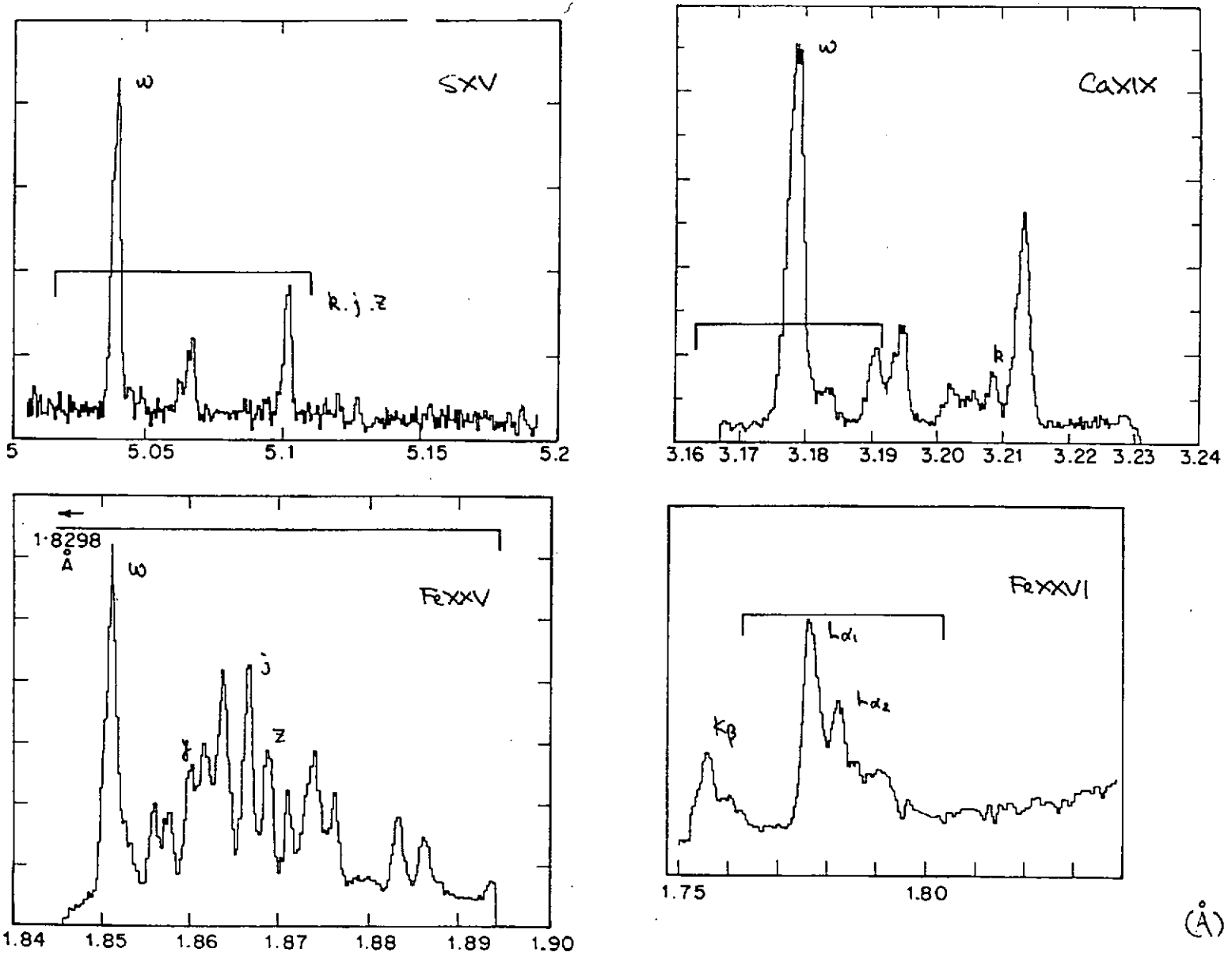
w
SXV
k.j.z
5
5.05
5.1
5.15
5.2
w
CaXIX
k
3.16
3.17
3.18
3.19
3.20
3.21
3.22
3.23
3.24
1·8298 Å
w
FeXXV
j
z
1.84
1.85
1.86
1.87
1.88
1.89
1.90
FeXXVI
Lα1
Lα2
Kβ
1.75
1.80
(Å)

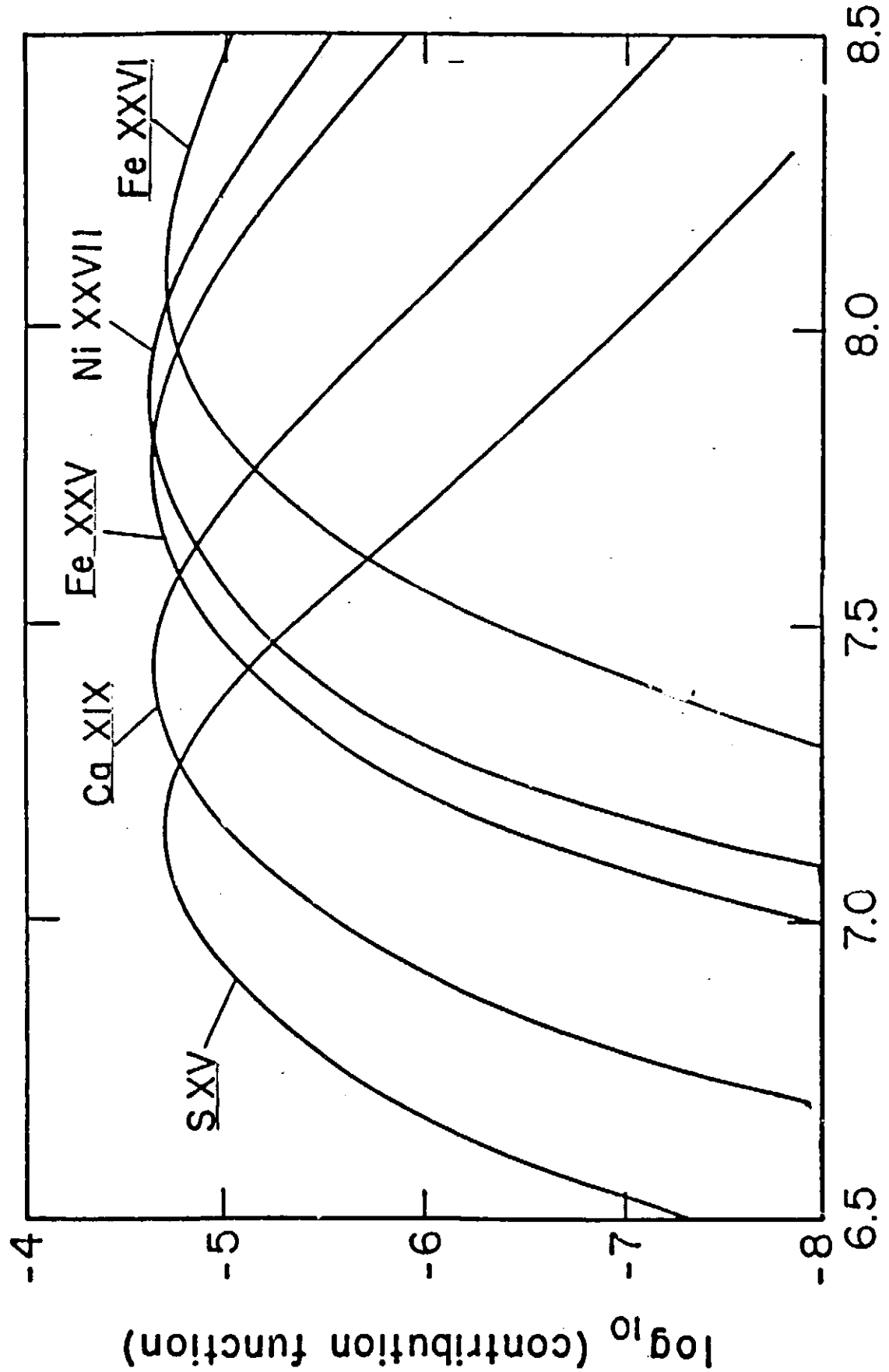
Fe XXVI
Ni XXVII
Fe XXV
Ca XIX
S XV
-4
-5
-6
-7
-8
6.5
7.0
7.5
8.0
8.5
log10 (contribution function)
log10 Te (K)

Figure 1

BCS Scientific Objectives

-plasma dynamics and heating during the impulsive phase of flares-

Plasma Dynamics

nonthermal (turbulent) motion

$\xi_t \simeq$ 44-170 km/sec (FeXXV; Hinotori)

no systematic limb effect

anti-correlation with source size

FeXXVI v.s. line broadening

?multiple mass ejection ← directed convective motion

?turbulence associated with magnetic reconnection

blue-shifted component

$V_t \simeq$ 300-400 km/sec

← chromospheric evaporation ← electron beam

← thermal conduction

?energetics

?completely shifted → double peak → blue enhancement

?multiple structure

Plasma Heating during the Impulsive Phase

?transient ionization ↔ $10^{-11} n_e \tau \lesssim 1$

?heating prior to 15×10^6 K with a high resolution spectrometer

? nonthermal electron heating

Superhot Component

?location and heating mechanism of FeXXVI

← chromospheric evaporation, nonthermal broadening

Plasma Diagnostics

?differential emission measure determined from broad band spectra

? diagnostic support for SXT and HXT

Abundance

?line/continuum ratio

He-like spectra from laboratory plasmas and solar flares

Takako KATO
National Institute for Fusion Science, Nagoya 464-01

May 15, 1990

1 Introduction

X-ray spectra of He-like ions have been measured from tokamaks and solar flares. Several physical parameters of a plasma can be derived from X-ray spectra of He-like ions. The ion temperature can be derived from the doppler width of a resonance line. The electron temperature is obtained from the intensity ratio of dielectronic satellite lines to a resonance line. In Fig.1 the energy level diagram for the prominent lines are shown. The following notations for the spectral lines are used in this article;
$w(2\ ^1P - 1\ ^1S)$, $x(2\ ^3P_2 - 1\ ^1S)$, $y(2\ ^3P_1 - 1\ ^1S)$, $z(2\ ^3S - 1\ ^1S)$, $q(1s2s2p\ ^2P - 1s^22s\ ^2S)$, $\beta(1s2s^22p\ ^1P - 1s^22s^2\ ^1S)$, j, $k(1s2p^2\ ^2D - 1s^22p\ ^2P)$.
The lines j and k are pure dielectronic satellite lines. Then the intensity ratios $I_k/I_w, I_j/I_w$ give the values of the electron temperature, where I_k, I_j and I_w indicate the intensities of the satellite lines k and j and the resonance line w, respectively. On the other hand, the line q in Fig.1 is produced mainly by the inner-shell excitation of Li-like ions and the line β produced by the inner-shell excitation of Be-like ions. Then the intensity ratios I_q/I_w and I_β/I_w give the ion density ratios n(Li)/n(He) and n(Be)/n(He), respectively, where n(He), n(Li) and n(Be) indicate the ion densities of He-like, Li-like and Be-like ions. The intensities of the intercombination (x and y) and the forbidden lines z are affected by the recombination from H-like ions. Then from the intensity ratios I_x, I_y, I_z to I_w, the ion density ratio n(H)/n(He) can be derived. The synthetic spectra including excition, ionization and recombination processe are fitted to the measurements.

In this article we will discuss He like X-ray spectra of titanium ions from a TFTR tokamak plasma[1] and of iron ions from Solar flares[2] in particular attention to a presence of high energy electrons which affect the spectra and ionization balances.

We consider a model that a hot component interacts with a bulk plasma. With this model, the time evolution of the spectra and ionization balances derived therefrom can be described consistently.

2 Atomic data

The rate coefficients for He-like lines and for Li-like satellite lines of Ti ions are adopted form ref.[3]. For dielectronic Be-like satellite lines, the data in [1] are used. The inner-shell ionization which contributes to z line is calculated by Lotz formula[4]. The cascade contributions from highly excited states and the recombination of H-like ions are taken into account[5]. The effective excitation rate coefficient calculated by our code for z for Ti ions is smaller than that of ref.[1] by a factor of 1.8[12]. The values in [1] is overestimated and their corrected values is 20 % larger than ours[6]. The effective excitation rate coefficients for x and y agree within 10 %. The effective recombination rates agree within 20 %. In Fig.2, ionization, recombination and excitation rate coefficients for Ti ions are compared for w, z, q and k lines. C_z^{eff} and α_z^{eff} indicate the effective excitation and recombination rate coefficient to produce z line, respectively. S_z is the inner-shell ionization rate coefficient from $1s^2 2s\ ^2S + e \rightarrow 1s2s\ ^3S + 2e$. The intensity I_z has three components due to the excitation of He-like ions, the inner-shell ionization of Li-like ions and the recombination of H-like ions.

$$I_z = C_z^{eff} n_e n(He) + S_z n_e n(Li) + \alpha_z^{eff} n_e n(H) \qquad (1)$$

The line q is produced predominantly by the inner-shell excitation of Li-like ions (C_q) and the line k arises from the dielectronic recombination of He-like ions only (C_k), where C_q and C_k indicate the rate coefficients for q line and k line through the inner-shell excitation and dielectronic recombination, respectively. Solid lines in Fig.2 are rate coefficients used in our clculations. Rate coefficients C_z by [7] and S_z from [1] are shown by dashed lines for comparison. Dot-dashed line indicate $\sigma_w^{rel} v$ for the resonance line by high energy electrons including relativistic effect[8],[9], where σ is the cross section and v velocity of electrons. For iron ions, data produced by [10] and [11] are used and they are compared with recent results by [16].

3 Spectra from TFTR tokamak

The spectra observed in the initial phase of ohmic heating show that the intensity of w is smaller than those of x, y and z[1] as shown in Fig.3. This suggests the contribution of the recombining plasma, where the effective recombination rate for w is smaller than those of x, y and z at $T_e < 1keV$. Hence, in order to get a better spectral fit, we introduce some amount of H-like ions. In the early phase of discharge, z and

q are remarkably strong. Both z and q are produced by the inner-shell ionization and the inner-shell excitation in Li-like ions which are sensitive to the amount of the high energy electrons as shown in Fig.2 by S_z and C_q. These phenomena imply the contribution of high energy electrons in order to produce H-like ions and z and q lines. We consider a time - dependent plasma model assuming that a small fraction of a hot component is produced in a bulk plasma at the beginning of the discharge. Then, the ionization process advances very rapidly by hot electrons, and H-like and He-like ions can be produced in an early phase. Since H-like ions produced in a hot component interact with a low temperature bulk plasma, the lines x, y and z are produced through recombination of H-like ions effectively.

We tried to fit the observed spectra with the model mentioned above. The parameters for spectral fits are the electron temperatures T_h and T_b, the ion density ratios n(Li)/n(He) and n(H)/n(He), and the fraction η of a hot component which interact with a bulk plasma. The derived temperatures of a hot component from the spectra and ion abundances are 7, 8 and 30 keV for the periods of 180 - 300, 300 - 420 and 420 -540 ms, respectively. The fractions of the suprathermal electron component are 0.03 % and 0.1 % for 180 - 420 ms and 420 -540 ms, respectively. The spectra predicted from the intermixing plasma are compared with the observed spectra in Fig.3. The contribution of a hot component is shown by hatched regions. This model can explain the observed spectra as well as the ion abundances derived from the spectra.

The ion density ratios n(H)/n(He) and n(Li)/n(He) derived from the spectral fits are plotted as a function of electron temperature of the bulk plasma in Fig.4. The values in the ionization equilibrium are plotted by dashed curves. As the electron temperature of the bulk plasma rises with time from 0.45 to 1.0 keV, the derived ion density ratio n(Li)/n(He) decreases and n(H)/n(He) increases. The value of n(Li)/n(He) is always larger than that in the ionization equilibrium. This indicates that the plasma is in an ionizing phase. On the other hand, the derived value of n(H)/n(He) is much higher than that in the ionization equilibrium and increases as the temperature rises, as seen in Fig.4. This implies that the plasma is over-ionized and the ionization process still dominates H-like ions. The calculated ion ratios assuming the temperature variation of the bulk plasma are shown by dott-dashed lines, and those including suprathermal electrons are plotted by solid lines.

Although a hot component can account for the enhancements of the ion abundances and the spectra, it does not work on the intensities of x and y. The intensity of z must be always larger than x and y with any mixture of n(H), n(He) and n(Li) at any plasma conditions. But the measurements show the spectra that x and y are stronger than z in the period after 420 ms. In order to solve these problems, we consider other processes in the followings.

1. ion - ion charge exchange

We explained a large excess of x and y in the later phase in JIPPT-IIU tokamak plasma with neon puffing[12] by charge exchange between H-like titanium ions and neon ions. We consider the charge transfer between H-like Ti ions and O ions. Assuming that the effective charge transfer recombination is $10^{-11}cm^3s^{-1}$ at low temperatures ($< 1keV$)[13], [14], oxygen contamination is required to be more than 5 % in order that the charge transfer recombination is comparable to the electron recombination at low temperature. At high temperatre ($\sim$ 1.5 keV) when the excitation process is effective, the charge exchange recombination rate is comparable to the excitation rate for $n(H)/n(He) = 0.07$ and 10% of oxygen comtamination.

2. two electron excitation

   In order to produce the intercombination lines x and y, two electron excitation-following the autoionization can be considered,

$$1s^2 2s + e \rightarrow 1s3d n\ell \rightarrow 1s2p + e. \quad (2)$$

   If the effective rate coefficient for this process is greater than 3 x $10^{-13}cm^3s^{-1}$ at 7 keV and 8 x $10^{-14}cm^3s^{-1}$ at 1.5 keV, the discrepancies for the lines x and y would be explained.

3. others

   Polarization by the suprathermal electrons might affect the intensities x, y, z and w[15]

Another problem for x and y are the intensity ratio of two lines. The observed spectra show always larger intensity for y than for x. The theoretical intensity of y is larger than that of x by excitation process and contrary by recombination process. But the differences of two lines is within 20%.

4 Spectra from solar flares

The high resolution X-ray spectra of highly ionized H-like and He-like iron ions from solar flares were observed by the Hinotori satellite[2]. From the spectral analysis they found that the ion ratios n(H)/n(He) of iron ions are always higher than those in the ionization equilibrium, although He-like spectra show the normal thermal spectra. The time dependent electron temperatures were derived from the intensity ratios of the satellite lines to the resonance line for both the H-like and He-like spectra. The derived electron temperature from H-like ions $T_e(H)$ is often higher than those derived

from He -like spectra $T_e(He)$ near the peak temperature.
In Fig.5, the ion ratios are plotted as a function of temperature following the time sequence for the large flare on 7 October 1981. The electron temperatures are those derived from He-like spectra I_j/I_w every 70 second intervals. Attached number indicates the order of the time evolution. The ionization equilibrium values are shown by dotted lines. Two dotted lines are the values by two different atomic data. The derived ion ratios n(H)/n(He) show the different trajectries between rising phase and decay phase of the electron temperature, which means that the plasma is not in the ionization equilibrium. The ion ratios n(H)/n(He) increase in the rising phase and decrease in the decay phase; the plasma is ionizing in the rising phase and recombining in the decay phase, although the values are always higher than the equilibrium values. The ion ratios n(Li)/n(He) also show the different tragectries for the rising phase and the decay phase.
We consider a hot spot model for solar flares similar to the previous section. Time resolved calculated ion abundances taking into account the time variation of the temperature are plotted as a function of T_e in Fig.6 for the two cases; (a) without high energy electrons and (b) with 5% of 8 keV high energy electrons. As shown in Fig.6(a), the ion ratios increase towards the ionization equilibrium as the electron temperature increases. That indicates the plasma is in the ionizing phase. In the ionizing phase the ion ratios are always smaller than the equilibrium values. On the other hand, the ion ratios decrease after the maximum temperature which indicates the recombining plasma. Including the 5% of 8 keV suprathermal electrons, the ion ratios become larger than those in the ionization equilibrium as in Fig.6(b). This result imply the possibility to explain the behaviour of the ion ratios by suprathermal electrons. It is estimated that at least 3% of suprathermal electrons of $\sim$10 keV is necessary to explain the ion abundances. In order to be consistent with the observed spectra which can be fitted well by thermal electrons, the effect of the high energy electrons for the spectra should be examined.
We have compared the calculated spectra using the data by [11], [12] with those by recent data in [13]. For He-like spectra, we found the differences for n=3 satellite line intenisties about 40%. This difference is not effective for the present analysis since the electron temperature is derived from I_j/I_w, but is important for the temperautre diagnostics using the intensity ratios of the n=3 satellite lines to the resonance line. The satellite intensities by [13] are always larger than those by [11]. The derived temperature by [13] is higher than that by [11] by 0.1 keV at 1.5 keV.
For H-like ions, the values in [13] are also larger than those in [12] by 40% for n=3 and 4 satellite lines. Since wavelengths of these satellite lines are included in the region of the Lyman α1 line, the intensity at Lyman α1 line differes 17% at 1.5 keV. This difference makes the temperature about 0.1 keV higher for the data by [12] than that by [13]. At the temperature higher than 2.5 keV, the difference is negligibly small. For the inten-

sities of the satellite lines at 1.787 - 1.789 A ($1s2s\ ^1S - 2s2p\ ^1P_1, 1s2p\ ^3P - 2p^2\ ^1D, ^3P$), 25% of difference is found. The intesities of the strongest satellite lines near 1.792 A ($1s2p\ ^1P_1 - 2p^2\ ^1D_2, 1s2p\ ^3P_2 - 2p^2\ ^3P_2$) agree within 6%.

Figure Captions

Fig.1 The energy level diagram of the prominent lines for He-like ions.

Fig.2 Excitation, ionization and recombination rate coefficients for lines w, z, q and k of Ti ions. Solid lines are those used in our calculations. Dashed line for C_z is from [8] and for S_z is from [1].

Fig.3 Observed (dots) and calculated (solid lines) spectra of He-like Ti ions in 60 ms intervals from an ohmically heated plasma of TFTR discharge. Hatched regions represent the contribution of a hot component.

Fig.4 Ion density ratios of n(Li)/n(He) and n(H)/n(He) for Ti ions against the electron temperatures. Dashed lines are the calculated values in the ionization equilibrium. Dott-dashed lines indicate the ratios assuming the temperature variation of a bulk plasma. Solid lines are those including a hot component. The ratios derived from the spectral fits are plotted by circles for n(Li)/n(He) and triangles for n(H)/n(He), respectively.

Fig.5 Derived ion density ratios n(H)/n(He), n(Li)/n(He) and n(Be)/n(He) for Fe ions from the solar flare spectra on 7 October 1981 against the electron temperatures. Dashed lines are the values in the ionization equilibrium.

Fig.6(a) Calculated ion abundances for Fe ions taking into account the temperature variation of the solar flare at 1981 October 7. The arrows indicate the direction of the time.
(b) Calculated ion abundances including 5% of 8 keV suprathermal electons.

References

[1] M. Bitter et al. *Phys. Rev. A 32 (1985) 3011*

[2] K. Tanaka, *Publ. Astron. Soc. Japan 38 (1986) 225*

[3] F. Bely-Dubau, P. Faucher, L. Steenman-Clark, M. Bitter, S. von Goeler, K.W. Hill, C. Camhy-Val and j. Dubau, *Phys. Rev. A 26 (1982) 3459*

[4] W. Lotz, *IPP 1/62 (1967)*

[5] T. Fujimoto and T. Kato, *Phys. Rev. A 30 (1984) 379*

[6] T. Kato, S. Morita K. Masai and S. Hayakawa, *Phys. Rev. A 36 (1987) 795*

[7] T. Kato, K. Masai, *Journal de Physique C1, Suppl. no.3 49 (1988) C-349*

[8] A.K. Pradhan, *Ap. J. Suppl. 59 (1985) 183*

[9] M. Inokuti, *Rev. Mod. Phys. 43 (1975) 297*

[10] P. Lee, A.J. Lieber A.K. Pradhan and Yueming, Xu, *Phys. Rev. A 34 (1986) 3210*

[11] F. Bely-Dubau, J. Dubau, P. Faucher and A.H. Gabriel, *Mon. Not. roy. Astron. Soc.,198 (1982) 239*

[12] J. Dubau, A. H. Gabriel, M. Loulerque, L.Steenman-Clark and S. Volonte, *Mon. Not. roy. Astron. Soc.,195 (1981) 705*

[13] U. Safronova, *To be published in NIFS report (1990)*

[14] F. Koike, K. Fujima and T. Kato *Annal Review, IPP, Nagoya 1988*

[15] V.A. Bazylev and M.I. Chibisov, *Sov. J. Plasma Phys. 5 (1979) 327*

[16] M. K. Inal *ORSAY No 3656, Doctor theses, Universite de Paris-Sud*

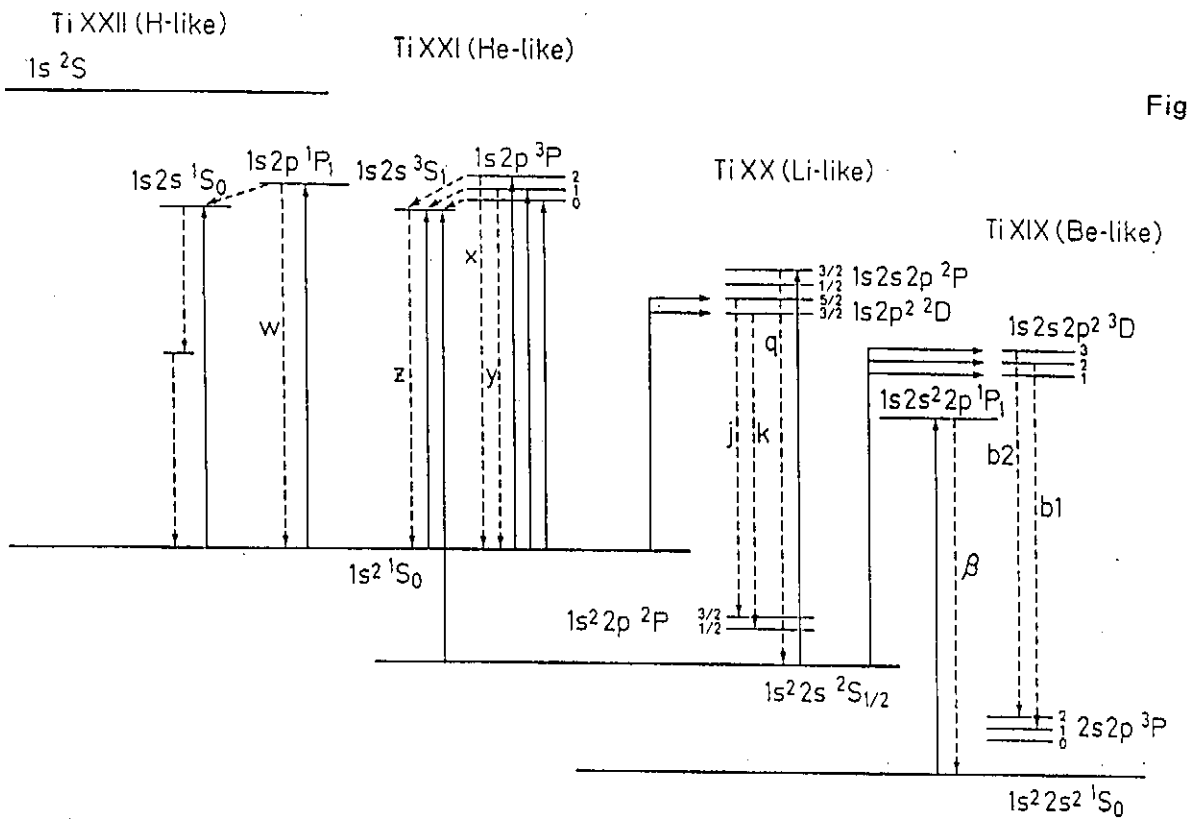
Ti XXII (H-like)
1s 2S
Ti XXI (He-like)
1s2s 1S0
1s2p 1P1
1s2s 3S1
1s2p 3P
Ti XX (Li-like)
Ti XIX (Be-like)
1s2s2p 3P
1s2p2 2D
1s2s2p2 3D
1s2s2p 1P1
1s2 1S0
1s2 2p 2P
1s2 2s 2S1/2
1s2 2s2p 3P
1s2 2s2 1S0
w
x
y
z
q
j
k
b2
b1
β

Fig.1

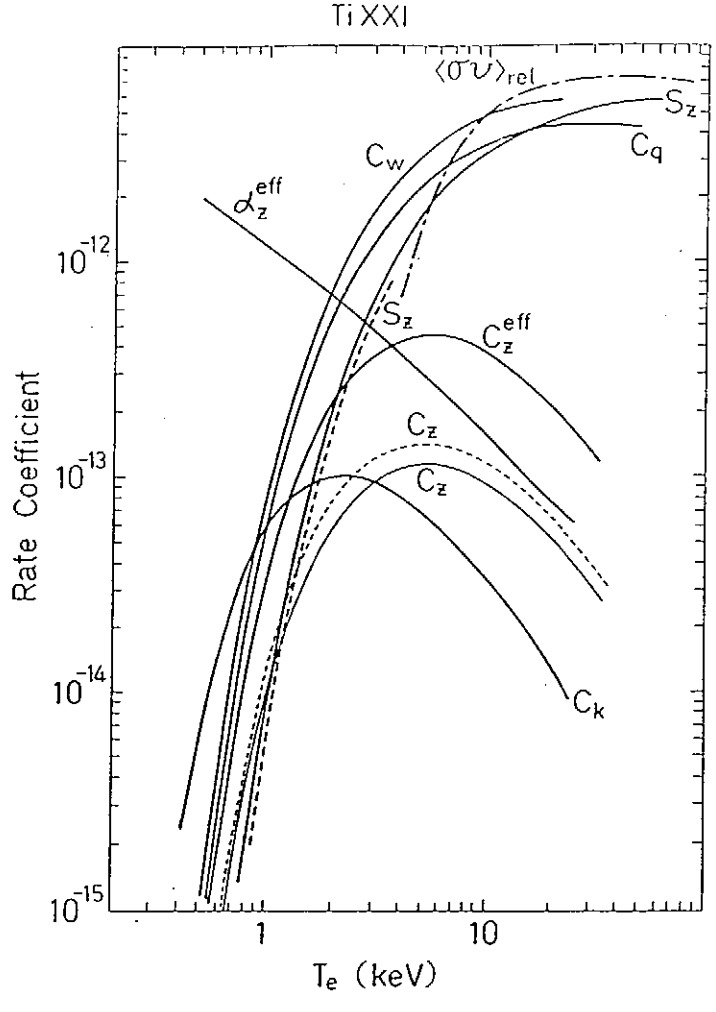
Ti XXI
⟨σv⟩rel
Sz
Cq
Cw
α_z^eff
C_z^eff
Cz
Ck
10^-12
10^-13
10^-14
10^-15
Rate Coefficient
1
10
Te (keV)

Fig.2

Fig.3

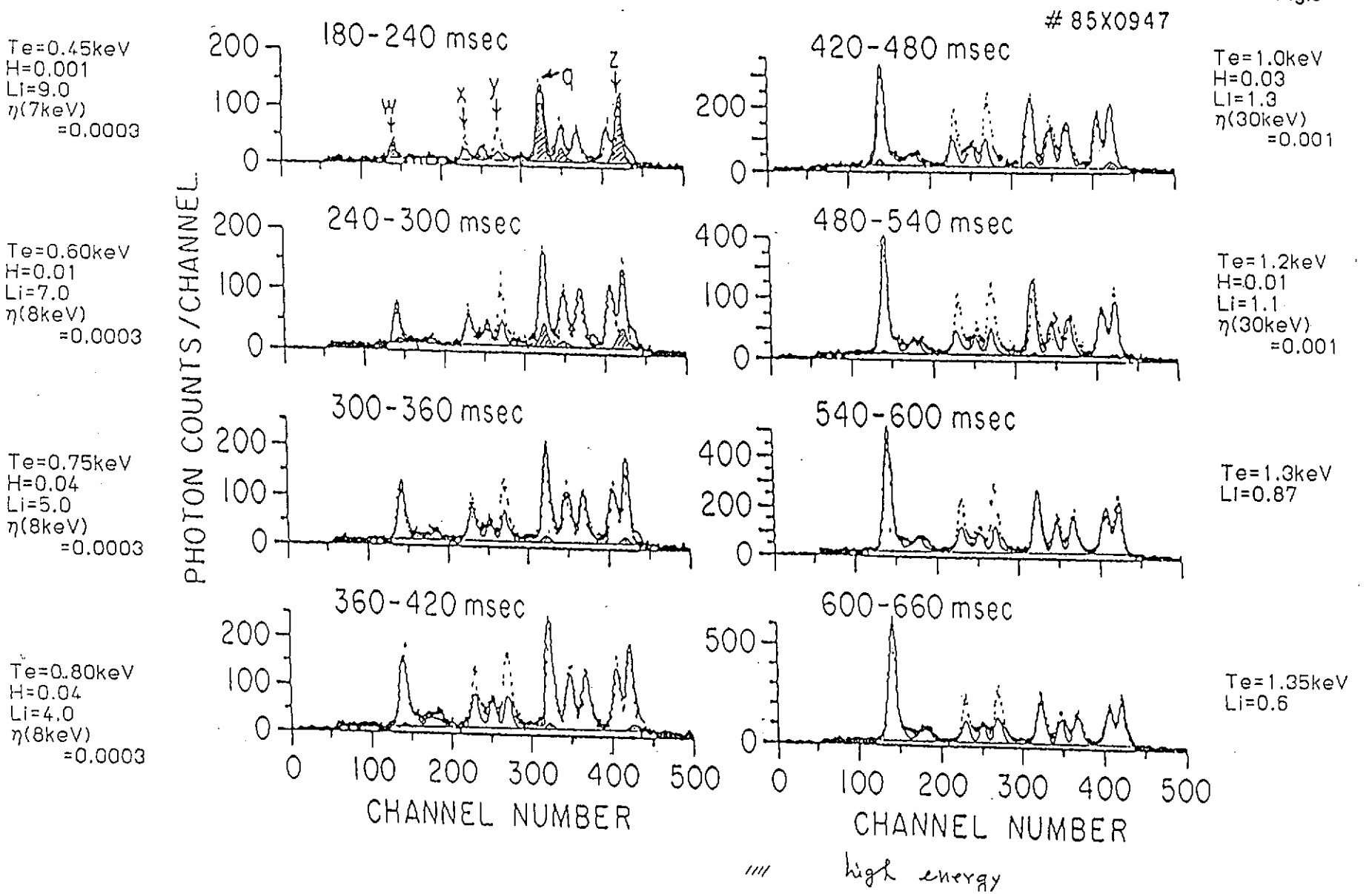
#85X0947
180-240 msec
240-300 msec
300-360 msec
360-420 msec
420-480 msec
480-540 msec
540-600 msec
600-660 msec
W
X
Y
q
Z
PHOTON COUNTS/CHANNEL
CHANNEL NUMBER
CHANNEL NUMBER
Te=0.45keV
H=0.001
Li=9.0
η(7keV)
=0.0003
Te=0.60keV
H=0.01
Li=7.0
η(8keV)
=0.0003
Te=0.75keV
H=0.04
Li=5.0
η(8keV)
=0.0003
Te=0.80keV
H=0.04
Li=4.0
η(8keV)
=0.0003
Te=1.0keV
H=0.03
LI=1.3
η(30keV)
=0.001
Te=1.2keV
H=0.01
Li=1.1
η(30keV)
=0.001
Te=1.3keV
LI=0.87
Te=1.35keV
Li=0.6
//// high energy

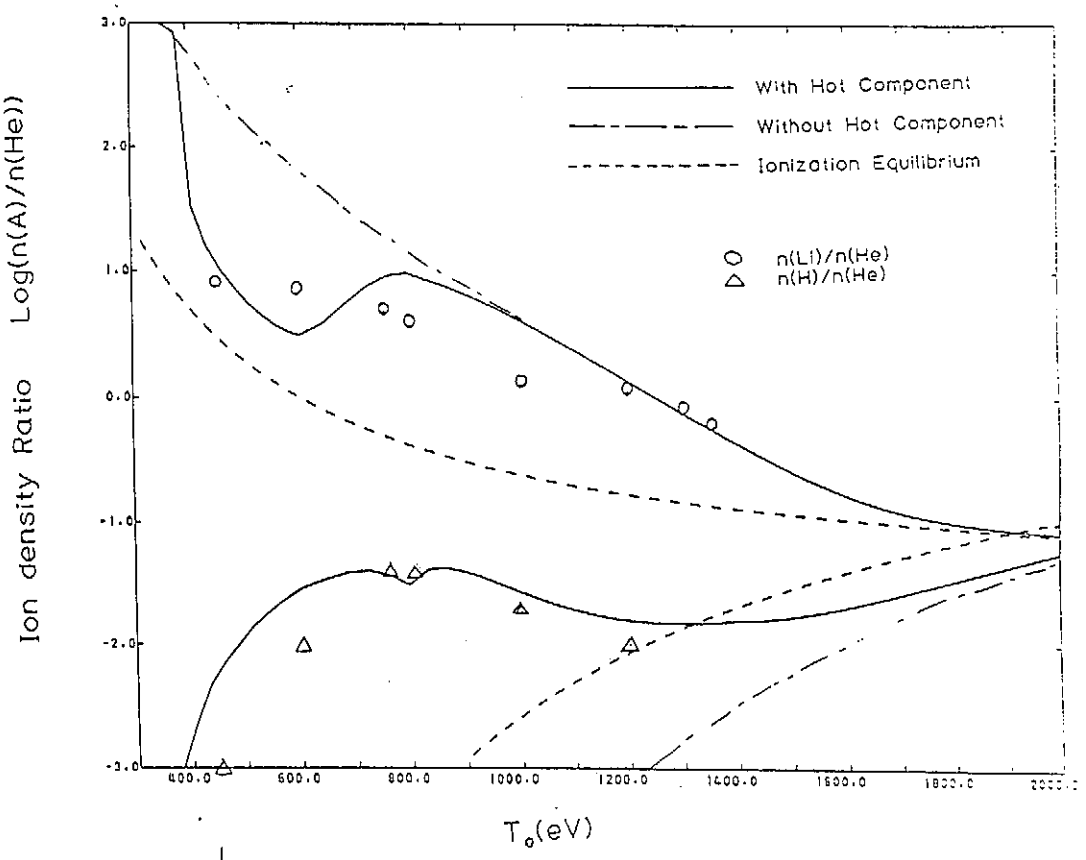
Ion density Ratio Log(n(A)/n(He))
With Hot Component
Without Hot Component
Ionization Equilibrium
n(Li)/n(He)
n(H)/n(He)
3.0
2.0
1.0
0.0
-1.0
-2.0
-3.0
400.0
600.0
800.0
1000.0
1200.0
1400.0
1600.0
1800.0
T_e(eV)

Fig.4

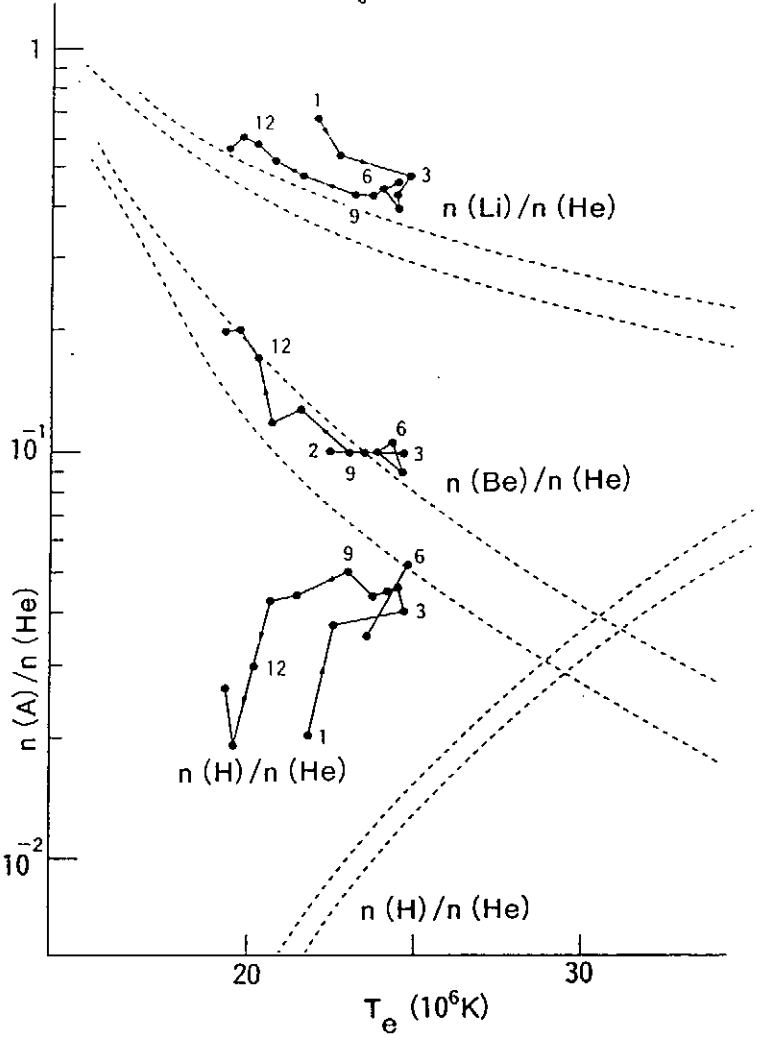
1
10^{-1}
10^{-2}
n (A)/n (He)
n (Li)/n (He)
n (Be)/n (He)
n (H)/n (He)
n (H)/n (He)
1
2
3
6
9
12
20
30
T_e (10^6K)

Fig.5

Fig.6(a)

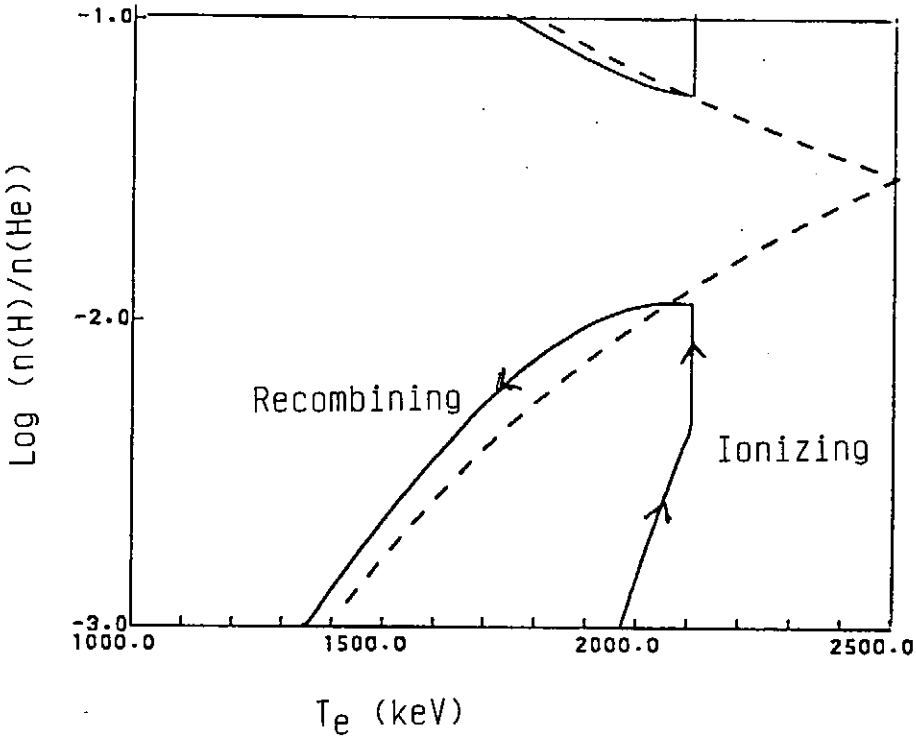
-1.0
-2.0
-3.0
1000.0
1500.0
2000.0
2500.0
Log (n(H)/n(He))
Recombining
Ionizing
Te (keV)

Fig.6(b)

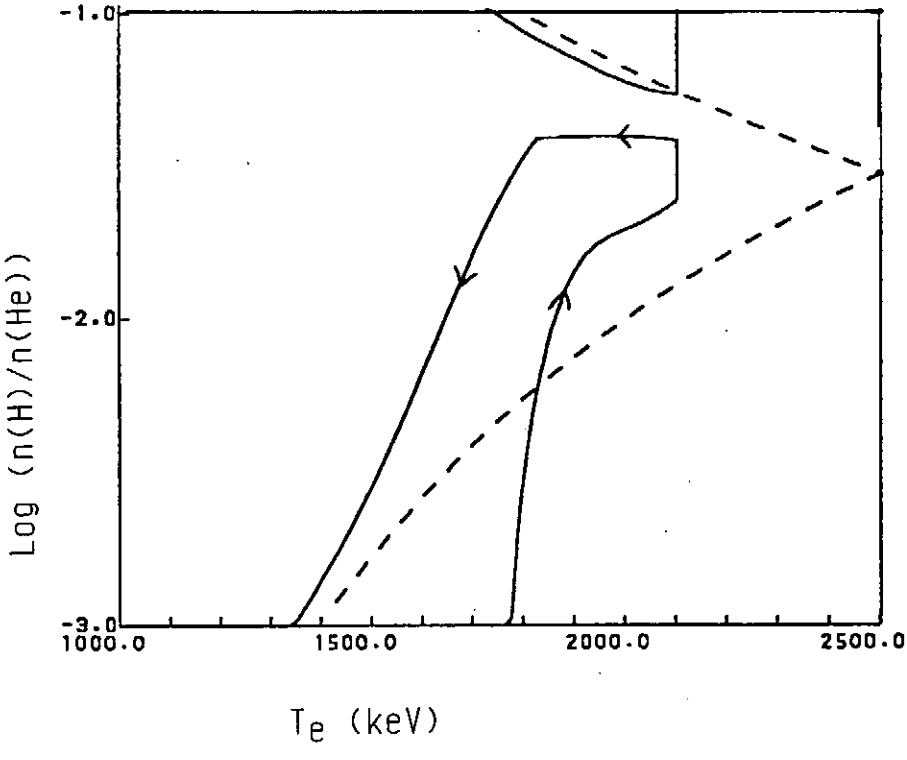
-1.0
-2.0
-3.0
1000.0
1500.0
2000.0
2500.0
Log (n(H)/n(He))
Te (keV)